CORA Cork Open Research Archive
Cartlann Taighde Oscailte Chorcaí

Title	Synthesis, functionalisation and characterisation of germanium nanocrystals & their applications
Authors	Carolan, Darragh
Publication date	2015
Original Citation	Carolan, D. 2015. Synthesis, functionalisation and characterisation of germanium nanocrystals & their applications. PhD Thesis, University College Cork.
Type of publication	Doctoral thesis
Rights	© 2015, Darragh Carolan. - http://creativecommons.org/licenses/by-nc-nd/3.0/
Download date	2026-11-04 17:42:22
Item downloaded from	https://hdl.handle.net/10468/2070



UCC
University College Cork, Ireland
Coláiste na hOllscoile Corcaigh

Ollscoil na hÉireann

NATIONAL UNIVERSITY OF IRELAND



Synthesis, Functionalisation and Characterisation of Germanium Nanocrystals & their Applications

A Thesis Presented to

The National University of Ireland, Cork

for the degree of

Doctor of Philosophy

by

Darragh Carolan

Supervised by Dr. Hugh Doyle



Tyndall National Institute

University College Cork

January 2015

Table of Contents

Table of Contents ..... **ii**

Declaration ..... **v**

Acknowledgements ..... **vi**

Abstract ..... **viii**

Glossary of Acronyms ..... **xi**

List of Figures, Schemes and Tables ..... **xv**

Chapter 1: Introduction **1**

1.1 Introduction **1**

1.1.1 Semiconductor Nanocrystals 1

1.1.2 Germanium Nanocrystals 8

Physical Methods 8

Chemical Methods 9

1.2 Metal Ion Sensing **24**

1.2.1 Introduction 24

1.2.2 Review on Metal Ion Sensing 29

1.3 Scope of the rest of this Thesis **36**

1.4 References **38**

Chapter 2: Synthesis & Characterisation of Germanium Nanocrystals **48**

2.1 Introduction **49**

2.2 Experimental Section **49**

2.2.1 Synthesis and Purification of Amine Terminated Ge NCs 49

Chemicals. 50

Synthesis and Purification. 51

2.2.2 Characterisation 52

Structural Characterisation 52

Optical Characterisation 52

Lifetimes 52

Determination of the Quantum Yield 53

2.3 Results and Discussion 56

2.3.1 Amine Terminated Ge NCs 56

2.3.2 Evidence for a Size Threshold Between Blue and Green Emission 66

2.4 Conclusion 71

2.5 References 72

Chapter 3: Synthesis & Characterisation of Surface Modified Germanium Nanocrystals 75

3.1 Introduction 76

3.2 Experimental Section 77

3.2.1 Synthesis and Purification of Alkyl Terminated Ge NCs 77

Chemicals. 77

Synthesis and Purification. 77

3.2.2 Synthesis and Purification of Functionalised Ge NCs 78

Chemicals. 78

Synthesis and Purification. 78

3.2.3 Characterisation 79

X-Ray Photoelectron Spectroscopy 79

3.3 Results and Discussion 81

3.3.1 Alkyl Terminated Ge NCs 81

3.3.2 Surface Modified Ge NCs 88

3.4 Conclusion 92

3.5 References 94

Chapter 4: Applications of Germanium Nanocrystals in Metal Ion Sensing 96

4.1 Introduction 97

4.2 Experimental Section 98

4.2.1 Chemicals and Procedures 98

Chemicals. 98

pH Measurements. 98

Metal Ion Sensing. 98

PL “Turn-On” Experiment. 99
4.2.2 Characterisation 99
Optical Characterisation 99
4.3 Results and Discussion 99
4.3.1 Selection of Ge NCs for Metal Ion Sensing 99
4.3.2 Metal Ion Sensing 101
4.4 Conclusion 110
4.5 References 112
Chapter 5: Summary & Conclusions 115
5.1 Summary 116
5.2 Conclusion 118
Appendix 123
6.1 Appendix 124
6.1.1 Peer Reviewed Publications 124
6.1.2 Targeted Publications 124
6.1.3 Outputs 125
6.1.4 Modules 125

Declaration

This thesis is my own work and has not been submitted for another degree, either at The National University of Ireland, Cork or elsewhere.

Darragh Carolan

_____

Acknowledgements

Firstly, I would like to sincerely thank my supervisor, Dr. Hugh Doyle for giving me this opportunity to do a doctorate in Chemistry. He put up with me throughout the PhD and gave me huge help when preparing reports, presentations and publications. His helpful guidance, useful input and insightful comments were a source of inspiration and motivation throughout this project. He is without doubt, one of the smartest people I have met so far! He was also great for just a normal chat about rugby and everyday life.

I would like to acknowledge my thesis committee, Prof. Martin Pemble, Dr. James Rohan and Carmel Kelleher for their support, advice and suggestions at the progress review meetings.

I would like to thank all the supervisors in the NTG group, namely Daniela Iacopino, Alan O'Riordan and head of the group Aidan Quinn who all gave me very useful advice and tips at various meetings and discussions. Many thanks to the post-docs/staff in the group; Pierre Lovera (Dr. Love), Micheal Burke ((Super)Mimi), Armelle Montrose, Mary Manning, Brendan Kennedy, Karen Dawson, Paul McElhone, you were all very encouraging. To all past and present students in the group, especially Amelie Wahl (Amelie-lee-poodle), John McHale, Andrea Pescaglini (The Rock – but not so hard), Ethel Noonan, Micki Mitchell (Brown-Star), Roxane Puicervert and Daniel Lordan (Lordy/Lord-Dan) who were all my office "buddys" at one stage or another. Thank you to all the other students; Alfonso, Carola, Colm (Ginger Puffo), Daniel J (Jonesy Doodle), Fabrizio (Momo, always up for a night out!), Niamh, Sean (Seanie Doodle/Babes), Marcus, Luis and Rob. I'll never forget some of the *epic* craic/nights out/trips away we had!

A special thanks to Keith Linehan (The Sausagemeister) who worked on closely related projects to me. Thank you for training me on the synthesis and purification and on certain instruments at the beginning. Your "straight to the point" attitude and insightful comments along the way were a great help.

Huge thanks to other various people outside the NTG group as well; Dave Pierce was a great friend throughout, always good for a chat and a great cup of tea! Cormac, Harry, Jan, Niall, Patricia, Conor, Brian, Donal (D-bag), Rose and some of the other Italians; Marcox2 and Francesco.

I have to say thank you to all past and present members of the Tyndall Taggers tag rugby team. At times, playing tag was the only thing keeping me sane, while we actually became a respectable enough team in the last 3 years or so!

Last but certainly not least, I would like to thank my family. Thanks to my brother Ultan (Ultie baby), whenever I went back home, has was always there for a bit of banter and some *great* nights out. Thanks also to my sister Natasha (Natie-boom-boom) for watching the late night movies together and letting me see her horse riding sessions.

But I think the biggest thanks I have to give is to my parents, Philip and Bernadette. They always said that getting an education was one of the most important things in life and I thank them for that attitude they had. They never hesitated to help me out financially and I am forever grateful for that. They kept me on the straight track when things went badly (They know what I mean!) and they had faith in me when I came down to Cork. So Mammy and Daddy, I love you guys and thank you, without your support this would have been impossible.

And finally, thank you for reading this thesis.

Abstract

In the last two decades, semiconductor nanocrystals have been the focus of intense research due to their size dependant optical and electrical properties. Much is now known about how to control their size, shape, composition and surface chemistry, allowing fine control of their photophysical and electronic properties, leading to utilisation in a range of applications from biological imaging to optoelectronic devices. However, genuine concerns have been raised regarding the heavy metal content of these materials, which is toxic even at relatively low concentrations and may limit their wide scale use, particularly in clinical applications where the high disposal costs for heavy metal containing waste must be considered. These toxicological concerns have driven the development of heavy metal free alternatives. In recent years, germanium nanocrystals (Ge NCs) have emerged as environmentally friendlier alternatives to II-VI and IV-VI semiconductor materials as they are nontoxic, biocompatible and electrochemically stable.

This thesis reports the synthesis and characterisation of Ge NCs and their application as fluorescence probes for the detection of metal ions. A room-temperature method for the synthesis of size monodisperse Ge NCs within inverse micelles is reported, with well-defined core diameters that may be tuned from 3.5 to 4.5 nm. The Ge NCs are chemically passivated with amine ligands using a Pt-catalysed hydrogermylation reaction, minimising surface oxidation while rendering the NCs dispersible in a range of polar solvents, making them amenable to low cost, solution based device processing. Regulation of the Ge NCs size is achieved by variation of the cationic quaternary ammonium salts used to form the inverse micelles. UV-Visible absorbance and photoluminescence spectroscopy show significant quantum confinement effects, with moderate absorption in the UV spectral range, and a strong, narrow luminescence in the visible with a marked dependency on excitation wavelength. A maximum quantum yield of 20% is shown for the nanocrystals, and a transition from primarily blue to green emission is observed as the NC diameter increases from 3.5 to 4.5 nm. To determine whether the observed size threshold was due to quantum confinement effects or differing surface chemistry/oxidation, a polydisperse sample with a mixed blue/green

emission profile is prepared and separated by centrifugation into individual sized NCs which each showed blue and green emission only, with total suppression of other emission colours.

A new, efficient one step synthesis of Ge NCs with *in situ* passivation and straightforward purification steps is also reported. Ge NCs are formed by co-reduction of a mixture of $GeCl_4$ and *n*-butyltrichlorogermane; the latter is used both as a capping ligand and a germanium source. When the reducing agent is added, while the Ge-Cl bonds in both precursors are readily reduced, the Ge-C bond in *n*-butyltrichlorogermane is more stable, capping the surface and ultimately limiting the growth of the NCs. This surface-bound layer of butyl chains both chemically passivates and stabilises the Ge NCs to facilitate dispersal in a range of non-polar solvents. Optical spectroscopy confirmed that these NCs are in the strong quantum confinement regime, with significant involvement of surface species in exciton recombination processes. The PL QY is determined to be 37 %, one of the highest values reported for organically terminated Ge NCs.

A synthetic method is developed to produce size monodisperse Ge NCs with modified surface chemistries bearing carboxylic acid, acetate, amine and epoxy functional groups. The effect of these different surface terminations on the optical properties of the NCs is also studied. Comparison of the emission properties of these Ge NCs showed that the wavelength position of the PL maxima could be moved from the UV to the blue/green by choice of the appropriate surface group.

We also report the application of water-soluble Ge NCs as a fluorescent sensing platform for the fast, highly selective and sensitive detection of Fe^{3+} ions *via* quenching of their strong blue luminescence without the need for specific labelling groups. The Ge NCs show excellent selectivity toward Fe^{3+}, with no quenching of the fluorescence signal induced by the presence of Fe^{2+} ions, allowing for solution phase discrimination between ions of the same element with different formal charges. The luminescence quenching mechanism is confirmed by lifetime and absorbance spectroscopies, while the applicability of this assay for detection of Fe^{3+} in real water samples is investigated and found to satisfy the US Environmental

Protection Agency requirements for Fe^{3+} levels in drinkable water supplies. To the best of our knowledge, this is the first report of the use of luminescent NCs for label-free detection of a specific heavy metal ion in a specific formal charge state.

Glossary of Acronyms

(In order of appearance in the text)

SC	Semiconductor
E_g	Band gap
HOMO	Highest occupied molecular orbital
LUMO	Lowest unoccupied molecular orbital
NC	Nanocrystal
QD	Quantum dot
QY	Quantum yield
UV	Ultraviolet
PL	Photoluminescence
HRTEM	High resolution transmission electron microscopy
IR	Infrared
NIR	Near-infrared
$GeCl_4$	Germanium tetrachloride
NaGe/KGe	Zintl salt
NH_4Br	Ammonium bromide
PLE	Photoluminescence excitation
XAS	X-Ray absorption spectroscopy
EXAFS	Extended X-Ray absorption fine structure
Mg_2Ge	Magnesium germanide
GeO_2	Germanium oxide
UV-Vis	Ultraviolet/visible absorbance spectroscopy
IPA	Isopropylalcohol
GRO	Germanium rich oxide
XRD	X-Ray diffraction
FTIR	Fourier transform infrared spectroscopy
XPS	X-Ray photoelectron spectroscopy
SAED	Selected area electron diffraction
NEXAFS	Near-edge X-Ray absorption fine structure
SiO_2	Silicon dioxide
TEOG	Tetraethoxyorthogermanate
TEOS	Tetraethoxyorthosilicate

H_2O_2	Hydrogen peroxide
HF	Hydrofluoric acid
TEG	Tetraethylgermane
DPG	Diphenylgermane
CO_2	Carbon dioxide
TCG	Tetrachlorogermane
TOP	Tri-*n*-octylphosphine
TOPO	Tri-*n*-octylphosphine oxide
TOA	Tri-*n*-octylamine
NW	Nanowire
TBP	Tri-*n*-butylphosphine
ODE	Octadecene
HDA	Hexadecylamine
ODT	Octadecanethiol
TGA	Thermogravimetric analysis
DTA	Differential thermal analysis
$LiAlH_4$	Lithium aluminium hydride
HPLC	High pressure liquid chromatography
$NaBH_4$	Sodium borohydride
$N_2H_4xH_2O$	Hydrazine hydrate
GeI_4	Germanium tetraiodide
CTAB	Hexadecyltrimethylammonium bromide
TOAB	Tetraoctylammonium bromide
H_2PtCl_6	Chloroplatinic acid
FWHM	Full width at half maximum
$C_{12}E_5$	Pentaethylene glycol monododecyl ether
$Li(C_2H_5)_3BH$	Super-hydride/Lithium triethylborohydride
$LiBH_4$	Lithium borohydride
PVP	Polyvinylpyrrolidone
BuLi	*n*-Butyllithium
NMR	Nuclear magnetic resonance
GeI_2	Germanium diiodide
HDMS	Hexamethyldisilazane
DRIFT	Diffuse reflectance infrared fourier transform

AAS	Atomic absorption spectrometry
ICP-MS	Inductively coupled plasma mass spectrometry
K_{SP}	Solubility product constant
K_{SV}	Stern-volmer constant
HBT	2-(2-hydroxyphenyl)benzothiazole
LOD	Limit of detection
CQD	Carbon quantum dots
IL	Ionic liquid
LR	Linear range
RS	Real sample
US EPA	Unites states environmental protection agency
TBAB	Tetrabutylammonium bromide
THAB	Tetrahexylammonium bromide
TKAB	Tetrakis(decyl)ammonium bromide
THDAB	Tetrahexadecylammonium bromide
NaOH	Sodium hydroxide
DI	Deionised
PTFE	Polytetrafluoroethylene
CCD	Charge-coupled device
EDX	Energy dispersive X-Ray spectroscopy
TCSPC	Time correlated single photon counting
APD	Avalanche photodiode
PVDF	Polyvinylidene fluoride
DTAB	Dodecyltrimethylammonium bromide
n-BTCG	*N*-butyltrichlorogermane
FFT	Fast fourier transform
PBS	Phosphate buffered saline
HCl	Hydrochloric acid
$AlCl_3 \bullet 6H_2O$	Aluminum chloride hexahydrate
$Cd(ClO_4)_2 \bullet xH_2O$	Cadmium perchlorate hydrate
$CoCl_2$	Cobalt chloride
$CuCl_2$	Copper chloride
$CrK(SO_4)_2 \bullet 12H_2O$	Chromium potassium sulfate dodecahydrate
$FeCl_2$	Iron chloride

$Fe(NO_3)_3 \bullet 9H_2O$	Iron nitrate nonahydrate
$HgCl_2$	Mercury chloride
$MnCl_2$	Manganese chloride
$NiCl_2$	Nickel chloride
$PbCl_2$	Lead chloride
$PdCl_2$	Palladium chloride
$Zn(CH_3COO)_2 \bullet 2H_2O$	Zinc acetate dihydrate
DA	Dopamine
Mel	Melamine
3,4 DHPA	3,4-dihydroxyphenylacetic acid
Phos	Sodium phosphate monobasic monohydrate
IUPAC	International union of pure and applied chemistry

List of Figures, Schemes and Tables

Figure 1-1: Simplified energy level diagram for metals, semiconductors and insulators. The red shaded boxes represent the filled valence bands and the white boxes represent the empty (at 0 K) conduction bands 1

Figure 1-2: Electronic band structures for direct (a) and indirect (b) semiconductors. The straight arrows show the lowest energy transition between the valence band (bottom) and conduction band (top). A change in *k* is necessary for indirect semiconductors.....2

Figure 1-3: The effect of quantum confinement on the energy levels in a SC material as it goes from bulk size to nanometre sized quantum dots. Right, the energy level structure of a molecule.....4

Figure 1-4: (a) Size- and material- dependent emission spectra of SC NCs. Blue curves represent different sizes of CdSe nanocrystals with diameters of 2.1, 2.4, 3.1, 3.6, and 4.6 nm (from right to left). The green series is InP NCs with diameters of 3.0, 3.5, and 4.6 nm. Red curves are InAs nanocrystals with diameters of 2.8, 3.6, 4.6, and 6.0 nm. (b) Image of solutions of colloidal QDs of various size and composition showing emission when excited with an Ultraviolet (UV) lamp. (c) Photoluminescence (PL) spectra of CdSe-ZnS and PbS-CdS core-shell QDs. The inset shows a schematic of a typical core-shell colloidal QD and a High Resolution Transmission Electron Microscopy (HRTEM) image of a CdSe NC (Part (a) adapted from ref 11 and parts (b) and (c) adapted from ref 13).....7

Figure 1-5: Scheme of work for the synthesis of Ge NCs *via* a metathesis reaction between Ge Zintl salts and $GeCl_4$, followed by surface modification to give different functional groups on the NC (top left). (a) HRTEM image of a 15 nm diameter Ge NC, (b) TEM image and size distribution histogram for Ge NCs synthesised by reacting NaGe and NH_4Br, and (c) photoluminescence (right) and photoluminescence excitation (PLE) (left) spectra for butyl-terminated Ge nanoparticles with an average diameter of 6.2 nm (adapted from ref 37).....10

Figure 1-6: Left, schematic highlighting the synthesis of Ge nanoparticles by thermally decomposing a sol-gel-derived polymer. Right, TEM images and SAED

pattern for Ge NCs liberated from a GeO_2 matrix upon dissolution in water at 60 ^{0}C for (a, b) 30 min and (c) 2.5 h. (adapted from ref 37) 12

Figure 1-7: Left: the synthesis of Ge NCs by decomposing $Ge[N(SiMe_3)_2]_2$ in oleylamine and octadecene at 300 ^{0}C. (a) TEM image, (b) SAED pattern, and (c) HRTEM image of the 7 ± 4 nm Ge NCs produced. (d) Optical characterisation of Ge NCs in toluene (adapted from ref 37)..... 15

Figure 1-8: Upper left: schematic depicting the formation of Ge NCs by reducing Ge (IV) halides with $LiAlH_4$. (a) TEM image, SAED pattern, and size histogram for Ge NCs synthesised by reducing $GeCl_4$ with $LiAlH_4$ in THF and in an ultrasonic bath for 30 min. (b) TEM image and SAED pattern for *n*-undecyl terminated Ge nanoparticles synthesised by reducing GeI_4 with $LiAlH_4$ at room temperature, followed by refluxing in *n*-undecene. (c) TEM image and size histogram for 4.0 ± 0.5 nm Ge particles synthesised by reducing a toluene solution of $GeCl_4$ with $LiAlH_4$/THF at room temperature in the presence of tetraoctylammonium bromide (adapted from ref 37)..... 17

Figure 1-9: Top: schematic for the synthesis of Ge NCs by reducing GeI_2 with *n*-butyllithium. (a) TEM image of 4.0 ± 1.7 nm Ge nanoparticle, and (b) normalised photoluminescence spectra for three different sizes of octadecene-capped Ge NCs, as well as TOP-capped Ge nanoparticles (green). The excitation wavelength used was 808 nm (adapted from ref 37)..... 20

Figure 1-10: (a-c) TEM images showing the Ge nanoparticles produced by a one-pot heat-up. Decreasing the concentration of GeI_4 produced NCs with decreasing average sizes from 22 nm (a) to 6 nm (c) (adapted from ref 37) 22

Figure 1-11: (a) Exciton recombination across the bandgap within the NC core, (b) emission resulting from transfer of excitons from the core to surface states, (c) emission resulting from the generation of excitons at the surface states of the NC 23

Figure 1-12: The various interaction pathways that can lead to fluorescence quenching in QDs..... 26

Figure 1-13: Top, visual detection of the quenching effect of Fe^{3+} on the fluorescence of the dansyl compound (a); blank, (b); 0.23 mM Fe^{3+}, (c); 0.46 mM Fe^{3+} and (d); 1 mM Fe^{3+}. Bottom, fluorescence response of the compound upon

addition of (a)-(k), 0-25 µM Fe^{3+}, inset: calibration curve response from the data (adapted from ref 89).....30
Figure 1-14: Left, Schematic illustration for the fluorescence quenching mechanism of CQDs in the presence of Fe^{3+}. The top equation shows the formation of a complex between Fe^{3+} and 6 phenolic hydroxyl groups. Right, PL spectra of the CQDs in the presence of increasing Fe^{3+} concentrations (adapted from ref 96).....32
Figure 1-15: (a) Representative PL spectra of CQDs in the presence of increasing Fe^{3+} concentrations (0-700 µM). (b) The relationship between $(I_0\text{-}I)/I_0$ and Fe^{3+} from 0 to 700 µM. Inset is a linear region. I and I_0 are the PL intensities of CQDs in the presence and absence of Fe^{3+}, respectively (adapted from ref 98) 32
Figure 1-16: (a) Photo of CQDs without and with 300 µM Fe^{3+}. (b) Comparison of PL intensity of the CQDs after the addition of various metal ions with a concentration of 100 µM. (c) PL spectra of CQDs with increasing Fe^{3+} concentration from 0-500 µM. (d) F_0/F *vs* Fe^{3+} concentration derived from the data in (c) (adapted from ref 101) 33
Table 1-1: Overview of the different types of probes used in the detection of Fe^{3+} ions 34
Scheme 2-1: Depiction of the different steps involved in the synthesis of Ge NCs ..50
Figure 2-1: (a) The fluorescence spectrum of 9,10 diphenylanthracene showing absorbance value, integration range and integrated intensity. (b) Plot of integrated intensity *vs* absorbance for various dilutions of the reference material with a linear fit to the data 54
Table 2-1: Synthetic conditions for the reactions carried out in this section 55
Figure 2-2: Chemical structures of the surfactants used in this study, (a) TBAB, (b) THAB, (c) TOAB, (d) TKAB 56
Figure 2-3: TEM images of Ge NCs synthesised using the surfactants (a) TBAB, (b) THAB, (c) TOAB and (d) TKAB. Inset: Size histograms of Ge NCs with Gaussian curves fitted to the data 57
Figure 2-4: (a) HR-TEM image of an individual Ge NC. (b) SAED pattern of as-synthesised Ge NCs, with the reflections characteristic of crystalline Ge indexed...58
Figure 2-5: FTIR spectrum of the amine-terminated Ge NCs 59

Figure 2-6: (a) UV-Vis absorption spectra for the different sized NCs. (b) Tauc plotting of the UV-Vis data shows a decrease in the bandgap with increasing size . 59
Figure 2-7: (a) PL spectra of aqueous dispersions of Ge NCs recorded using an excitation wavelength of 400 nm. (b) Wavelength position of the luminescence maximum as a function of excitation wavelength. (c) Representative red shift of the maximum emission wavelength with increasing excitation wavelength 60
Figure 2-8: Normalised PL spectra of aqueous dispersions of Ge NCs recorded using different excitation wavelengths for (a) 3.5 nm, (b) 3.7nm, (c) 4.1 nm and (d) 4.5 nm nanocrystals 61
Figure 2-9: Normalised photoluminescence excitation (PLE) spectra of aqueous dispersions of Ge nanocrystals. The wavelength positions at which the spectra were recorded are indicated..... 63
Figure 2-10: TEM image of the NCs produced using TOAB as the surfactant template, re-dispersed in chloroform 63
Figure 2-11: Normalised PL spectra of Ge NCs dispersed in (a) water, (b) chloroform, (c) acetonitrile, (d) dichloromethane, (e) ethanol and (f) methanol recorded using different excitation wavelengths 64
Figure 2-12: Stability test for the Ge NCs 65
Figure 2-13: (a) Integrated PL intensity *vs*. absorbance for dilute dispersions of blue emitting Ge NCs and 9,10-diphenylanthracene. (b) Integrated PL intensity *vs*. absorbance for dilute dispersions of green emitting Ge NCs and fluorescein 66
Figure 2-14: Left, TEM images of the (a) parent solution, (b) supernatant and (c) pellet. Right, histograms of the NC size with curves fitted to the data using a lognormal model in the case of (a) and (c) and a Gaussian model in the case of (b) 67
Figure 2-15: (a) UV-Vis, PL and PLE (dashed lines) spectra of (a) 3.9 nm and (b) 6.8 nm Ge NCs. Excitation-emission scanning matrices for (c) 3.9 nm and (d) 6.8 nm Ge NCs 68
Figure 2-16: (a) Excitation-emission scanning matrix, (b) PL and PLE (black line) spectra of the parent solution 69
Figure 2-17: Integrated PL intensity *vs*. absorbance for dilute dispersions of (a) 3.9 nm Ge NCs and 9,10 diphenylanthracene, (b) 6.8 nm Ge NCs and fluorescein. (c) PL

decays of both NC samples and (d) long-term PL stability of both samples recorded over 6 hours 70
Scheme 3-1: Schematic of the one-pot method used to produce butyl terminated Ge NCs by co-reduction of $GeCl_4$ and *n*-butyltrichlorogermane with *n*-butyllithium77
Table 3-1: Synthetic conditions for the reactions carried out in this section 80
Figure 3-1: Left, TEM image of Ge NCs synthesised by the reduction of both *n*-butyltrichlorogermane and $GeCl_4$. Right, histogram of Ge NC diameters fitted using a Gaussian model 81
Figure 3-2: Left, TEM images and, right, size histograms and of Ge NCs produced by the reduction of a single precursor (a) *n*-butyltrichlorogermane and (b) $GeCl_4$ 82
Figure 3-3: (a) HR-TEM of an individual Ge NC, inset shows an FFT pattern, (b) SAED pattern for the Ge NCs and (c) EDX spectrum 83
Figure 3-4: FTIR of the butyl capped Ge NCs produced by reduction of both germanium precursors 84
Figure 3-5: XPS spectra of the butyl capped Ge NCs produced by reduction of both germanium precursors 85
Figure 3-6: (a) UV-Vis, PL and PLE spectra for Ge NCs in chloroform. (b) PL peak maximum (red squares) and intensity (blue circles) *vs*. excitation wavelength.....86
Figure 3-7: UV-Vis, PL and PLE spectra for Ge NCs produced by the reduction of a single precursor (a) *n*-butyltrichlorogermane and (b) $GeCl_4$ 86
Figure 3-8: Integrated PL intensity *vs*. absorbance for dilute dispersions of Ge NC in chloroform and 9,10-diphenylanthracene in cyclohexane. (b) PL decays of Ge NC dispersions. Inset: Table of fitted time constants and relative amplitudes 88
Figure 3-9: (a) Low magnification TEM image of epoxy terminated Ge NCs, (b) size histogram with a Gaussian curve fitted to the data, (c) HR-TEM of the NCs and (d) SAED pattern with the reflections characteristic of crystalline Ge indexed.....89
Figure 3-10: Low magnification TEM images of the NCs produced with (a) acetate terminations, (b) amine terminations, (c) carboxylic acid terminations and (d) alkyl terminations. Insets show histograms of the sizes 90
Figure 3-11: FTIR spectra for Ge NCs capped with different ligands.....91
Figure 3-12: PL spectra of Ge NCs modified with different functional groups. An excitation wavelength of 370 nm was used for all samples 92

Figure 4-1: Integrated PL intensity *vs*. absorbance for dilute dispersions of (a) 3.9 nm Ge NCs and 9,10 diphenylanthracene, (b) 6.8 nm Ge NCs and fluorescein. (c) PL decays of both NC samples and (d) long-term PL stability of both samples recorded over 6 hours 100

Figure 4-2: Normalised PL intensity of 3.9 nm and 6.8 nm Ge NCs as a function of pH 100

Figure 4-3: (a) Normalised response for the effect of various different metal ions on the Ge NC fluorescence. (Concentration of ions is 50 μM). Error bars were calculated from the standard deviation of 6 measurements (b) Time-dependent PL intensity obtained for the interaction between Ge NCs and Fe^{3+} ions. Inset shows the spectra obtained 102

Figure 4-4: (a) Representative photoluminescence spectra of Ge NCs in the presence of increasing Fe^{3+} concentrations (0-800 μM). (b) The relationship between I_0/I (red squares) and τ_0/τ (blue circles) with the concentration of Fe^{3+} ions within the range of 0-800 μM. The excitation was fixed at 340 nm for all spectra. I_0 and I are the PL intensities in the absence and presence of Fe^{3+} ions, respectively. τ_0 and τ are the lifetimes in the absence and presence of Fe^{3+} ions, respectively..... 103

Figure 4-5: I_0/I *vs*. concentration for the linear range 0 to 1 μM 104

Figure 4-6: Normalised UV-Vis spectra for the Ge NCs before, and after the addition of increasing concentrations of Fe^{3+} 105

Figure 4-7: Variation of the peak emission wavelength as a function of the Fe^{3+} concentration 106

Figure 4-8: . Photoluminescence spectra (left) and I_0/I *vs.* concentration (right) of Ge NCs measured for Fe^{3+} concentrations from 1 to 200 μM in tapwater, (a) and (b), riverwater, (c) and (d) and lakewater (e) and (f). The excitation was fixed at 340 nm for all spectra. I and I_0 are the PL intensities in the presence and absence of Fe^{3+} ions, respectively 107

Table 4-1: Determination of Fe^{3+} in real water samples 109

Figure 4-9: Normalised PL response for the PL recovery test 110

“Hope walks through the fire, faith leaps over it”

-Jim Carrey addressing the Maharishi University of Management class of 2014 when he was awarded an honorary degree

Chapter 1: Introduction

1.1 Introduction

1.1.1 Semiconductor Nanocrystals

Crystalline inorganic solids can be divided electronically into three well-known categories: metals, semiconductors (SC), and insulators. In these extended solids, atomic orbitals overlap to give nearly continuous electronic energy levels known as bands. Metals are electronically characterised by having a partially filled band; semiconductors have a filled band (the valence band) separated from the mostly empty conduction band by a bandgap (E_g), corresponding to the Highest Occupied Molecular Orbital - Lowest Unoccupied Molecular Orbital (HOMO - LUMO) energy gap for small molecules. Insulators are conceptually the same as semiconductors in their electronic structure, except that the bandgap is larger in insulators (see Figure 1-1). In terms of bandgaps, metals have a minimal bandgap; semiconductors have E_g from ~0.5 to ~3.5 eV; and insulators have E_g > 4 eV. (1 eV = 1.602×10^{-19} J). There are some key differences, however, between the electronic structure of molecules and solid-state materials such as semiconductors.

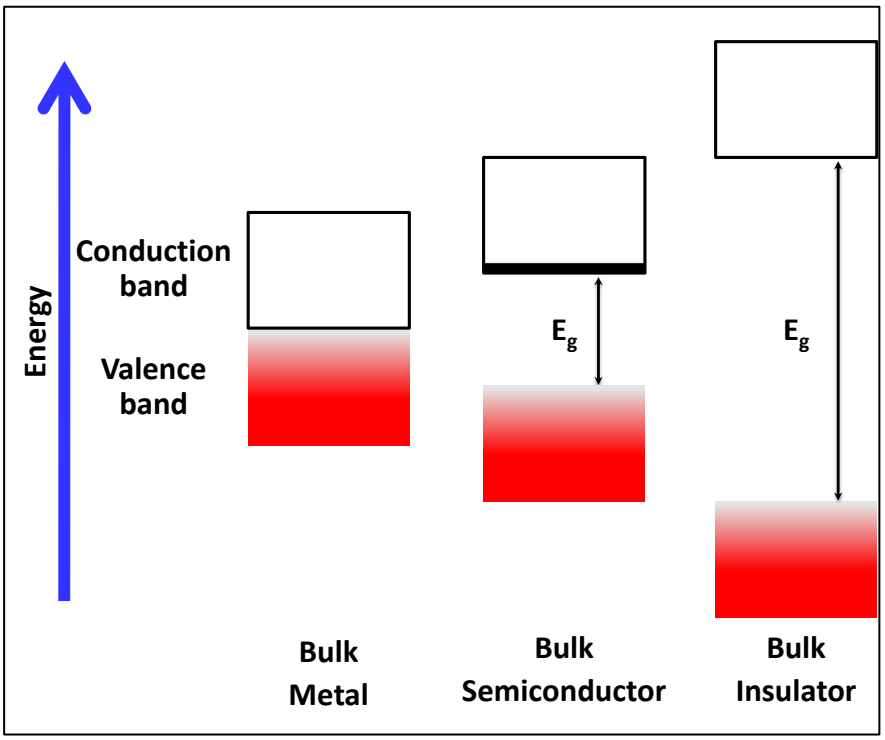


Figure 1-1: Simplified energy level diagram for metals, semiconductors and insulators. The red shaded boxes represent the filled valence bands and the white boxes represent the empty (at 0 K) conduction bands

The simplified band structure diagram in Figure 1-1 can be redrawn in terms of the wave-vector k which is related to the de Broglie wavelength by the equation: $k = \frac{2\pi}{\lambda}$. The wave-vector k can also be related to the momentum of the electron in the crystal by the equation $k = \frac{p}{\hbar}$. Hence, a plot of E *vs* k relates the available energy states for an electron to its crystal momentum. It should be emphasised that a plot of E *vs* k consists of many discrete points with each point corresponding to a possible state that is allowed to exist in the crystal. The points are so close that the $E - k$ relationship is normally drawn as a continuous curve. Semiconductors in which the lowest-energy transition does not involve a change in *k* are called ''direct bandgap'' materials (see Figure 1.2(a)); conversely, semiconductors in which the lowest-energy transition does involve a change in *k* are ''indirect bandgap'' materials, Figure 1.2(b).

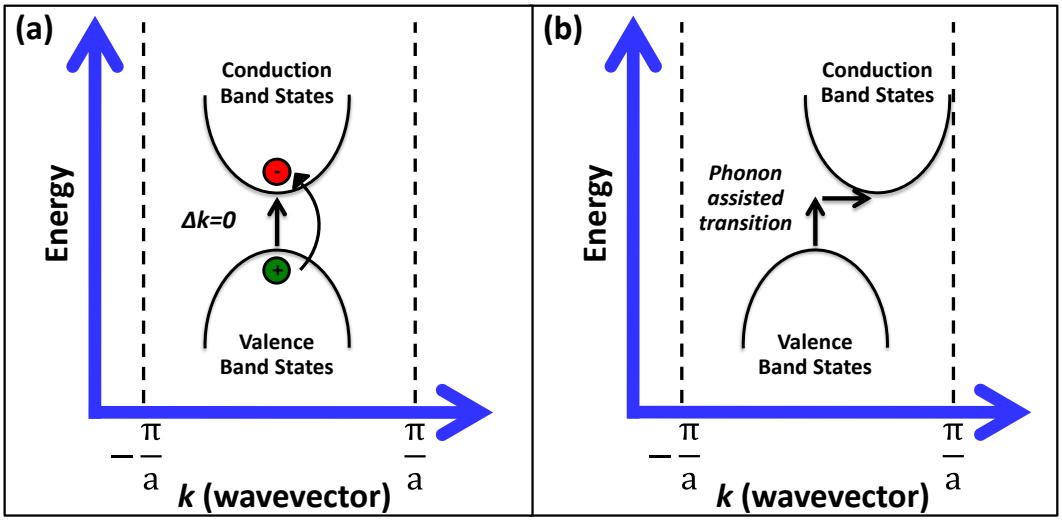


Figure 1-2: Electronic band structures for direct (a) and indirect (b) semiconductors. The straight arrows show the lowest energy transition between the valence band (bottom) and conduction band (top). A change in *k* is necessary for indirect semiconductors

Electronic transitions for which $\Delta k \neq 0$ are formally forbidden, although defects in the lattice and other reductions in symmetry may make the transitions more allowed. Silicon and germanium are both indirect bandgap materials. GaN, GaP, GaAs, InP, and InAs are III-V semiconductors, while ZnO, ZnS, CdS, CdSe, and CdTe are II-VI semiconductors and these generally have direct bandgaps.

Consider any semiconductor with a bandgap of E_g between its conduction and valence bands. If this material absorbs a photon, an electron can be promoted into the conduction band, leaving behind a hole in the valence band (see Figure 1-2(a), for the case of a direct bandgap semiconductor). This exciton (a quasi-particle consisting of an electron in the conduction band and a hole in the valence band held together by Coulombic forces) has a structure very similar to that of the hydrogen atom but usually a low binding energy due to the small effective masses. This electron/hole pair can either recombine through fluorescence, emitting a photon with energy approximately equal to E_g, or through nonradiative processes (simply put, creating heat). Taking a simple Bohr model picture of the exciton, the electron and hole orbit each other at a distance known as the Bohr exciton radius, which varies depending on the material, ranging from a few to tens of nanometres (10^{-9} m). The Bohr exciton radius is defined by a model which calculates the spatial separation between an electron and its corresponding hole, and is given by $a_{exciton} = \frac{a_0 \varepsilon_r}{\mu^*/m_e}$. Here, a_o is the Bohr radius of a hydrogen atom ($a_o = 0.529\text{Å}$), ε_r is the permittivity of the material, μ^* is the reduced mass of an exciton and m_e is the effective mass of the electron. μ^*/m_e is given as $\frac{\mu^*}{m_e} = \frac{m_e^* \times m_h^*}{m_e^* + m_h^*}$ where m_e^* is the effective mass of the electron and m_h^* is the effective mass of the hole.

In simple bulk semiconductors, an exciton is rarely observed at room temperature because the energy binding the electron to the hole is smaller than the thermal "bath" of the crystal lattice; carriers are typically free. However, consider a situation where the electrons and holes are restricted by the physical dimensions of the material. Nanocrystals (NCs), or quantum dots (QDs), are such a case; these are crystalline objects that are less than 100 nm in three dimensions. They are made up of a small number of atoms and are found in the transition region between atoms or molecules and infinitely large solids (see Figure 1-3). In a SC NC, the crystallite is so small that the excited electron and hole are physically confined to a separation smaller than their Bohr exciton radius, providing a real materials system for the quantum mechanical particle-in-a-box model. Confining the electron/hole pair to a smaller space increases the energy of the available states through what is known as

quantum confinement[1-3]. Quantum confinement can be observed once the diameter of a material is of the same magnitude as the de Broglie wavelength of the electron wave function.

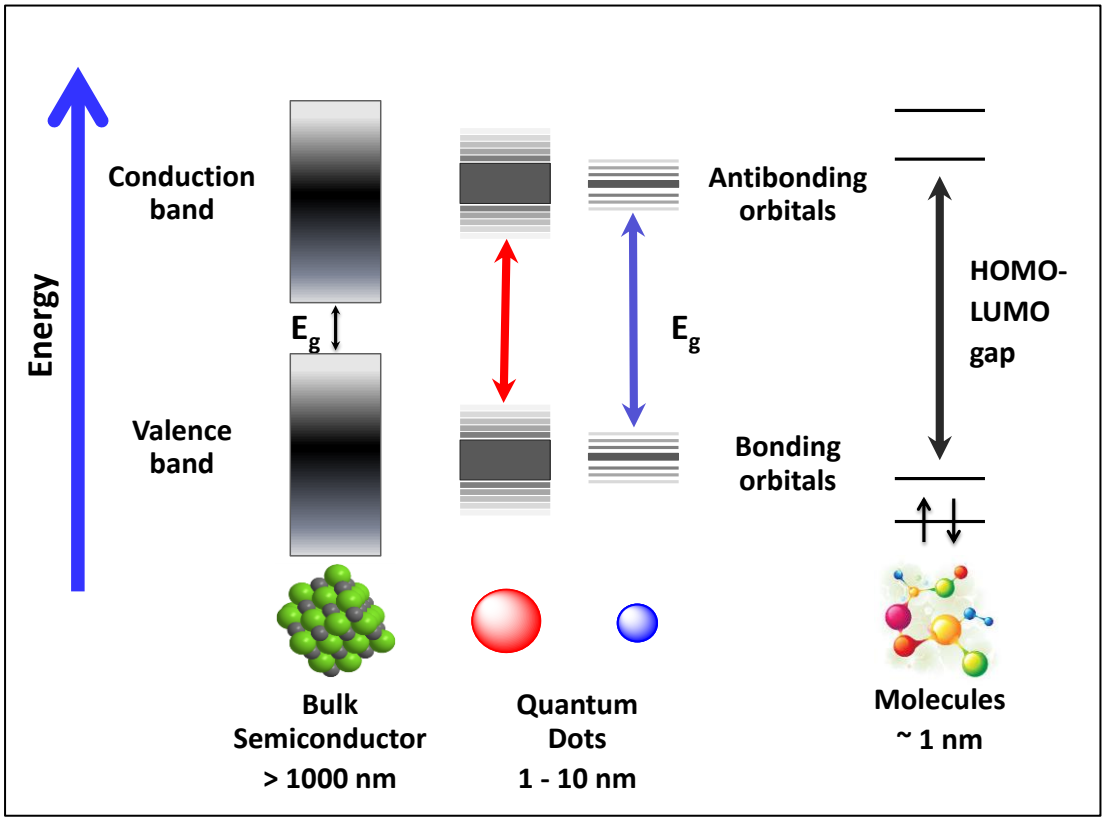


Figure 1-3: The effect of quantum confinement on the energy levels in a SC material as it goes from bulk size to nanometre sized quantum dots. Right, the energy level structure of a molecule

The net effect of this is to raise the energy band gap E_g with decreasing particle size, see Figure 1-3, therefore, the onset of light absorption shifts to shorter wavelengths. This is why the electronic, optical and structural properties can be a function of the crystallite dimensions and thus change with the radius. Since semiconductors are of widespread use in electronic and optical applications, the possibility of being able to adjust the bandgap in semiconductor nanocrystals to the required specifications by varying the size makes them extremely interesting.

Considering an electron in the conduction band and a hole in the valence band; both feel confined by the size of the particle. We can treat both like a particle in a

box: the electron and hole have discrete energy states, E, (modelling the particle as a cube, width L):[4]

$$E = \frac{h^2}{(8m^*L^2)}\left(n_x^2 + n_y^2 + n_z^2\right) \qquad \text{(Eq. 1-1)}$$

Where h is Planck's constant and m^* is the effective mass.

For the electron, the lowest energy state above the bottom of the conduction band is given as:

$$E_e = \frac{3h^2}{8m_e^*L^2} \qquad \text{(Eq. 1-2)}$$

For the hole, the lowest energy state below the top of the valence band is given as:

$$E_h = \frac{3h^2}{8m_h^*L^2} \qquad \text{(Eq. 1-3)}$$

This means that the bandgap appears bigger for a semiconducting nanocrystal compared to bulk:

$$E_{g,NC} = E_{g,bulk} + E_e + E_h \qquad \text{(Eq. 1-4)}$$

Or:

$$E_{g,NC} = E_{g,bulk} + \frac{3h^2}{8L^2}\left(\frac{1}{m_e^*} + \frac{1}{m_h^*}\right) \qquad \text{(Eq. 1-5)}$$

In reality we need to modify our rather crude equation to take into account the fact that

a) The nanoparticles are not necessarily cubes and
b) The electron and hole attract each other and so lower their energies.

This leads us to the Brus equation[4]:

$$E_{g,NC} = E_{g,bulk} + \frac{h^2}{8r^2}\left(\frac{1}{m_e^*} + \frac{1}{m_h^*}\right) - \frac{1.8e^2}{4\varepsilon_r\varepsilon_0 r} \qquad \text{(Eq. 1-6)}$$

Where r is the nanocrystal radius, e is the elementary charge, ε_0 is the permittivity of free space and ε_r is the permittivity of the material.

This formula has a simple enough interpretation; the bandgap energy of a semiconductor nanocrystal is equal to the bulk bandgap plus a quantum localisation term which describes the energy of a "pseudoelectron" of effective mass m_e^* near the bottom of the conduction band (LUMO) and the energy of a "pseudohole" of effective mass m_h^* in the valence band (HOMO). The third term describes the decrease in energy as a result of the Coulombic attraction between the electron and hole.

The Coulomb term shifts $E_{g,NC}$ to lower energy with an inverse relation to r, while the quantum localisation term shift $E_{g,NC}$ to higher energy with an inverse relation to r^2. Thus the apparent bandgap will always increase for small enough r - an effect that has now been experimentally observed for many different materials.

In the last two decades QDs have been made from a variety of semiconducting materials and are optically active from the ultraviolet to the near infrared portions of the electromagnetic spectrum (Figure 1-4(a)). CdSe and CdTe (II-VI) QDs, which emit largely in the visible region, are joined by CdS, ZnSe, and ZnS (II-VI) QDs in the ultraviolet and PbSe, PbTe, and PbS (IV-VI) QDs[5] in the near infrared. Cadmium and lead-free visible and near infrared emitting QDs are also being studied, such as InP,[6, 7] InAs,[8, 9] (though the trade-off is lower toxicity for higher expense considering the rarity of indium) and GaP[10] (III-V). Moreover, various alloys of these materials have been developed, see Figure 1-4(b), while overcoating a QD core with a wider bandgap shell material (Figure 1-4(c), inset) can further improve the stability, blinking and quantum yield (QY) of the nanocrystals. A great deal is known about how to control shape, size, surface chemistry, uniformity and these compound SC QDs are currently utilized in applications such as biological imaging,[11, 12] and optoelectronic devices.[13, 14] However, genuine concerns have been raised regarding the toxicity of these compound QDs in living systems[15] with different levels of toxicity reported in the literature.[16] Derfus *et al.* confirmed that QDs with a CdSe core and without a ZnS shell were toxic to liver cells after exposure to UV light.[17] It was shown that QDs build up in vital organs for at least 90 days once inside the body.[18] Hence, it is important to develop alternative QDs with good optical and

electrical properties but composed of materials with low toxicities. Moreover, the European Union's Restriction of Hazardous Substances Directive severely limits the use of heavy metal cations such as Cd, Pb and Hg in consumer electronics.[19]

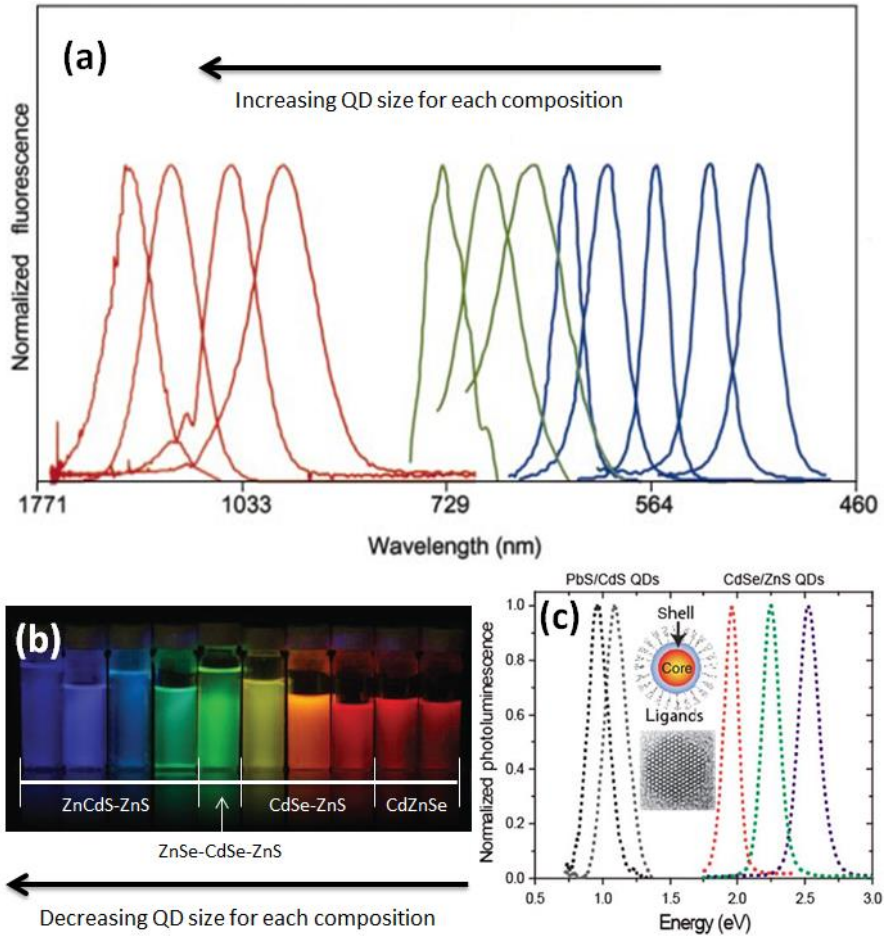


Figure 1-4: (a) Size- and material- dependent emission spectra of SC NCs. Blue curves represent different sizes of CdSe nanocrystals with diameters of 2.1, 2.4, 3.1, 3.6, and 4.6 nm (from right to left). The green series is InP NCs with diameters of 3.0, 3.5, and 4.6 nm. Red curves are InAs nanocrystals with diameters of 2.8, 3.6, 4.6, and 6.0 nm. (b) Image of solutions of colloidal QDs of various size and composition showing emission when excited with an Ultraviolet (UV) lamp. (c) Photoluminescence (PL) spectra of CdSe-ZnS and PbS-CdS core-shell QDs. The inset shows a schematic of a typical core-shell colloidal QD and a High Resolution Transmission Electron Microscopy (HRTEM) image of a CdSe NC (Part (a) adapted from ref 11 and parts (b) and (c) adapted from ref 13)

Consequently, research has concentrated on the advancement of nontoxic Group IV SC QDs. As well as their high compatibilities with current microelectronics, silicon and germanium are nontoxic, biocompatible and electrochemically stable making them ideal replacements in applications such as light-emitting diodes, solar cells,

and biosensors. Si and Ge nanocrystals exhibit reasonably strong light emission as well. Si (QY up to 25 %) and Ge QDs (QY up to 20 %) emit in the visible, although the mechanism for light emission in these nanoparticles is still not well understood.

Si and Ge are both indirect bandgap SCs with bulk Ge exhibiting a number of indirect and direct transitions in the infrared (IR) and visible spectra. While the optical properties of Si NCs have been investigated to a great extent, Ge NCs have not been investigated in as much detail. Ge is especially appealing due to the higher electron and hole mobilities (μ_e = 3900 $cm^2\ V^{-1}s^{-1}$, μ_h = 1900 $cm^2\ V^{-1}s^{-1}$) compared to Si,[20] larger dielectric constant, a large absorption coefficient (*ca.* 2 × 10^5 cm^{-1}) and narrow bulk band gap (0.67 eV at 300 K), implying the possible tuning of light emission over as much as 3.3 eV, corresponding to wavelengths from the near-UV to the near-IR (NIR). A vital difference between Si and Ge is that Ge has smaller effective masses of electrons and holes leading to a significantly larger exciton Bohr exciton radius (11.1 nm, calculated using $m_e^* = 0.12m_e$, $m_h^* = 0.21m_e$ and $\varepsilon_r = 16$) when compared to silicon (4.5 nm). The larger exciton Bohr radius means that Ge nanocrystals will impart stronger, more easily identified effects of quantum confinement than silicon for the same size nanocrystals. It is also rational that quantum confinement effects will emerge for larger Ge nanocrystal sizes than Si.[21]

1.1.2 Germanium Nanocrystals

Physical Methods

Ge NCs can be synthesised by both physical and chemical methods. Physical strategies for producing Ge NCs include chemical vapour deposition,[22] etching,[23, 24] plasma techniques,[25-28] gas-phase pyrolysis,[29] sputtering,[30-32] laser ablation,[33, 34] and ion implantation followed by high temperature annealing.[35,36] However, these techniques are expensive, difficult to scale and use extreme temperatures and pressures. Furthermore, these methods produce broad distributions of crystal sizes and broad optical absorption and photoluminescence features that make definitive interpretation in terms of quantum confinement and other mechanisms difficult. Although there are a few interesting publications based on physical methods to produce Ge NCs, the following literature review will focus only on solution based chemical methods.

Chemical Methods

Colloidal routes hold great promise for the scalable production of high-quality, solution processible NCs of numerous semiconductors. While a vast amount of research has focused on the development of compound QDs,[10] a far lesser body of work exists for the synthesis of freestanding Ge NCs, although a great deal of progress has been made.[37] The key barrier with the nucleation and growth of these materials lies in the strong covalent character of the Ge-Ge bond. Hostile experimental conditions such as elevated temperatures and the use of strong reducing agents, which are particularly dangerous and environmentally unfriendly, are necessary to facilitate crystallisation. High temperature routes are further complicated by the instability of organic reagents at elevated temperatures which can create impurities that are challenging to eliminate. Furthermore, interpretation of fluorescence spectra becomes easier said than done as reactive free radicals from the breakdown of organic solvents produce luminescence.

Metathesis reaction between $GeCl_4$ and Zintl salts

Kauzlarich and co-workers have produced numerous reports on the synthesis of Ge NCs. Early work focussed on the metathesis reaction between germanium tetrachloride ($GeCl_4$) and the Zintl salt NaGe in glyme or diglyme solutions, see Figure 1-5. Grignard reagents such as methyllithium, methylmagnesium bromide or octylmagnesium chloride were then employed to passivate the surface of the Ge NCs.[38] Later, using KGe or NaGe in glyme, di/triglyme and alkyllithium/Grignard reagents, they were able to produce different sized NCs with butyl, methyl or octyl terminations.[39] Work then turned to looking at the surface of the nanocrystals where different Grignard reagents were used to produce different passivating layers on the surface,[40] although no comparison in the optical properties was made. Another different Grignard reagent was later used and then successive reactions carried out on the surface of the NCs to produce acetal, alcohol, ester and polymer terminated NCs. Interestingly, these NCs showed very little difference in luminescence properties and this was attributed to emission from the NC core alone.[41] Ge NCs were also produced by the reduction of NaGe with ammonium bromide (NH_4Br) in 1) the solid state to give amorphous products and, 2) the

solution phase to produce crystalline NCs using 1-eicosyne as a ligand (Figure1-5(b)).[42]

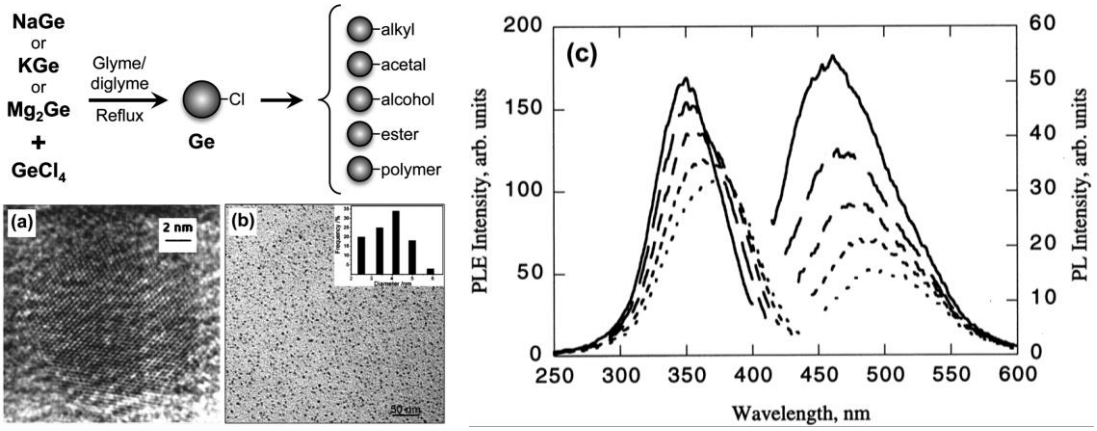


Figure 1-5: Scheme of work for the synthesis of Ge NCs *via* a metathesis reaction between Ge Zintl salts and $GeCl_4$, followed by surface modification to give different functional groups on the NC (top left). (a) HRTEM image of a 15 nm diameter Ge NC, (b) TEM image and size distribution histogram for Ge NCs synthesised by reacting NaGe and NH_4Br, and (c) photoluminescence (right) and photoluminescence excitation (PLE) (left) spectra for butyl-terminated Ge nanoparticles with an average diameter of 6.2 nm (adapted from ref 37)

Pugsley *et al.* present results of an XAS (X-ray Absorption Spectroscopy) and EXAFS (Extended X-ray Absorption Fine Structure) study on the synthesis of Ge nanoparticles formed by a metathesis reaction between Mg_2Ge (Magnesium germanide) and $GeCl_4$ in diglyme.[43] The products formed at various stages in the processing were characterised by TEM and optical spectroscopy as well as *in situ* XAS/EXAFS studies using specially designed reaction cells. It was found that after 1 h the particle size range was between 1.5 to 4.5 nm, with a mean value near 2.7 nm; after 3 h, the average size had increased to 2.9 nm and to 3.7 nm by 6h, with only a few larger particles extending up to 6 nm in dimension. From TEM, they could not conclude if the Ge nanoparticles formed by reaction were amorphous, crystalline or a mixture of both. The room temperature PL spectra excited by 325 nm laser radiation exhibited a double maximum at 430 and 510 nm. They did not observe any systematic changes in the peak position or PL intensity as a function of reaction time as the average particle size evolved from 2 to 4 nm. The PL spectra from samples containing nanocrystalline germanium oxide (GeO_2) exhibited an additional weak feature at 660 nm. *In situ* XAS/EXAFS experiments offered a new

way to monitor and determine the mechanism and kinetics of the nanoparticle formation.

Reduction, hydrolysis & condensation and decomposition of organogermanes

Heath *et al.* reported the synthesis of three different sizes of Ge NCs by the ultrasonic mediated reduction of mixtures of chlorogermanes and organochlorogermanes by an ultrafine colloidal solution of sodium/potassium alloy in heptanes followed by crystallisation in a sealed pressure bomb (by heating to 270 ^{o}C for 24-48 hours).[21] Using different reagent mixtures and amounts, Ge nanoparticles with average sizes of 6, 11, and > 20 nm were produced. Polydispersity, and a range of morphologies that included platelets, was observed, as well as evidence of oxidation after exposure to air. The authors also observed that the successful synthesis of crystalline Ge nanoparticles was dependent upon the surface capping ligands, with alkylsilanes being preferable for producing the smallest Ge nanoparticles. UV-Visible (UV-Vis) and near-infrared spectroscopy of colloidal suspensions showed evidence of quantum confinement effects, as well as absorption characteristics of the direct and indirect band gaps.

Veinot and Henderson produced Ge NCs ~6-12 nm in size by the hydrolysis and subsequent condensation of phenyl trichlorogermane using a mixture of isopropylalcohol (IPA) and water to form a sol-gel polymer, followed by thermal processing (in a slightly reducing atmosphere, 5 % H_2 / 95 % Ar) of the germanium rich oxide (GRO) bulk polymer (Figure 1-6, left).[44] With increasing processing temperature (up to and above 525 ^{o}C) and time, Ge NCs grow in the oxide network confirmed by X-Ray Diffraction (XRD), Raman, Fourier Transform Infrared (FTIR), and X-Ray Photoelectron Spectroscopies (XPS). PL spectroscopy showed emission between 390 and 440 nm with a red shift caused by increasing NC size, consistent with quantum confinement effects. The authors were able to easily liberate the NCs from the oxide matrix by dissolution in warm (60 ^{o}C) water and confirmed this by TEM and PL. Figure 1-6(a)-(c) shows that they were able to control the size of the NCs by changing the amount of time the matrix was exposed to water, with a size decrease after a longer exposure. This was confirmed by TEM and PL with a blue

shift in the emission energy for the particles that were exposed longer to water. FTIR of the liberated NCs showed oxide and hydroxide terminated surfaces.

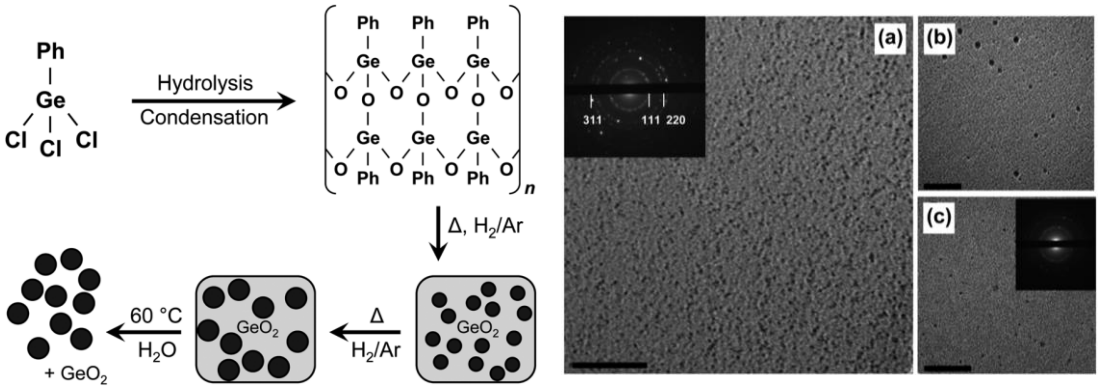


Figure 1-6: Left, schematic highlighting the synthesis of Ge nanoparticles by thermally decomposing a sol-gel-derived polymer. Right, TEM images and SAED pattern for Ge NCs liberated from a GeO_2 matrix upon dissolution in water at 60 ^{0}C for (a, b) 30 min and (c) 2.5 h. (adapted from ref 37)

Later, they investigated the atmospheric dependence of Ge NC formation and growth from thermal processing of $(C_6H_5GeO_{1.5})_n$ condensation polymers, derived from phenyl trichlorogermane.[45] By processing the germanium rich oxide in two different atmospheres, the authors were able to uncouple the disproportionation and reduction pathways for NC formation. In an inert processing atmosphere (100 % Ar), the generation of elemental Ge (at 600 ^{o}C) from thermally induced disproportionation of the GRO produced GeO_2-embedded Ge NCs as confirmed by Near-Edge X-Ray Absorption Fine Structure (NEXAFS) spectroscopy and XPS. Their size (20 nm) was found to be independent of both processing temperature and time which was verified by XRD. Processing in a slightly reducing atmosphere (5 % H_2 / 95 % Ar) activated a second Ge NC formation and growth pathway, involving the reduction of Ge oxide species as proven by NEXAFS and XPS. In this reducing atmosphere, crystalline Ge emerged for samples processed at 525 ^{o}C, while increased processing temperature and times resulted in the ability to tailor NC growth and size as shown by XRD.

In a subsequent study,[46] the phenyl group was replaced with various other substituents which allowed the processing temperature to be reduced to lower than the original phenyl GRO and as low as 300 ^{o}C for *n*-butyltrichlorogermane,

while the amount of carbonaceous impurities was also reduced. They compare processing in a reducing atmosphere (5 % H_2 / 95 % Ar) and inert atmosphere (100 % Ar) and concluded that hydrogen reduction of the oxide networks was not contributing substantially to the formation of elemental Ge. The reduction threshold for GeO_2 is 450 ^{o}C and thus formation of Ge NCs only happened by disproportionation of the precursors at lower temperatures.

Similarly Ozin and Henderson produced silicon dioxide (SiO_2)-embedded Ge NCs through thermal processing of sol-gel glasses synthesised from the co-hydrolysis and co-condensation of tetraethoxyorthogermanate (TEOG) and tetraethoxyorthosilicate (TEOS) in a 1:7 ratio.[47] FTIR and Raman confirmed the presence of Si-O-Si, Si-O-Ge and Ge-O-Ge in the intermediate copolymer. The copolymer was then heated to 700 ^{o}C in a slightly reducing atmosphere (5 % H_2 / 95 % Ar) to give a mix of bulk Ge and nanocrystalline Ge embedded in a SiO_2 matrix. The bulk Ge was selectively etched with hydrogen peroxide (H_2O_2) leaving a powder consisting exclusively of nanocrystalline Ge in SiO_2. This was confirmed by XRD. Subsequent etching with a mix of water, ethanol and HF (Hydrofluoric acid) liberated the Ge NCs and made them soluble in ethanol and methanol with "presumably" ethoxide surface passivation. PL was not observed as the diameter was bigger than the Bohr radius. Raman showed a shift to lower frequency and broadening of the optical phonon peak. The NCs were then spun cast onto Si wafers to form a film with even thickness and a high refractive index.

Korgel's group synthesised Ge NCs by decomposing the germanium precursors tetraethylgermane (TEG) or diphenylgermane (DPG) in supercritical hexane or octanol[48] and later carbon dioxide (CO_2),[49] with emission in the visible.

At around the same time, Gerion and co-workers decomposed different concentrations of pure TEG and TEG mixed with hexane or toluene at 430 ^{o}C to produce a black powder which contained Ge NCs embedded in a matrix which was then dissolved.[50] When the authors explored the reaction conditions, they found that nanocrystalline Ge is only observed above a certain concentration of TEG and above certain temperatures. When below these conditions, the reaction is difficult

to control and produces unwanted side-products which made the final products difficult to separate and purify. They also discovered that when just the pure organics are heated above 400 ^{o}C, blue emission is also observed. Due to the fact that they were not able to unambiguously assign this emission to the Ge NCs alone, they did not perform any further optical characterisation of the NC samples.

Zaitseva *et al.*[51] later expanded on this approach by the use of higher boiling point solvents and also introduced a new precursor, tetrachlorogermane (TCG). Firstly, they showed that decomposing TCG (decomposition temperature: 140 ^{o}C) in tri-*n*-octylphosphine (TOP) and tri-*n*-octylphosphine oxide (TOPO) which have boiling points from 300 ^{o}C-360 ^{o}C produced amorphous, easily oxidised Ge. Switching to boiling tri-*n*-octylamine (TOA, B.P: 384 ^{o}C) allowed for better control, producing NCs that were highly resistant to oxidation. Increasing the concentration of precursor did not noticeably affect the size but did increase the amount of final product. Changing the solvent and thus the temperature to squalene (B.P: 412 ^{o}C) allowed formation of 3 nm NCs. Increasing the precursor concentration and reaction time produced 6.6 nm NCs. TEG in squalene produced mainly nanowires (NWs) due to the higher decomposition temperature of TEG (420 ^{o}C). TEG in octacosane (B.P. 429 ^{o}C) produces NCs at 425 ^{o}C but with a low yield of product. Tri-*n*-butylphosphine (TBP) in squalene at 410 ^{o}C produced mainly NCs that are ~ 8 nm but still had NWs and larger NCs. Addition of dichlorobenzene to the initial mixture produced a smaller size distribution, and showed the possibility to control size and structure by varying surfactant/precursor mixtures. PL at 543 nm was observed in samples with NCs smaller than 4 nm but no size dependent correlation could be made due to the fact that NCs of the same size and distribution could vary in emission wavelength by up to 50 nm.

Boyle's group also have a few reports on Ge NC synthesis. A simple thermal reduction of the Ge (II) precursor $Ge[N(SiMe_3)_2]_2$, mixed with oleylamine and injected into octadecene (ODE) at 300 ^{o}C (Figure 1-7, left) produced 7 ± 4 nm Ge NCs confirmed by TEM and SAED, see Figure 1-7(a)-(c).[52] FTIR showed that oleylamine coated the NC surface and no Si was present, also confirmed by EDX. PL using 325 and 442 nm HeCd laser lines as excitation sources, Figure1-7(d), showed

emission at 375 and 500 nm corresponding to different particle sizes within the distribution.

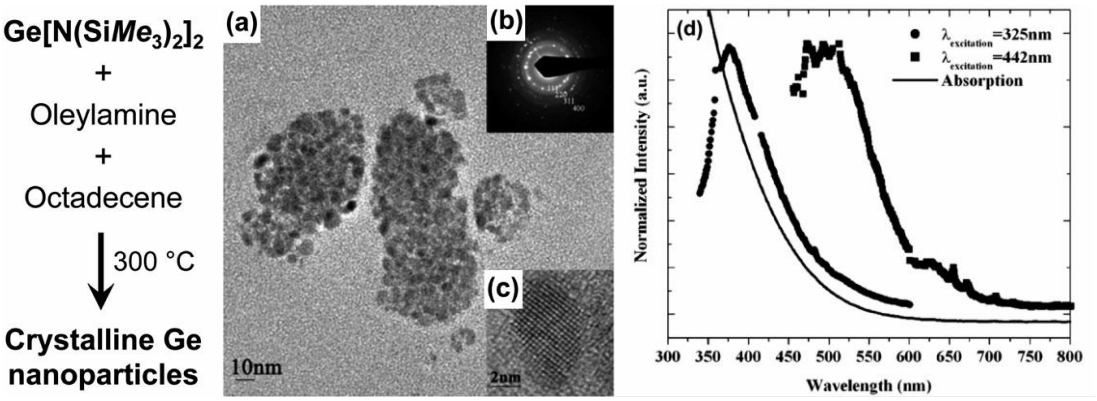


Figure 1-7: Left: the synthesis of Ge NCs by decomposing $Ge[N(SiMe_3)_2]_2$ in oleylamine and octadecene at 300 ^{0}C. (a) TEM image, (b) SAED pattern, and (c) HRTEM image of the 7 ± 4 nm Ge NCs produced. (d) Optical characterisation of Ge NCs in toluene (adapted from ref 37)

Later, Boyle again synthesised Ge NCs encapsulated with phospholipids by injecting a $Ge[N(SiMe_3)_2]_2$ precursor into hexadecylamine (HDA) heated to 300 ^{o}C under an argon atmosphere.[53] A different surface coating was prepared by exchanging the HDA for tri-*n*-octylphosphine or octadecanethiol (ODT) through treatment of a toluene or hexane solution of Ge NCs with excess TOP or ODT, and was confirmed by XPS. XPS and TEM also indicated the presence of pure Ge with some oxidation. Thermogravimetric analysis (TGA)/differential thermal analysis (DTA) conducted on particles indicated that the mass of Ge is 40 % of the total. Interestingly, functionalised Ge NCs were not luminescent enough to be useful for normal fluorescence microscopy but fluorescently labelled NCs were compatible with RBL-2H3 mast cells for at least 24 h, with less than a 2 % increase in cell death, and served as nontoxic biomarkers for cell signalling. Additionally, both organic and aqueous solutions of Ge NCs exhibited stable photothermal behaviour when excited with near-infrared radiation. These photothermal characteristics of Ge NCs compared favourably with reported values for Au nanoshells.

A series of novel germanium precursors were synthesised by Boyle and co-workers to investigate the effect of the precursors structure on the morphologies of the resulting nanomaterials.[54] This study increased the number of structurally

characterised Ge (II) precursors, including diamide, alkoxide, siloxide, silanethiolate, as well as Ge (IV) hydride-siloxide, and thiolate derivatives. The precursors were synthesised by choosing ligands of interest, which were then individually reacted with $Ge(NR_2)_2$ ($R=SiMe_3$) in toluene. The solution was stirred for 10 min, and each reaction mixture was set aside to allow the volatile component to slowly evaporate. Over an extended period of time under an argon atmosphere, light yellow or colourless X-Ray quality crystals were isolated. A mixture of these compounds with oleylamine, was injected into a solution of octadecene preheated to 325 ^{o}C. It was found that nanodots were observed for diamide, while the majority of compounds formed nanowires (alkoxides: aspect ratio = 20; siloxides: aspect ratio = 50). The results from this study indicate the "precursor structure effect" plays a role in the resulting nanoparticle morphology.

Reduction of GeX_Y (X=Cl, I, O; y=2, 4) by hydride reducing agents, sodium naphthalide and butyllithium

Wilcoxon *et al.* synthesised Ge NCs between 2 and 10 nm using inverse micelles with lithium aluminium hydride ($LiAlH_4$) as the reducing agent.[55] A High Pressure Liquid Chromatography (HPLC) apparatus with on line optical and electrical diagnostics allowed for different sizes to be separated as well as the ionic conducting by-products. The optical properties of the NCs were determined on-line without exposure to oxygen. XRD, SAED and HRTEM also confirmed that the Ge NCs retained the bulk structural properties down to at least 2 nm though broadened by the finite crystal size. The rich structure in the optical spectra was interpreted in terms of the band structure of Ge, but blue shifted by quantum confinement. Photoluminescence was observed for clusters 2-5 nm in size, in the range of 350-700 nm. Several of the peaks were tentatively attributed to specific recombination channels.

Wu *et al.* synthesised Ge NCs from 3-10 nm with narrow size distributions by the inexpensive, simple ultrasonic solution reduction of $GeCl_4$ by $LiAlH_4$, $NaBH_4$ and alkaline ($N_2H_4xH_2O$).[56] Alkaline produced the smallest NCs (3.8 ± 0.6 nm) followed by $NaBH_4$ (4.8 ± 0.7 nm) and $LiAlH_4$ gave the largest NCs (6.7 ± 0.6 nm). It was found that ultrasonic treatment resulted in smaller sizes compared to stirring treatment;

see Figure 1-8(a). When the concentration of precursor was increased, smaller sized NCs with a broader size distribution were made (3.8 ± 1.9 nm). No other characterisation was performed.

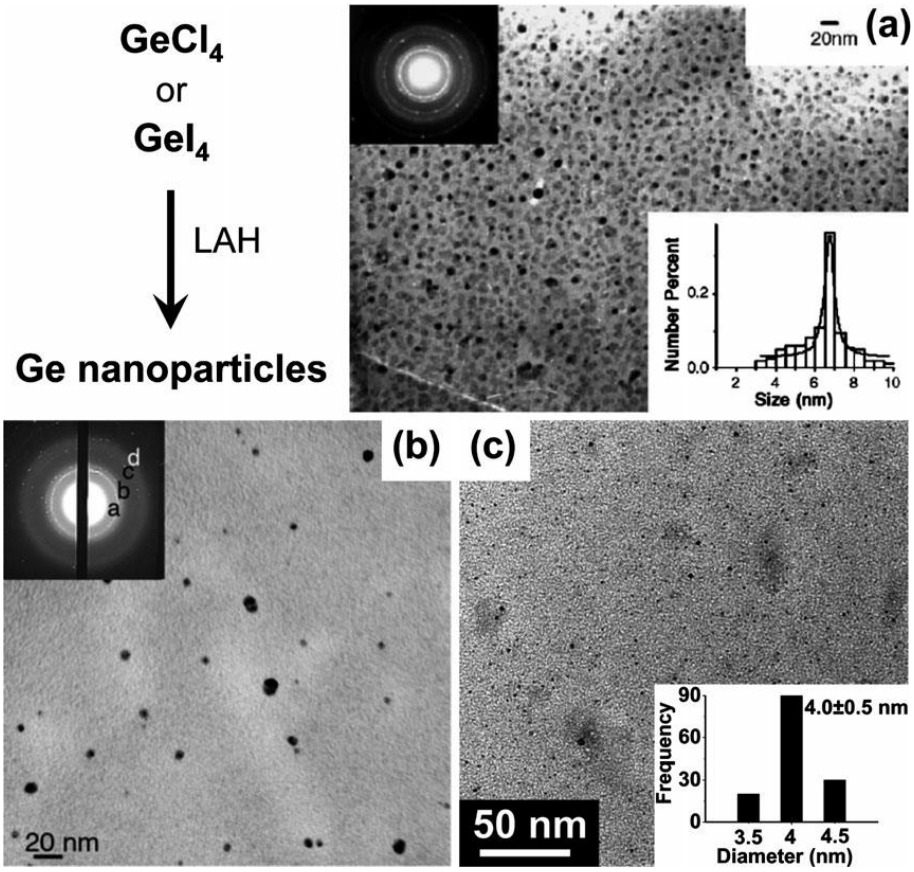


Figure 1-8: Upper left: schematic depicting the formation of Ge NCs by reducing Ge (IV) halides with $LiAlH_4$. (a) TEM image, SAED pattern, and size histogram for Ge NCs synthesised by reducing $GeCl_4$ with $LiAlH_4$ in THF and in an ultrasonic bath for 30 min. (b) TEM image and SAED pattern for *n*-undecyl terminated Ge nanoparticles synthesised by reducing GeI_4 with $LiAlH_4$ at room temperature, followed by refluxing in *n*-undecene. (c) TEM image and size histogram for 4.0 ± 0.5 nm Ge particles synthesised by reducing a toluene solution of $GeCl_4$ with $LiAlH_4$/THF at room temperature in the presence of tetraoctylammonium bromide (adapted from ref 37)

Veinot and co-workers[57] synthesised 5 nm Ge NCs by reducing a mixture of GeI_4 and CTAB (hexadecyltrimethylammonium bromide) as a surfactant with $LiAlH_4$ to produce hydride terminated NCs (Figure 1-8(b)). The intermediate here was analysed by FTIR and it was confirmed that Ge-H bonds cover the surface. A hydrogermylation reaction was then employed to produce *n*-alkyl terminated NC

surfaces with no apparent oxidation confirmed by FTIR. PL spectroscopy showed visible emission with a well-defined peak at 390 nm.

Warner and Tilley[58] produced 5 nm Ge NCs by the reduction of $GeCl_4$ with TOAB (tetraoctylammonium bromide) as a surfactant in toluene, using lithium triethylborohydride (superhydride) as the reducing agents. Chloroplatinic acid (H_2PtCl_6) was used as a catalyst to promote the reaction of the NC surface with allylamine, which produced hydrophilic surface coverage. Increasing the amount of reducing agent and adding it rapidly produced large, 50 nm triangles which did not fluoresce. UV-Vis of the small NCs showed an increasing absorption towards the UV. PL for the small NCs (excitation at 400 nm) produced green emission at 540 nm with a full width at half maximum (FWHM) of 80 nm. The quantum yield was found to be 12 %.

Tilley and co-workers reduced $GeCl_4$ in hexane and pentaethylene glycol monododecyl ether ($C_{12}E_5$) with a series of different hydride reducing agents to produce nanocrystalline Ge.[59] The NCs became larger as the strength of the reducing agent was decreased. $LiAlH_4$ produced the smallest NCs; 4 ± 0.5 nm (Figure 1-8(c)), $Li(C_2H_5)_3BH$ produced larger NCs; 4.5 ± 0.5 nm with $LiBH_4$ producing 5.5 ± 0.5 nm NCs and $NaBH_4$ produced the largest NCs; 25 ± 15 nm. PL spectroscopy showed emission in the range 420-480 nm with a blue shift in the peak position as the NC size decreased (excitation at 400 nm). A quantum yield of 11 % was obtained for the NCs. No PL was observed from the reaction with $NaBH_4$. The NCs were used a biological fluorescent imaging tags with relatively low toxicity.

Chou and Schaak[60] used a modified polyol process to synthesise Ge NCs of different size and shapes which were weakly stabilised by PVP (polyvinylpyrrolidone), thus the NPs degraded within 30-60 minutes. $GeCl_4$ and PVP in ethylene glycol were reduced by $NaBH_4$ (in trietylene glycol dimethyl ether [triglyme]). The particles were 5 ± 1 nm but amorphous (shown by XRD) and crystallised after heating to 600 ^{o}C confirmed by XRD. At higher precursor concentrations, a bimodal distribution was obtained; 8 ± 2 nm and 2.2 ± 0.7 nm. When ethanol was used as the solvent instead of ethylene glycol, larger (50 ± 18 nm), more uniform NCs were formed. Increasing

the reduction rate produced cube shaped particles which were 160 ± 30 nm in size but consisted of aggregations of smaller NCs. UV-Vis showed an intense peak at 275 nm and PL (excitation at 310 nm) showed UV emission at 352 nm.

$GeCl_4$ was reduced by naphthalide to produce a mixture of Ge NCs and polymeric side products containing Ge. Heat treatment was applied and it was discovered that a phase change from amorphous to crystalline products occurred between 550 ^oC and 600 ^oC.[61] The reaction parameters such as reductant, time, procedure, concentration and temperature were then investigated. It was found that sodium naphthalide was the best reductant, a saturation of size happened after 10 min growth time, a two pot synthesis produces smaller, more monodisperse NCs, increasing the concentration produced larger NCs and the best temperature for reaction was 0 ^oC with higher temperatures producing larger particles.[62]

Hope-Weeks[63] produced Ge NCs by the reduction of $GeCl_4$ with sodium naphthalide in 1,2-dimethoxyethane (glyme). Following reduction, *n*-butyllithium (BuLi) was employed to passivate the surface; this was confirmed by H^1 NMR (Nuclear Magnetic Resonance) and FTIR with no surface oxidation observed. By changing the growth time, the author controlled the sizes of the NCs. After 10 minutes growth, 3-7 nm NCs were formed. When the time was increased to 45 minutes, NCs between 30-49 nm were produced. TEM showed the high crystallinity of these particles. The larger particles did not fluoresce while the smaller particles showed PL in a narrow range from 360-460 nm with a maximum intensity at 380 nm (excitation at 320 nm).

Lee and Klimov[64] produced Ge NCs emitting in the IR by the reduction of germanium diiodide (GeI_2) in hexadecylamine with a mixture of *n*-butyllithium and octadecene. Heating to 300 ^oC produced 4 ± 1.7 nm NCs, see Figure 1-9. Increasing the concentration of all precursors produced larger 6.4 nm NCs. Smaller NCs were obtained when the reaction and purification steps were performed under ambient conditions. It was found that HDA is the best solvent due to the hampered solubility of GeI_2. Use of the less soluble reducing agent $LiAlH_4$ resulted in low quality NCs. ODE as a ligand was found to have the most profound effect by improving the QY

relative to TOP capped NCs. TOP capped NCs were more susceptible to oxidation as well, losing all chemical stability within 72 hours (confirmed by FTIR) and also showed far weaker PL. The absorption onset energies and PL, Figure 1-9(b), showed a blue shift with decreasing NC size (excited at 808 nm) with emission in the IR.

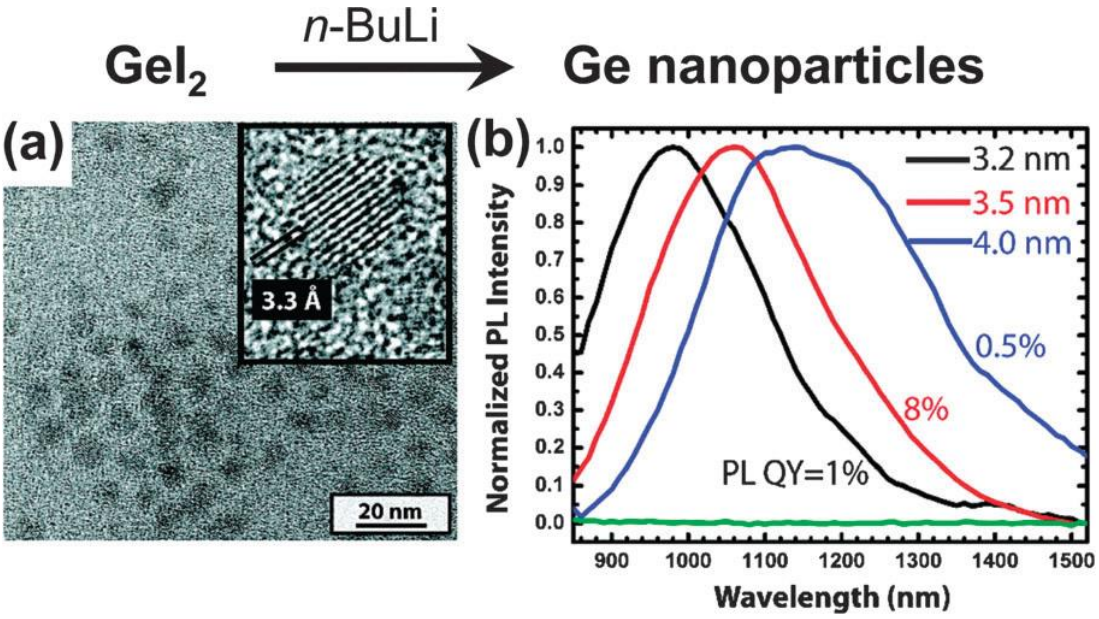


Figure 1-9: Top: schematic for the synthesis of Ge NCs by reducing GeI_2 with *n*-butyllithium. (a) TEM image of 4.0 ± 1.7 nm Ge nanoparticle, and (b) normalised photoluminescence spectra for three different sizes of octadecene-capped Ge NCs, as well as TOP-capped Ge nanoparticles (green). The excitation wavelength used was 808 nm (adapted from ref 37)

Codoluto[65] produced colloidal Ge NCs with a quantum yield of up to 8 % by the reduction of germanium (II) iodide by tert-butyllithium at high temperatures. They also performed systematic investigations of the nanocrystal nucleation and growth as a function of synthesis conditions including the nature of coordinating solvents, surface bound ligands, synthesis duration and temperature.

Ruddy[66] synthesised near infrared emitting Ge NCs with a QY below 0.1% which were apparently alkyl-terminated, by the reduction of GeI_4/GeI_2 mixtures. GeI_4/GeI_2 mixtures were dissolved in hexadecylamine, heated to 200 ^{o}C, and then reacted with *n*-butyllithium in octadecene after which the temperature was ramped to 300 ^{o}C. The size of the NCs was controlled between 2.3 and 11.3 nm by adjusting both the GeI_4/GeI_2 ratio and the temperature ramp rate. The bandgap and emission energy were found to increase with decreasing particle size.

A one step route for the apparently green synthesis of Ge NCs from GeO_2 powders an aqueous solution was performed by Wu *et al.*[67] Adding ice-cold $NaBH_4$ to GeO_2 and PVP in an aqueous solution at pH 7 and heating to 60 ^{o}C produced monodisperse Ge NCs with a diameter of 3 nm when irradiated with the TEM beam. Adding GeO_2 and PVP in an aqueous solution at pH 7 to $NaBH_4$ (the opposite of above) produced 4-6 nm NCs. When annealed at 600 ^{o}C for 1 hour under Ar gas, the NCs underwent a regrowth process and ended up 6-18 nm in size. The surfaces of these NCs were homogenous and no amorphous oxide layer was seen, also confirmed by XRD and FTIR. PL showed emission in the visible with a peak at 426 nm when excited at 370 nm which trailed off into the IR. The influence of pH, reaction time, temperature and surfactants was also investigated. When the pH was changed to 5, Ge NCs do not form and when the pH was 11, the NCs increased in size to 6-8 nm with less uniformity. Reactions below 60 ^{o}C and times from 30 minutes to 2 hours did not produce Ge NCs. Other surfactants were tried but the experiments could not obtain Ge NCs.

Korgel's group also synthesised different sized nanocrystals by reducing different concentrations of GeI_2 with $LiAlH_4$ in the coordinating solvents tri-*n*-octylphosphine and tri-*n*-butylphosphine with high yields.[68] They found that NCs produced using TBP gave larger NCs with a much larger size distribution.

One pot heat up methods

Vaughn and Schaak[69] synthesised Ge NCs of different sizes by a "one pot heat up method" in which all precursors were dissolved in a reducing solvent and heated to 260-315 ^{o}C. Oleylamine and oleic acid were added to GeI_4, followed by hexamethyldisilazane (HDMS) which played a role in the formation of Ge NCs. Without HDMS an amorphous product which was highly susceptible to oxidation formed. Figure 1-10(a)-(c) shows that by decreasing the concentration of precursor and keeping everything else the same, the size of the NCs could be decreased from 22 ± 4 nm to 12 ± 2 nm and finally 6 ± 1 nm. UV-Vis spectra showed a red shift in absorbance as the particle size increased. Adding TOP as a co-surfactant produced cube shaped NPs. When the solvent was changed to octadecene, with a stoichiometric amount of oleylamine (12:1 oleylamine:GeI_4), one dimensional

nanostructures were formed. The NCs were stable for up to 6 months confirmed by XRD, TEM, XPS and DRIFT (Diffuse Reflectance Infrared Fourier Transform) and this was attributed to a thin oxide shell on the surface that is capped by oleic acid.

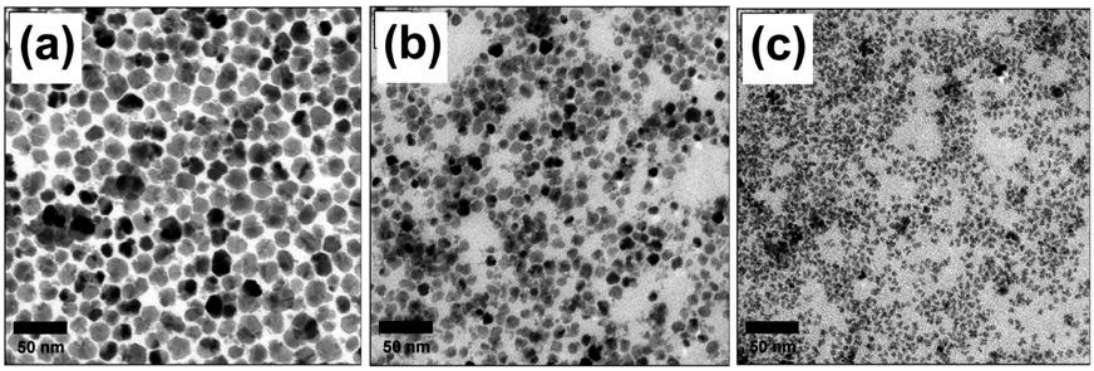


Figure 1-10: (a-c) TEM images showing the Ge nanoparticles produced by a one-pot heat-up. Decreasing the concentration of GeI_4 produced NCs with decreasing average sizes from 22 nm (a) to 6 nm (c) (adapted from ref 37)

Wang[70] produced gram scale quantities of Ge NCs by a simple inverse micelle solvothermal route. Hexane, $GeCl_4$, phenyl-$GeCl_3$, $C_{12}E_5$ and Na (25 wt. % dispersion in toluene) were inserted into a Parr reactor and heated to 280 ^{o}C for 72 hours. A black powder was collected, washed and dried at 60 ^{o}C for 12 hours. The as synthesised powder was indexed to cubic Ge by XRD and was a mixture of different shapes (sphere, triangle, hexagon) and sizes. Average particle size could not be determined from these results. By reducing the concentration of $C_{12}E_5$, NCs from 6-35 nm could be formed with uniform shape. The concentration of surfactant was also seen to have an effect on size and shape.

Kauzlarich group's most recent work[71] compares the straight forward, heat up route with microwave heating. GeI_4 and GeI_2 were mixed in different ratios, combined with oleylamine and heated. A range of different sizes from 4-11 nm was achieved by varying the precursor ratios and reaction temperature. The stability of the NCs was observed to be dependent on the NC size, with smaller nanoparticles exhibiting better stability. On exposure to ambient conditions, oxidation occurs and results in slow precipitation of the nanoparticles. The nanocrystals were well characterised by TEM and powder XRD but no PL was observed in the visible or IR and the authors hypothesise that this may be due to presence of defects on the surface.

Summarising the above syntheses, 2-8 nm Ge NCs were shown to emit from the UV to the near infrared (NIR) with a very wide range of excitation wavelengths used (310-808 nm). These reports, taken as a whole, suggest the possibility to vary the light emission of Ge NCs across a broad range. The exact mechanism behind the generation of fluorescence from Ge NCs is still debatable and the wide variety of synthetic strategies reported, together with broad particle size distributions, different ligand passivations and surface oxidation, have all contributed to the lack of agreement. A few reports demonstrate near bandgap size tuneable emission which is often attributed to pure quantum confinement within the NC core[64, 66, 72] (See Figure 1-11(a)). It is also suggested that PL is due to recombination of electron and hole at localised energy states near the nanocrystals surface, formed by either charge transfer from excitons formed within the nanocrystal core, Figure 1-11(b), or the direct generation and recombination of electron-hole pairs at surface trap states, see Figure 1-11(c). These reports have generally shown PL emission which is dependent on excitation energy.[38, 39]

A similar effect is seen for Si nanocrystals, for which a widely accepted mechanism for luminescence emission is the radiative recombination of excitons. The photophysical properties and efficiency of Ge NCs emission are not very well understood to date. Therefore, there is an urgent requirement to grow high quality, monodisperse, air stable, Ge NCs which are proccessible in a range of solvents and study their photophysical properties.

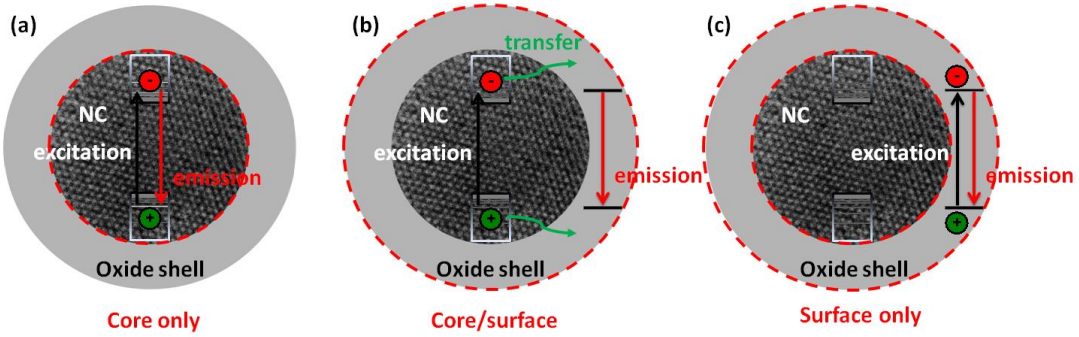


Figure 1-11: (a) Exciton recombination across the bandgap within the NC core, (b) emission resulting from transfer of excitons from the core to surface states, (c) emission resulting from the generation of excitons at the surface states of the NC

Ge NCs have lately been used in various applications such as biological imaging,[53, 59] thin films,[26, 47, 73] field effect transistors,[27] hybrid photodetectors[74] and inverse opals.[75] These applications demonstrate the versatility of this material and it could also be a promising candidate for future applications in the fields of optoelectronic devices, photovoltaics and batteries.

1.2 Metal Ion Sensing

1.2.1 Introduction

A wide variety of functional materials contain metal ions and some of these materials can be either extremely useful or detrimental in living systems and in general life worldwide. Some metal ions like mercury, lead and cadmium are harmful to the environment and human health, even at very low concentrations. Mercury, in particular is a severe neurotoxin and long term exposure to high levels of mercury can lead to damage of the brain, nervous system and immune system, while ions can accumulate environmentally through the food chain. Copper is an essential element in the body; however it can be toxic at high concentrations causing liver and kidney damage. Furthermore, some brain diseases such as Alzheimer's and Parkinson's disease are related to copper.

On the other hand, iron is a biologically important and versatile ion and is ubiquitous in living systems.[76] It plays a vital role in oxygen uptake, oxygen metabolism and electron transfer in the body. Iron is found in important compounds such as Ferritin and Transferrin which contribute to iron storage and transport in the body. Ferritin consists of a protein shell surrounding a core which contains the iron. It acts as a depot where iron can be stored inside cells in nontoxic form and subsequently released in useable form. It is found in various organs of mammals, particularly the liver, kidney and spleen, as well as in plants and bacteria. Transferrins are proteins that contain 2 similar, though not identical, sites that bind iron tightly but reversibly. It carries ingested iron from the stomach and introduces it to metabolic processes of the body, e.g. removing iron from phospahate complexes and transferring it to immature red cells which require iron. Hemoglobin and Myoglobin also contain iron (in an iron-porphyrin complex) which can directly

bind to oxygen. Hemoglobin picks up oxygen in the lungs and carries it to tissues *via* the circulatory system. Myoglobin binds and stores oxygen until it can be released to take part in metabolic processes. Iron deficiency can lead to anaemia while iron overload causes liver and kidney damage.[77, 78]

For these reasons it is critical for the environment and human health to detect metal ions. Traditional methods to detect metal ions include capillary electrophoresis,[79] electrochemical methods,[80] Atomic Absorption Spectrometry (AAS),[81] Inductively Coupled Plasma Mass Spectrometry (ICP-MS)[82] and so on. While these methods have very good detection limits, they also have limitations such as complicated processing, expensive instruments and time-consuming, complicated operations.[83, 84] Consequently, it is crucial to develop alternative methods to detect metal ions which are low in cost, simple and sensitive. The fluorescence detection of metal ions using quantum dots, or nanocrystals, has recently captured the interest of the scientific community. Photoluminescence based sensing methods allow for rapid testing and analysis, possess high sensitivity due to the low signal backgrounds and excellent signal/noise ratios inherent to this method, and are relatively simple and cost effective to carry out.

Following this principle, various QD-based optical sensors can be developed using fluorescence changes induced by direct physical adsorption or chelation of ions and small molecules on the surface of QDs. The detection of a particular ion is observed by monitoring changes in the fluorescence intensity on addition of the ion to the nanocrystals. Generally, the direct interaction of metal ions with QDs is a very complicated process and there are several interaction pathways that lead to fluorescence quenching, see Figure 1-12.

Firstly, typical metal chalcogenide-based QDs (for example, CdS, CdSe and CdTe) are formed *via* the precipitation of cations with chalcogenide anions. Consequently, those metals with lower solubility product constant (K_{SP}) values than the metal in the QD can displace the QD cations *via* cation-exchange (Figure 1-12(a)). As a result, surface defects are generated, leading to a nonradiative recombination of the

excitons and fluorescence quenching. Typical signs of the cation-exchange are a red-shift in either their absorption or PL wavelength.

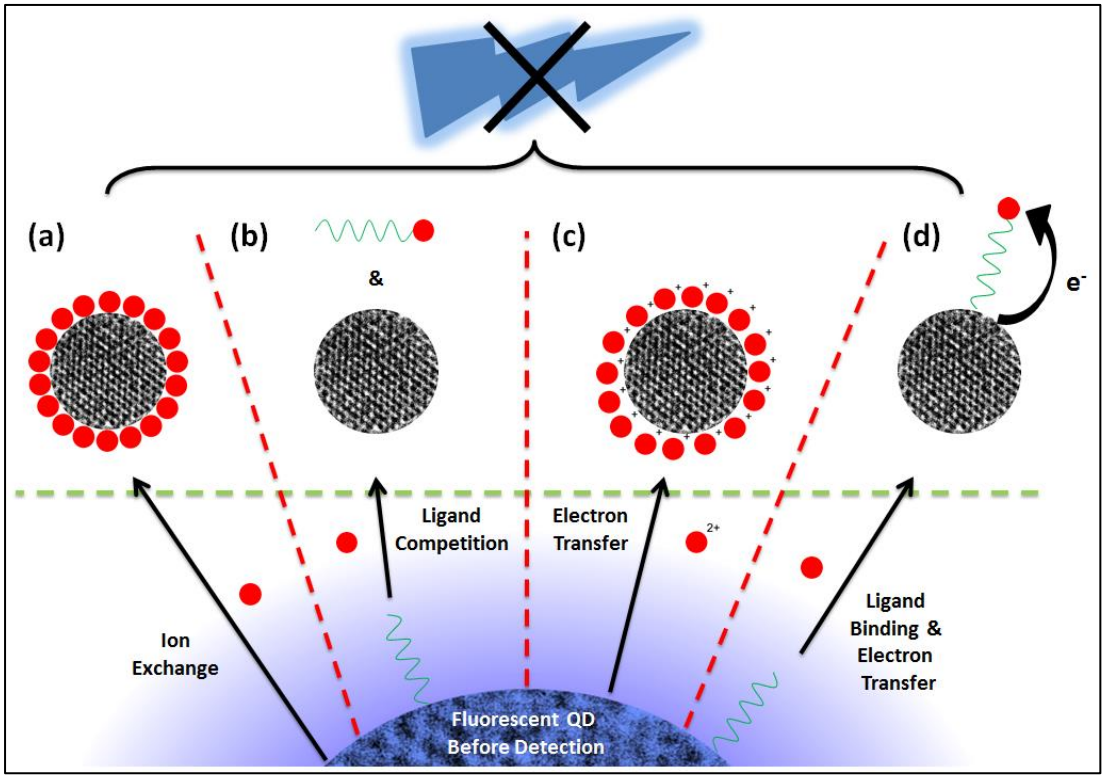


Figure 1-12: The various interaction pathways that can lead to fluorescence quenching in QDs

Ions can also compete with the typical ligands on the QD surface. After detaching the ligands from the QDs, Figure 1-12(b), surface traps can be generated which can trap electrons from the conduction band, leading to fluorescence quenching. Normally, the competition of ligands does not change the luminescent centre of the QDs, thus the PL and absorption wavelengths would not change but the result is aggregation of the QDs.

The third quenching pathway, as described by Isarov and Chrysochoos,[85] is the reduction of surface adsorbed metal ions to form nonradiative surface channels, see Figure 1-12(c). This case is primarily observed for Cu^{2+} induced quenching, in which Cu^{2+} was reduced to diamagnetic Cu^{+} by surface S^{2-} vacancies in the following way: $CdS + Cu^{2+} \rightarrow CdS^{+} + Cu^{+}$. The resultant CdS^{+}-Cu^{+} has a lower energy level than pure CdS QDs, shifting the fluorescence to longer wavelengths, together with

fluorescence quenching by Cu^{+} through a non-radiative recombination of electrons and holes.

For QDs with high density of surface ligands, the attack of the QD core by metal ions may be hindered. However, metal ions can still be adsorbed by QDs either *via* electrostatic attraction or ligand coordination. Since the metal ions are typically electron-deficient, electron transfer from the conduction band of the QDs to metal ions may occur (Figure 1-12(d)), leading to fluorescence quenching.

Although the above interaction pathways have been identified in the literature, it is still difficult to clearly attribute the interactions. The actual interactions between metal ions and QDs could well be a combination of several of the above pathways. For example authors have observed both ligand detachment and cation exchange when studying the interaction of Hg^{2+} with glutathione-capped CdTe QDs.

Fluorescence quenching refers to any process that decreases the fluorescence intensity of a sample. A variety of molecular interactions, which include energy transfer, ground state complex formation and collisional encounters, can result in quenching. Dynamic (or collisional) quenching occurs when a quencher diffuses to a luminophore during the lifetime of its excited state. Upon contact, the electron in the emissive species returns to the ground state without emission of a photon and without a change in the fluorophore's molecular structure. In static quenching, the quencher binds to the fluorescent species thus forming a complex which is nonfluorescent. Thus, both dynamic and static quenching require molecular contact between the emitter and quencher.

Dynamic quenching can be described by the Stern-Volmer equation:

$$\frac{I_0}{I} = 1 + k_q \tau_0 [Q] = 1 + K_D [Q] \qquad \text{(Eq. 1-7)}$$

Where I_0 and I are the fluorescence intensities in the absence and presence of quencher, k_q is the bimolecular rate constant, τ_0 is the lifetime of the fluorophore in the absence of quencher and $[Q]$ is the quencher concentration. The Stern-Volmer Constant, K_D is given by $K_D = k_q \tau_0$. If the quenching is known to be

dynamic, the Stern-Volmer constant will be represented by K_D, otherwise this constant will be described as K_{SV}.

For static quenching, the dependence of the fluorescence intensity on the quencher concentration is derived upon consideration of the association constant for complex formation. This constant is given by:

$$K_S = \frac{[I-Q]}{[I][Q]} \qquad \text{(Eq. 1-8)}$$

Where $[I-Q]$ is the concentration of the complex, $[I]$ is the concentration of the uncomplexed fluorophore and $[Q]$ is the concentration of the quencher.

If the complexed species is non-fluorescent then the fraction of the fluorescence that remains (I/I_0) is given by the fraction of the total fluorophores that are not complexed, $f = I/I_0$. The total concentration of fluorophore, $[I]_0$, is given by:

$$[I]_0 = [I] + [I-Q] \qquad \text{(Eq. 1-9)}$$

Substituting this into equation 1-8 gives:

$$K_S = \frac{[I]_0 - I}{[I][Q]} = \frac{[I]_0}{[I][Q]} - \frac{1}{[Q]} \qquad \text{(Eq. 1-10)}$$

Substituting in the fluorescence intensities for the fluorophore concentration and rearranging gives:

$$\frac{I_0}{I} = 1 + K_S[Q] \qquad \text{(Eq. 1-11)}$$

This equation is identical to the one for dynamic quenching, except that the quenching constant is now the association constant.

As we can see fluorescence quenching data from intensity measurements alone can be explained by either static or dynamic processes. The measurement of fluorescence lifetimes is the most definitive method to distinguish between static and dynamic quenching. Dynamic quenching affects the excited states of the fluorophores where there is an equivalent decrease in fluorescence intensity and lifetime. A decrease in lifetime occurs because dynamic quenching is an additional rate process which depopulates the excited state, hence $I_0/I = \tau_0/\tau$ (τ_0 is the

fluorescence lifetime in the absence of quencher and τ is the fluorescence lifetime in the presence of quencher). In contrast, for static quenching, the only observed fluorescence is from the uncomplexed fluorophores, which are unperturbed and therefore the lifetime is not affected (i.e. $\tau_0/\tau = 1$).

An additional way to tell apart static and dynamic quenching is by inspection of the absorption spectra of the fluorophore. Dynamic quenching only affects the excited states and so no change in the absorption spectrum is expected. On the other hand, static quenching involves ground-state complex formation which will result in alteration of the absorption spectrum of the fluorophore.

1.2.2 Review on Metal Ion Sensing

Many different compound semiconducting nanocrystal systems have been used in the detection of various ions such as Ag^{+}, Cu^{2+}, Pb^{2+}, Hg^{2+}, Cd^{2+} and Zn^{2+} *via* fluorescence measurements.

While it is important to sensitively detect these ions, the following literature review will focus on the detection of Fe^{3+} ions. Fe^{3+} is a biologically important and versatile ion, playing a vital role in oxygen uptake, oxygen metabolism and electron transfer in the body. The presence of Fe^{3+} has to be efficiently monitored as both its deficiency and overloading can induce anaemia and organ failure; hence there is on-going requirement for sensitive sensing strategies for detection of Fe^{3+} in various types of water samples (See Table 1-1 for an overview of the various probes used to detect Fe^{3+} ions to date).

The incorporation of an organic receptor onto the surface of CdSe/ZnS QDs results in a nanocrystal hybrid with selectivity for both Cu^{2+} and Fe^{3+} ions. Addition of Fe^{3+} resulted in a substantial increase in absorbance bands at 275 and 355 nm while the addition of Cu^{2+} caused a substantial bathochromic shift of both bands to 295 and 410 nm respectively. In fact these changes were so significant they could be detected by the naked eye.[86]

Au NCs were used as detecting probes for sensing Fe^{3+} ions, based on a mechanism involving particle aggregation induced fluorescence quenching by complexation of the Fe^{3+} ions in solution with the o-quinone units of the dopaquinone moieties on

the NC surface. This probe showed high selectivity towards Fe^{3+} ions, good sensitivity and was used for the detection of Fe^{3+} in tap water, lake water, and iron supplements (in tablet form).[87]

A novel fluorescent probe based on 2-(2-hydroxyphenyl)benzothiazole (HBT) was synthesised, characterised and used to sense Fe^{3+}.[88] Both UV-Vis and fluorescence spectroscopic studies demonstrated that this probe was highly sensitive and selective towards Fe^{3+} over other metal ions in acetonitrile. Upon binding with Fe^{3+}, the emission band of the probe red-shifted from 370 nm to 420 nm and the fluorescence intensity was enhanced > 103-fold. The lowest detection limit was 6.04×10^{-8} M.

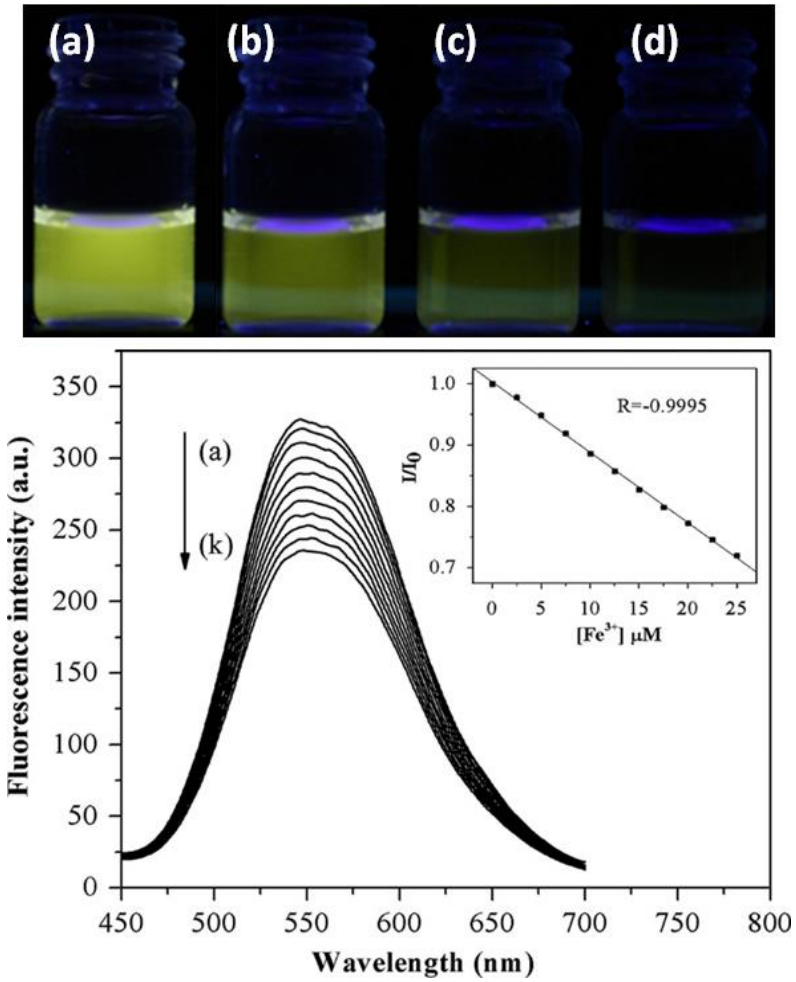


Figure 1-13: Top, visual detection of the quenching effect of Fe^{3+} on the fluorescence of the dansyl compound (a); blank, (b); 0.23 mM Fe^{3+}, (c); 0.46 mM Fe^{3+} and (d); 1 mM Fe^{3+}. Bottom, fluorescence response of the compound upon addition of (a)-(k), 0-25 µM Fe^{3+}, inset: calibration curve response from the data (adapted from ref 89)

A novel dansyl-based fluorescent probe used for the detection of Fe^{3+}.[89] It exhibited high selectivity and sensitivity towards Fe^{3+} ions. The quenching of fluorescence could be seen by eye also (Figure 1-13 (a)-(d)). The limit of detection (LOD) was found to be 0.62 µM. Recovery tests also confirmed its practical application in tap water samples.

A phosphonic acid functionalised sensor was developed for the highly sensitive and selective detection of Fe^{3+} with a detection limit of 10 nM.[90] The quenching of fluorescence was found to be due to the Fe^{3+} binding to the O atoms on the phosphonic group while the mechanism was determined to be static quenching. Various rhodamine derivatives have also been used to detect Fe^{3+}.[91-93]

Lai *et al*. used nitrogen co-doped polymer nanodots to detect Fe^{3+} over the range 0-30 µM which they say is due to the high affinity of Fe^{3+} to N and O on the nanodot surface and induces aggregation of the nanodots leading to PL quenching. They also state that quenching may lead to partial transfer of an electron in the excited state to the d orbital of Fe^{3+} but performed no lifetime measurements to confirm this. The authors suggest that both static and dynamic quenching occur here.[94]

Polymer nanodots were again used to detect Fe^{3+} with a detection limit of 1 nM.[95] The quenching was attributed to chelation of the Fe^{3+} with the surface of the nanodots which can cause photoinduced electrons to transfer from the conduction band to the Fe^{3+} thus causing quenching. They also successfully detected Fe^{3+} in lakewater. As well as these SC NC, metal nanoparticle, polymer nanodot and fluorescent molecular probes, carbon quantum dots (CQD) have also been used to detect Fe^{3+} ions.

CQDs were synthesised and used to detect Fe^{3+} with a detection limit as low as 2 nM, see Figure 1-14, right. This high sensitivity was attributed to the formation of complexes between Fe^{3+} and phenolic hydroxyls on the surface of the CQDs (Figure 1-14, left). The lifetimes in the presence and absence of Fe^{3+} confirmed a dynamic quenching mechanism.[96]

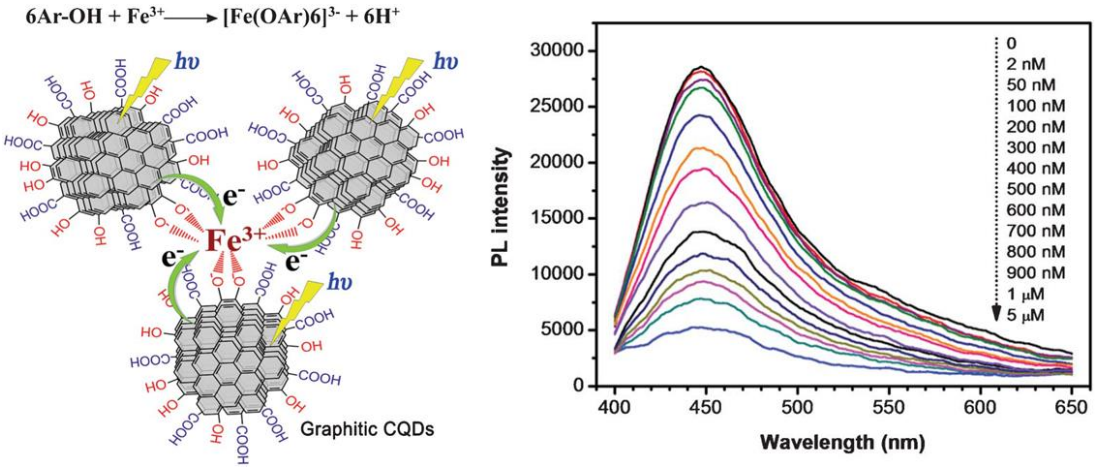


Figure 1-14: Left, Schematic illustration for the fluorescence quenching mechanism of CQDs in the presence of Fe^{3+}. The top equation shows the formation of a complex between Fe^{3+} and 6 phenolic hydroxyl groups. Right, PL spectra of the CQDs in the presence of increasing Fe^{3+} concentrations (adapted from ref 96)

CQDs were further used as a ratiometric sensor for Fe^{3+} ions with a limit of detection of 40 nM.[97] The authors contend that the quenching was caused by electron/energy transfer process occurring between the excited CQDs and the redox active metal ions. The NCs were also used to detect Fe^{3+} in lakewater samples.

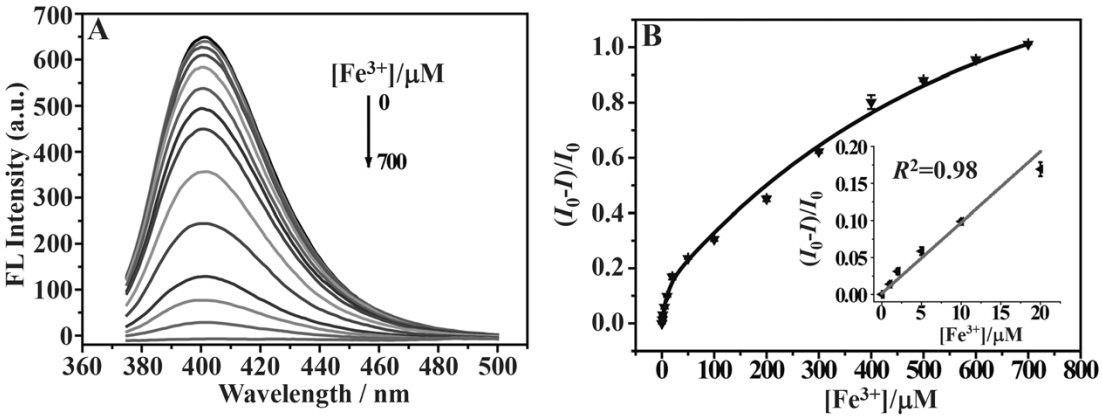


Figure 1-15: (a) Representative PL spectra of CQDs in the presence of increasing Fe^{3+} concentrations (0-700 μM). (b) The relationship between $(I_0\text{-}I)/I_0$ and Fe^{3+} from 0 to 700 μM. Inset is a linear region. I and I_0 are the PL intensities of CQDs in the presence and absence of Fe^{3+}, respectively (adapted from ref 98)

CQDs were also prepared by the hydrothermal treatment of dopamine and used to detect Fe^{3+} ions due to the special response of catechol groups on the NC surface to Fe^{3+} ions with a detection limit as low as 0.32 μm, see Figure 1-15(a) and (b). They

further examined the practicality of the assay by testing Fe^{3+} from natural water sources (lake water and tap water). The results of recovery for three samples were satisfied, thus demonstrating the applicability of the QDs.[98]

Different ionic liquids (ILs) were used to produce highly luminescent, surface-different nitrogen-doped CQDs which showed different selectivity for Cu^{2+} and Fe^{3+}. The quenching of the fluorescence was attributed to binding of the surface hydroxyl groups to Fe^{3+} which induced electron or energy transfer between the CQDs and Fe^{3+}; the LOD was determined to be 20 nM.[99] Plant leaf derived CQDs were used to sense Fe^{3+} over the concentration range 0-100 µM.[100] Ding *et al*. used doped CQDs to specifically sense Fe^{3+} over a large concentration range due to the strong interactions between the surface groups of the NCs and Fe^{3+} allowing for the transfer of photoelectrons (Figure 1-16). The LOD was calculated to be 4 µM.[101]

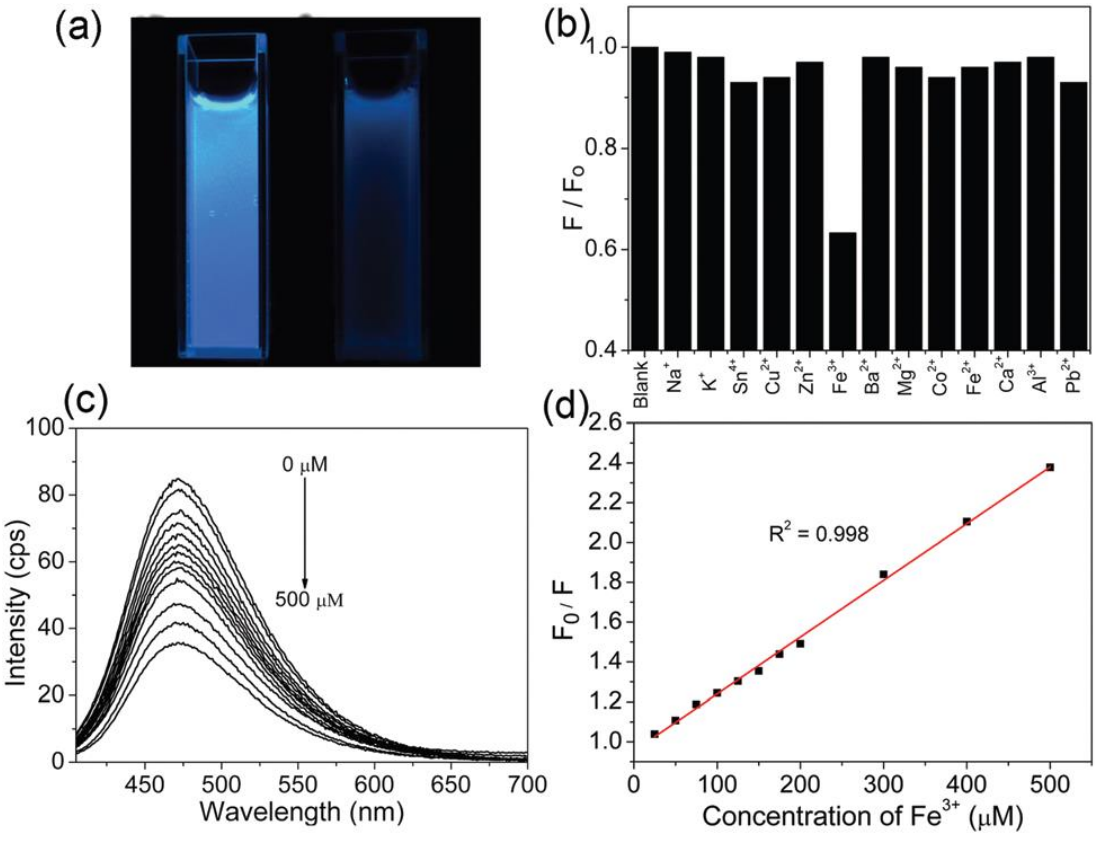


Figure 1-16: (a) Photo of CQDs without and with 300 µM Fe^{3+}. (b) Comparison of PL intensity of the CQDs after the addition of various metal ions with a concentration of 100 µM. (c) PL spectra of CQDs with increasing Fe^{3+} concentration from 0-500 µM. (d) F_0/F *vs* Fe^{3+} concentration derived from the data in (c) (adapted from ref 101)

Table 1-1: Overview of the different types of probes used in the detection of Fe^{3+} ions

Probe	QY (%)	LR (µM)	LOD (nM)	RS	Reference
CdSe/ZnS-Schiff	-	0-40	-	-	86
Au NCs	1.7	5-1280	3500	Tapwater & Lakewater	87
HBT derivative	7	0.5-4.5	60	-	88
Dansyl-derivative	38	0-25	620	Tapwater	89
Phosphonic acid-functionalised sensor	23	0.5-9	10	-	90
Polymer nanodots	13.8	0.1-10	-	-	94
Polymer nanodots	16.9	-	1	Lakewater	95
CQDs	-	0-1	2	-	96

CQDs	-	-	40	Lakewater	97
CQDs	6.4	0-20	320	Tapwater & Lakewater	98
CQDs	25.8	2 linear ranges between 0-50 µM	20	-	99
CQDs	16.4	0-100	-	-	100
CQDs	54.4	25-500	4000	-	101
CQDs	75	-	1ppm	-	102
CQDs	3.1	1-50	-	-	103
CQDs	15	1-5, 5-50	25	Lakewater	104

QY: quantum yield, LR: linear range, LOD: limit of detection, RS: real sample

The fluorescence of CQDs could be quenched by Fe^{3+} ions, due to the coordination between Fe^{3+} ions and the phenolic hydroxy groups of the CQDs.[102] Fluorescence quenching was said to contribute to ultrafast nonradiative electron-transfer that involved partial transfer of an electron in the excited state to the d orbital of Fe^{3+}. The mechanism was confirmed to be a dynamic one by lifetime measurements while the LOD was calculated to be 1 ppm, but the sensing of ions was not specific to Fe^{3+}.

Xu and co-workers produced CQDs from kitchen waste and used these NCs to sense Fe^{3+} over the concentration range 1-1000 µM. They assumed that both a static and

dynamic quenching mechanism occurred in this system but did not calculate the LOD, K_{SV}, or show lifetimes.[103]

The drawbacks of these techniques are that they often require a difficult to synthesise fluorescent probe, time-consuming sample pre- and post-treatment procedures, and sophisticated instrumentation. These studies also have several shortcomings such as limited linear ranges of detection concentrations (See Table 1-1 for examples), non-selectivity,[98-100, 102, 104-106] a lack of environmental water testing, (Table 1-1) and poor understanding of the quenching mechanism.[94, 97, 101-105]

It is noted that detection using NC systems has been carried out thus far using compound semiconductor NCs (which can contain toxic elements themselves) or carbon quantum dots. As mentioned previously, Ge NCs have many attractive properties such as their low toxicity and high quantum yield. Therefore we wanted to explore the possibility that Ge NCs could perhaps detect some metal ion.

1.3 Scope of the rest of this Thesis

The focus of this thesis is directed towards understanding the synthesis and characterisation of germanium nanocrystals in the solution phase. Using structural characterisation, the size, morphology and crystal structure of the Ge NCs is determined. Employing optical spectroscopies, the photophysical properties of different Ge NCs are examined and tuned by manipulation of the size and surface chemistry. The Ge NCs are then used as fluorescent probes for the highly selective, fast and sensitive detection of Fe^{3+} ion in aqueous solutions.

Chapter 1 starts with a general introduction to semiconductor nanocrystals or quantum dots, detailing the classic size dependent emission properties of compound materials. Examples of applications for these NCs are given as well as drawbacks for these materials. Then, an in-depth literature review for germanium nanocrystals is presented, with a focus on solution based methods. Some applications of Ge NCs are briefly discussed. The last part of this chapter gives an overview on metal ion sensing; introducing the different fluorescent quenching

pathways for sensing, a description of the quenching mechanisms, followed by a review of the literature for Fe^{3+} sensing.

Chapter 2 describes the synthesis and characterisation of size monodisperse, amine-terminated Ge NCs. A detailed characterisation of nanocrystal size, morphology, crystal phase and surface chemistry by TEM, SAED and FTIR is reported. Spectroscopic characterisation of the Ge NCs by UV/Visible absorption and photoluminescence spectroscopy, quantum yield determination and transient lifetime measurements is also presented and discussed. Spectroscopic investigation into the size dependent properties of Ge NCs, produced by separation of a polydisperse sample into discrete size fractions by centrifugation, is also reported.

Chapter 3 introduces a new method for producing alkyl-terminated colloidal Ge NCs which has numerous advantages such as short reaction time and minimal post-synthetic purification. Also described at the end of **Chapter 3** is the development of a synthetic method to control the emission properties of the Ge NCs, by variation of the functional groups (ligands) bound to the NC surface. The work in this Chapter confirms and validates the interpretation of the emission properties of the Ge NCs, which emphasises the significant role played by the NC surface in tuning the optical properties of Ge NCs, which was developed in **Chapter 2** and the beginning of **Chapter 3**.

Chapter 4 reports the application of Ge NCs as a sensing platform for the highly selective and sensitive detection of Fe^{3+} ions without the need for analyte-specific labelling groups. The Ge NCs show excellent selectivity towards Fe^{3+} ions, with no quenching of the fluorescence signal induced by the presence of Fe^{2+} ions, allowing for solution phase discrimination between ions of the same element with different formal charges. The applicability of this assay for detection of Fe^{3+} in real water samples was successfully demonstrated satisfying US Environmental Protection Agency requirements.

Chapter 5 summarises the major results and conclusions from this thesis, while the **Appendix** lists peer-reviewed publications based on this thesis, together with additional outputs based on results obtained from external research collaborations.

1.4 References

1. Rossetti, R.; Nakahara, S.; Brus, L. E., Quantum Size Effects in the Redox Potentials, Resonance Raman-Spectra, and Electronic-Spectra of CdS Crystallites in Aqueous-Solution. *J. Chem. Phys.* **1983,** *79*, 1086.

2. Rossetti, R.; Ellison, J. L.; Gibson, J. M.; Brus, L. E., Size Effects in the Excited Electronic States of Small Colloidal CdS Crystallites. *J. Chem. Phys.* **1984,** *80*, 4464.

3. Ekimov, A. I.; Efros, A. L.; Onushchenko, A. A., Quantum-Size Effect in Semiconductor Microcrystals. *Solid State Commun.* **1993,** *88*, 947.

4. Brus, L., Electronic Wave Functions in Semiconductor Clusters: Experiment and Theory. *J. Phys. Chem.* **1986,** *90*, 2555.

5. Talapin, D. V.; Lee, J.-S.; Kovalenko, M. V.; Shevchenko, E. V., Prospects of Colloidal Nanocrystals for Electronic and Optoelectronic Applications. *Chem. Rev.* **2009,** *110*, 389.

6. Liu, Z.; Kumbhar, A.; Xu, D.; Zhang, J.; Sun, Z.; Fang, J., Coreduction Colloidal Synthesis of III-V Nanocrystals: The Case of InP. *Angew. Chem. Int. Ed.* **2008,** *47*, 3540.

7. Xu, S.; Kumar, S.; Nann, T., Rapid Synthesis of High-Quality InP Nanocrystals. *J. Am. Chem. Soc.* **2006,** *128*, 1054.

8. Battaglia, D.; Peng, X. G., Formation of High Quality InP and InAs Nanocrystals in a Noncoordinating Solvent. *Nano Lett.* **2002,** *2*, 1027.

9. Xie, R.; Peng, X., Synthetic Scheme for High-Quality InAs Nanocrystals Based on Self-Focusing and One-Pot Synthesis of InAs-Based Core-Shell Nanocrystals. *Angew. Chem. Int. Ed.* **2008,** *47*, 7677.

10. Green, M., Solution Routes to III-V Semiconductor Quantum Dots. *Curr. Opin. Solid State Mater. Sci.* **2002,** *6*, 355.

11. Bruchez, M.; Moronne, M.; Gin, P.; Weiss, S.; Alivisatos, A. P., Semiconductor Nanocrystals as Fluorescent Biological Labels. *Science* **1998,** *281*, 2013.

12. Wu, X.; Liu, H.; Liu, J.; Haley, K. N.; Treadway, J. A.; Larson, J. P.; Ge, N.; Peale, F.; Bruchez, M. P., Immunofluorescent Labeling of Cancer Marker Her2 and

Other Cellular Targets with Semiconductor Quantum Dots. *Nat. Biotechnol.* **2003,** *21*, 41.

13. Shirasaki, Y.; Supran, G. J.; Bawendi, M. G.; Bulovic, V., Emergence of Colloidal Quantum-Dot Light-Emitting Technologies. *Nat. Photonics* **2013,** *7*, 13.

14. Wood, V.; Bulović, V., Colloidal Quantum Dot Light-Emitting Devices. *Nano Reviews* **2010,** *1*, 5202.

15. Winnik, F. M.; Maysinger, D., Quantum Dot Cytotoxicity and Ways to Reduce It. *Acc. Chem. Res.* **2012,** *46*, 672.

16. Bottrill, M.; Green, M., Some Aspects of Quantum Dot Toxicity. *Chem. Commun.* **2011,** *47*, 7039.

17. Derfus, A. M.; Chan, W. C. W.; Bhatia, S. N., Probing the Cytotoxicity of Semiconductor Quantum Dots. *Nano Lett.* **2003,** *4*, 11.

18. Ye, L.; Yong, K.-T.; Liu, L.; Roy, I.; Hu, R.; Zhu, J.; Cai, H.; Law, W.-C.; Liu, J.; Wang, K.; Liu, J.; Liu, Y.; Hu, Y.; Zhang, X.; Swihart, M. T.; Prasad, P. N., A Pilot Study in Non-Human Primates Shows No Adverse Response to Intravenous Injection of Quantum Dots. *Nat. Nanotechnol.* **2012,** *7*, 453.

19. www.eur-lex.europa.eu, European Parliament Directive 2002/95/EC on the Restriction of the Use of Certain Hazardous Substances in Electrical and Electronic Equipment.

20. Kamata, Y., High-*k*/Ge MOSFETS for Future Nanoelectronics. *Mater. Today* **2008,** *11*, 30.

21. Heath, J. R.; Shiang, J. J.; Alivisatos, A. P., Germanium Quantum Dots - Optical-Properties and Synthesis. *J. Chem. Phys.* **1994,** *101*, 1607.

22. Dag, O.; Kuperman, A.; Ozin, G. A., Germanium Nanoclusters - Chemical-Vapor-Deposition of Digermane in Zeolite-Y and Mordenite. *Adv. Mater.* **1994,** *6*, 147.

23. Kamins, T. I.; Ohlberg, D. A. A.; Williams, R. S.; Zhang, W.; Chou, S. Y., Positioning of Self-Assembled, Single-Crystal, Germanium Islands by Silicon Nanoimprinting. *Appl. Phys. Lett.* **1999,** *74*, 1773.

24. Kartopu, G.; Sapelkin, A. V.; Karavanskii, V. A.; Serincan, U.; Turan, R., Structural and Optical Properties of Porous Nanocrystalline Ge. *J. Appl. Phys.* **2008,** *103*.

25. Gresback, R.; Holman, Z.; Kortshagen, U., Nonthermal Plasma Synthesis of Size-Controlled, Monodisperse, Freestanding Germanium Nanocrystals. *Appl. Phys. Lett.* **2007,** *91*, 093119.

26. Holman, Z. C.; Kortshagen, U. R., Solution-Processed Germanium Nanocrystal Thin Films as Materials for Low-Cost Optical and Electronic Devices. *Langmuir* **2009,** *25*, 11883.

27. Holman, Z. C.; Liu, C.-Y.; Kortshagen, U. R., Germanium and Silicon Nanocrystal Thin-Film Field-Effect Transistors from Solution. *Nano Lett.* **2010,** *10*, 2661.

28. Holman, Z. C.; Kortshagen, U. R., Absolute Absorption Cross Sections of Ligand-Free Colloidal Germanium Nanocrystals. *Appl. Phys. Lett.* **2012,** *100*, 133108.

29. Stoldt, C. R.; Haag, M. A.; Larsen, B. A., Preparation of Freestanding Germanium Nanocrystals by Ultrasonic Aerosol Pyrolysis. *Appl. Phys. Lett.* **2008,** *93*, 043125.

30. Hayashi, S.; Fujii, M.; Yamamoto, K., Quantum Size Effects in Ge Microcrystals Embedded in SiO_2 Thin-Films. *Jpn. J. Appl. Phys., Part 2* **1989,** *28*, L1464.

31. Maeda, Y.; Tsukamoto, N.; Yazawa, Y.; Kanemitsu, Y.; Masumoto, Y., Visible Photoluminescence of Ge Microcrystals Embedded in SiO_2 Glassy Matrices. *Appl. Phys. Lett.* **1991,** *59*, 3168.

32. Zacharias, M.; Fauchet, P. M., Blue Luminescence in Films Containing Ge and GeO_2 Nanocrystals: The Role of Defects. *Appl. Phys. Lett.* **1997,** *71*, 380.

33. Ngiam, S.-T.; Jensen, K. F.; Kolenbrander, K. D., Synthesis of Ge Nanocrystals Embedded in a Si Host Matrix. *J. Appl. Phys.* **1994,** *76*, 8201.

34. Shirahata, N.; Hirakawa, D.; Masuda, Y.; Sakka, Y., Size-Dependent Color Tuning of Efficiently Luminescent Germanium Nanoparticles. *Langmuir* **2012,** *29*, 7401.

35. Nogami, M.; Abe, Y., Sol-Gel Method for Synthesizing Visible Photoluminescent Nanosized Ge-Crystal-Doped Silica Glasses. *Appl. Phys. Lett.* **1994,** *65*, 2545.

36. Zhu, J. G.; White, C. W.; Budai, J. D.; Withrow, S. P.; Chen, Y., Growth of Ge, Si, and SiGe Nanocrystals in SiO_2 Matrices. *J. Appl. Phys.* **1995,** *78*, 4386.

37. Vaughn II, D. D.; Schaak, R. E., Synthesis, Properties and Applications of Colloidal Germanium and Germanium-Based Nanomaterials. *Chem. Soc. Rev.* **2013,** *42*, 2861.

38. Taylor, B. R.; Kauzlarich, S. M.; Lee, H. W. H.; Delgado, G. R., Solution Synthesis of Germanium Nanocrystals Demonstrating Quantum Confinement. *Chem. Mater.* **1998,** *10*, 22.

39. Taylor, B. R.; Kauzlarich, S. M.; Delgado, G. R.; Lee, H. W. H., Solution Synthesis and Characterization of Quantum Confined Ge Nanoparticles. *Chem. Mater.* **1999,** *11*, 2493.

40. Taylor, B. R.; Fox, G. A.; Hope-Weeks, L. J.; Maxwell, R. S.; Kauzlarich, S. M.; Lee, H. W. H., Solution Preparation of Ge Nanoparticles with Chemically Tailored Surfaces. *Mater. Sci. Eng., B* **2002,** *96*, 90.

41. Tanke, R. S.; Kauzlarich, S. M.; Patten, T. E.; Pettigrew, K. A.; Murphy, D. L.; Thompson, M. E.; Lee, H. W. H., Synthesis of Germanium Nanoclusters with Irreversibly Attached Functional Groups: Acetals, Alcohols, Esters, and Polymers. *Chem. Mater.* **2003,** *15*, 1682.

42. Ma, X.; Wu, F.; Kauzlarich, S. M., Alkyl-Terminated Crystalline Ge Nanoparticles Prepared from NaGe: Synthesis, Functionalization and Optical Properties. *J. Solid. State. Chem.* **2008,** *181*, 1628.

43. Pugsley, A. J.; Bull, C. L.; Sella, A.; Sankar, G.; McMillan, P. F., XAS/EXAFS Studies of Ge Nanoparticles Produced by Reaction between Mg_2Ge and $GeCl_4$. *J. Solid. State. Chem.* **2011,** *184*, 2345.

44. Henderson, E. J.; Hessel, C. M.; Veinot, J. G. C., Synthesis and Photoluminescent Properties of Size-Controlled Germanium Nanocrystals from Phenyl Trichlorogermane-Derived Polymers. *J. Am. Chem. Soc.* **2008,** *130*, 3624.

45. Henderson, E. J.; Hessel, C. M.; Cavell, R. G.; Veinot, J. G. C., How Processing Atmosphere Influences the Evolution of GeO_2-Embedded Germanium Nanocrystals Obtained from the Thermolysis of Phenyl Trichlorogermane-Derived Polymers. *Chem. Mater.* **2010,** *22*, 2653.

46. Hoffman, M.; Veinot, J. G. C., Understanding the Formation of Elemental Germanium by Thermolysis of Sol-Gel Derived Organogermanium Oxide Polymers. *Chem. Mater.* **2012,** *24*, 1283.

47. Henderson, E. J.; Seino, M.; Puzzo, D. P.; Ozin, G. A., Colloidally Stable Germanium Nanocrystals for Photonic Applications. *ACS Nano* **2010,** *4*, 7683.

48. Lu, X. M.; Ziegler, K. J.; Ghezelbash, A.; Johnston, K. P.; Korgel, B. A., Synthesis of Germanium Nanocrystals in High Temperature Supercritical Fluid Solvents. *Nano Lett.* **2004,** *4*, 969.

49. Lu, X. M.; Korgel, B. A.; Johnston, K. P., Synthesis of Germanium Nanocrystals in High Temperature Supercritical CO_2. *Nanotechnology* **2005,** *16*, S389.

50. Gerion, D.; Zaitseva, N.; Saw, C.; Casula, M. F.; Fakra, S.; Van Buuren, T.; Galli, G., Solution Synthesis of Germanium Nanocrystals: Success and Open Challenges. *Nano Lett.* **2004,** *4*, 597.

51. Zaitseva, N.; Dai, Z. R.; Grant, C. D.; Harper, J.; Saw, C., Germanium Nanocrystals Synthesized in High-Boiling-Point Organic Solvents. *Chem. Mater.* **2007,** *19*, 5174.

52. Gerung, H.; Bunge, S. D.; Boyle, T. J.; Brinker, C. J.; Han, S. M., Anhydrous Solution Synthesis of Germanium Nanocrystals from the Germanium(II) Precursor $Ge[N(SiMe_3)_2]_2$. *Chem. Commun.* **2005,** 1914.

53. Lambert, T. N.; Andrews, N. L.; Gerung, H.; Boyle, T. J.; Oliver, J. M.; Wilson, B. S.; Han, S. M., Water-Soluble Germanium (0) Nanocrystals: Cell Recognition and Near-Infrared Photothermal Conversion Properties. *Small* **2007,** *3*, 691.

54. Boyle, T. J.; Tribby, L. J.; Ottley, L. A. M.; Han, S. M., Synthesis and Characterization of Germanium Coordination Compounds for Production of Germanium Nanomaterials. *Eur. J. Inorg. Chem.* **2009,** *2009*, 5550.

55. Wilcoxon, J. P.; Provencio, P. P.; Samara, G. A., Synthesis and Optical Properties of Colloidal Germanium Nanocrystals. *Phys. Rev. B* **2001,** *64*, 035417.

56. Wu, H. P.; Liu, J. F.; Wang, Y. W.; Zeng, Y. W.; Jiang, J. Z., Preparation of Ge Nanocrystals *Via* Ultrasonic Solution Reduction. *Mater. Lett.* **2006,** *60*, 986.

57. Fok, E.; Shih, M. L.; Meldrum, A.; Veinot, J. G. C., Preparation of Alkyl-Surface Functionalized Germanium Quantum Dots *Via* Thermally Initiated Hydrogermylation. *Chem. Commun.* **2004,** 386.

58. Warner, J. H.; Tilley, R. D., Synthesis of Water-Soluble Photoluminescent Germanium Nanocrystals. *Nanotechnology* **2006,** *17*, 3745.

59. Prabakar, S.; Shiohara, A.; Hanada, S.; Fujioka, K.; Yamamoto, K.; Tilley, R. D., Size Controlled Synthesis of Germanium Nanocrystals by Hydride Reducing Agents and Their Biological Applications. *Chem. Mater.* **2010,** *22*, 482.

60. Chou, N. H.; Oyler, K. D.; Motl, N. E.; Schaak, R. E., Colloidal Synthesis of Germanium Nanocrystals Using Room-Temperature Benchtop Chemistry. *Chem. Mater.* **2009,** *21*, 4105.

61. Chiu, H. W.; Chervin, C. N.; Kauzlarich, S. M., Phase Changes in Ge Nanoparticles. *Chem. Mater.* **2005,** *17*, 4858.

62. Chiu, H. W.; Kauzlarich, S. M., Investigation of Reaction Conditions for Optimal Germanium Nanoparticle Production by a Simple Reduction Route. *Chem. Mater.* **2006,** *18*, 1023.

63. Hope-Weeks, L. J., Time Dependent Size and Shape Control of Germanium Nanocrystals. *Chem. Commun.* **2003,** 2980.

64. Lee, D. C.; Pietryga, J. M.; Robel, I.; Werder, D. J.; Schaller, R. D.; Klimov, V. I., Colloidal Synthesis of Infrared-Emitting Germanium Nanocrystals. *J. Am. Chem. Soc.* **2009,** *131*, 3436.

65. Codoluto, S. C.; Baumgardner, W. J.; Hanrath, T., Fundamental Aspects of Nucleation and Growth in the Solution-Phase Synthesis of Germanium Nanocrystals. *CrystEngComm* **2010,** *12*, 2903.

66. Ruddy, D. A.; Johnson, J. C.; Smith, E. R.; Neale, N. R., Size and Bandgap Control in the Solution-Phase Synthesis of Near-Infrared-Emitting Germanium Nanocrystals. *ACS Nano* **2010,** *4*, 7459.

67. Wu, J.; Sun, Y.; Zou, R.; Song, G.; Chen, Z.; Wang, C.; Hu, J., One-Step Aqueous Solution Synthesis of Ge Nanocrystals from GeO_2 Powders. *CrystEngComm* **2011,** *13*, 3674.

68. Lu, X. M.; Korgel, B. A.; Johnston, K. P., High Yield of Germanium Nanocrystals Synthesized from Germanium Diiodide in Solution. *Chem. Mater.* **2005,** *17*, 6479.

69. Vaughn, D. D., II; Bondi, J. F.; Schaak, R. E., Colloidal Synthesis of Air-Stable Crystalline Germanium Nanoparticles with Tunable Sizes and Shapes. *Chem. Mater.* **2010,** *22*, 6103.

70. Wang, W. Z.; Poudel, B.; Huang, J. Y.; Wang, D. Z.; Kunwar, S.; Ren, Z. F., Synthesis of Gram-Scale Germanium Nanocrystals by a Low-Temperature Inverse Micelle Solvothermal Route. *Nanotechnology* **2005,** *16*, 1126.

71. Muthuswamy, E.; Iskandar, A. S.; Amador, M. M.; Kauzlarich, S. M., Facile Synthesis of Germanium Nanoparticles with Size Control: Microwave Versus Conventional Heating. *Chem. Mater.* **2012,** *25*, 1416.

72. Takeoka, S.; Fujii, M.; Hayashi, S.; Yamamoto, K., Size-Dependent Near-Infrared Photoluminescence from Ge Nanocrystals Embedded in SiO_2 Matrices. *Phys. Rev. B* **1998,** *58*, 7921.

73. Ruddy, D. A.; Erslev, P. T.; Habas, S. E.; Seabold, J. A.; Neale, N. R., Surface Chemistry Exchange of Alloyed Germanium Nanocrystals: A Pathway toward Conductive Group IV Nanocrystal Films. *J. Phys. Chem. Lett.* **2013,** *4*, 416.

74. Xue, D.-J.; Wang, J.-J.; Wang, Y.-Q.; Xin, S.; Guo, Y.-G.; Wan, L.-J., Facile Synthesis of Germanium Nanocrystals and Their Application in Organic-Inorganic Hybrid Photodetectors. *Adv. Mater.* **2011,** *23*, 3704.

75. Seino, M.; Henderson, E. J.; Puzzo, D. P.; Kadota, N.; Ozin, G. A., Germanium Nanocrystal Doped Inverse Crystalline Silicon Opal. *J. Mater. Chem.* **2011,** *21*, 15895.

76. Cotton, F. A.; Wilkinson, G., *Advanced Inorganic Chemistry*. Wiley: New York, 1989.

77. Andrews, N. C., Disorders of Iron Metabolism. *N. Engl. J. Med.* **1999,** *341*, 1986.

78. Galaris, D.; Skiada, V.; Barbouti, A., Redox Signaling and Cancer: The Role of "Labile" Iron. *Cancer Lett.* **2008,** *266*, 21.

79. Ali, I.; Aboul-Enein, H. Y., Determination of Metal Ions in Water, Soil, and Sediment by Capillary Electrophoresis. *Anal. Lett.* **2002,** *35*, 2053.

80. Aragay, G.; Merkoçi, A., Nanomaterials Application in Electrochemical Detection of Heavy Metals. *Electrochim. Acta* **2012,** *84*, 49.

81. Cizdziel, J. V.; Gerstenberger, S., Determination of Total Mercury in Human Hair and Animal Fur by Combustion Atomic Absorption Spectrometry. *Talanta* **2004,** *64*, 918.

82. T. Townsend, A.; A. Miller, K.; McLean, S.; Aldous, S., The Determination of Copper, Zinc, Cadmium and Lead in Urine by High Resolution ICP-MS. *J. Anal. At. Spectrom.* **1998,** *13*, 1213.

83. Leermakers, M.; Baeyens, W.; Quevauviller, P.; Horvat, M., Mercury in Environmental Samples: Speciation, Artifacts and Validation. *TrAC, Trends Anal. Chem.* **2005,** *24*, 383.

84. Li, Y.; Chen, C.; Li, B.; Sun, J.; Wang, J.; Gao, Y.; Zhao, Y.; Chai, Z., Elimination Efficiency of Different Reagents for the Memory Effect of Mercury Using ICP-MS. *J. Anal. At. Spectrom.* **2006,** *21*, 94.

85. Isarov, A. V.; Chrysochoos, J., Optical and Photochemical Properties of Nonstoichiometric Cadmium Sulfide Nanoparticles: Surface Modification with Copper(II) Ions. *Langmuir* **1997,** *13*, 3142.

86. Singh, N.; Mulrooney, R. C.; Kaur, N.; Callan, J. F., A Nanoparticle Based Chromogenic Chemosensor for the Simultaneous Detection of Multiple Analytes. *Chem. Commun.* **2008,** 4900.

87. Annie Ho, J.-a.; Chang, H.-C.; Su, W.-T., DOPA-Mediated Reduction Allows the Facile Synthesis of Fluorescent Gold Nanoclusters for Use as Sensing Probes for Ferric Ions. *Anal. Chem.* **2012,** *84*, 3246.

88. Liu, S.-d.; Zhang, L.-w.; Liu, X., A Highly Sensitive and Selective Fluorescent Probe for Fe^{3+} Based on 2-(2-Hydroxyphenyl)Benzothiazole. *New J. Chem.* **2013,** *37*, 821.

89. Yang, M.; Sun, M.; Zhang, Z.; Wang, S., A Novel Dansyl-Based Fluorescent Probe for Highly Selective Detection of Ferric Ions. *Talanta* **2013,** *105*, 34.

90. Zhang, Y.; Wang, G.; Zhang, J., Study on a Highly Selective Fluorescent Chemosensor for Fe^{3+} Based on 1,3,4-Oxadiazole and Phosphonic Acid. *Sensor. Actuat. B-Chem.* **2014,** *200*, 259.

91. She, M.; Yang, Z.; Yin, B.; Zhang, J.; Gu, J.; Yin, W.; Li, J.; Zhao, G.; Shi, Z., A Novel Rhodamine-Based Fluorescent and Colorimetric “Off–On” Chemosensor and Investigation of the Recognizing Behavior Towards Fe^{3+}. *Dyes Pigments* **2012,** *92*, 1337.

92. Wang, J.; Zhang, D.; Liu, Y.; Ding, P.; Wang, C.; Ye, Y.; Zhao, Y., A N-Stablization Rhodamine-Based Fluorescent Chemosensor for Fe^{3+} in Aqueous Solution and Its Application in Bioimaging. *Sensor. Actuat. B-Chem.* **2014,** *191*, 344.

93. Hu, Z.-Q.; Feng, Y.-C.; Huang, H.-Q.; Ding, L.; Wang, X.-M.; Lin, C.-S.; Li, M.; Ma, C.-P., Fe^{3+}-Selective Fluorescent Probe Based on Rhodamine B and Its Application in Bioimaging. *Sensor. Actuat. B-Chem.* **2011,** *156*, 428.

94. Lai, T.; Zheng, E.; Chen, L.; Wang, X.; Kong, L.; You, C.; Ruan, Y.; Weng, X., Hybrid Carbon Source for Producing Nitrogen-Doped Polymer Nanodots: One-Pot Hydrothermal Synthesis, Fluorescence Enhancement and Highly Selective Detection of Fe(III). *Nanoscale* **2013,** *5*, 8015.

95. Zhang, S.; Li, J.; Zeng, M.; Xu, J.; Wang, X.; Hu, W., Polymer Nanodots of Graphitic Carbon Nitride as Effective Fluorescent Probes for the Detection of Fe^{3+} and Cu^{2+} Ions. *Nanoscale* **2014,** *6*, 4157.

96. Zhang, Y.-L.; Wang, L.; Zhang, H.-C.; Liu, Y.; Wang, H.-Y.; Kang, Z.-H.; Lee, S.-T., Graphitic Carbon Quantum Dots as a Fluorescent Sensing Platform for Highly Efficient Detection of Fe^{3+} Ions. *RSC Adv.* **2013,** *3*, 3733.

97. Qu, S.; Chen, H.; Zheng, X.; Cao, J.; Liu, X., Ratiometric Fluorescent Nanosensor Based on Water Soluble Carbon Nanodots with Multiple Sensing Capacities. *Nanoscale* **2013,** *5*, 5514.

98. Qu, K.; Wang, J.; Ren, J.; Qu, X., Carbon Dots Prepared by Hydrothermal Treatment of Dopamine as an Effective Fluorescent Sensing Platform for the Label-Free Detection of Iron(II) Ions and Dopamine. *Chem. Eur. J.* **2013,** *19*, 7243.

99. Zhao, A.; Zhao, C.; Li, M.; Ren, J.; Qu, X., Ionic Liquids as Precursors for Highly Luminescent, Surface-Different Nitrogen-Doped Carbon Dots Used for Label-Free Detection of Cu^{2+}/Fe^{3+} and Cell Imaging. *Anal. Chim. Acta* **2014,** *809*, 128.

100. Zhu, L.; Yin, Y.; Wang, C.-F.; Chen, S., Plant Leaf-Derived Fluorescent Carbon Dots for Sensing, Patterning and Coding. *J. Mater. Chem. C* **2013,** *1*, 4925.

101. Ding, H.; Wei, J.-S.; Xiong, H.-M., Nitrogen and Sulfur Co-Doped Carbon Dots with Strong Blue Luminescence. *Nanoscale* **2014,** *6*, 13817.

102. Zhu, S.; Meng, Q.; Wang, L.; Zhang, J.; Song, Y.; Jin, H.; Zhang, K.; Sun, H.; Wang, H.; Yang, B., Highly Photoluminescent Carbon Dots for Multicolor Patterning, Sensors, and Bioimaging. *Angew. Chem. Int. Ed.* **2013,** *52*, 3953.

103. Xu, J.; Lai, T.; Feng, Z.; Weng, X.; Huang, C., Formation of Fluorescent Carbon Nanodots from Kitchen Wastes and Their Application for Detection of Fe^{3+}. *Luminescence* **2014**.

104. Xu, J.; Zhou, Y.; Liu, S.; Dong, M.; Huang, C., Low-Cost Synthesis of Carbon Nanodots from Natural Products Used as a Fluorescent Probe for the Detection of Ferrum(III) Ions in Lake Water. *Anal. Methods* **2014,** *6*, 2086.

105. Li, W.; Zhang, Z.; Kong, B.; Feng, S.; Wang, J.; Wang, L.; Yang, J.; Zhang, F.; Wu, P.; Zhao, D., Simple and Green Synthesis of Nitrogen-Doped Photoluminescent Carbonaceous Nanospheres for Bioimaging. *Angew. Chem. Int. Ed.* **2013,** *52*, 8151.

106. Liu, L. Q.; Li, Y. F.; Zhan, L.; Liu, Y.; Huang, C. Z., One-Step Synthesis of Fluorescent Hydroxyls-Coated Carbon Dots with Hydrothermal Reaction and Its Application to Optical Sensing of Metal Ions. *Sci. China-Chem.* **2011,** *54*, 1342.

Chapter 2: Synthesis & Characterisation of Germanium Nanocrystals

2.1 Introduction

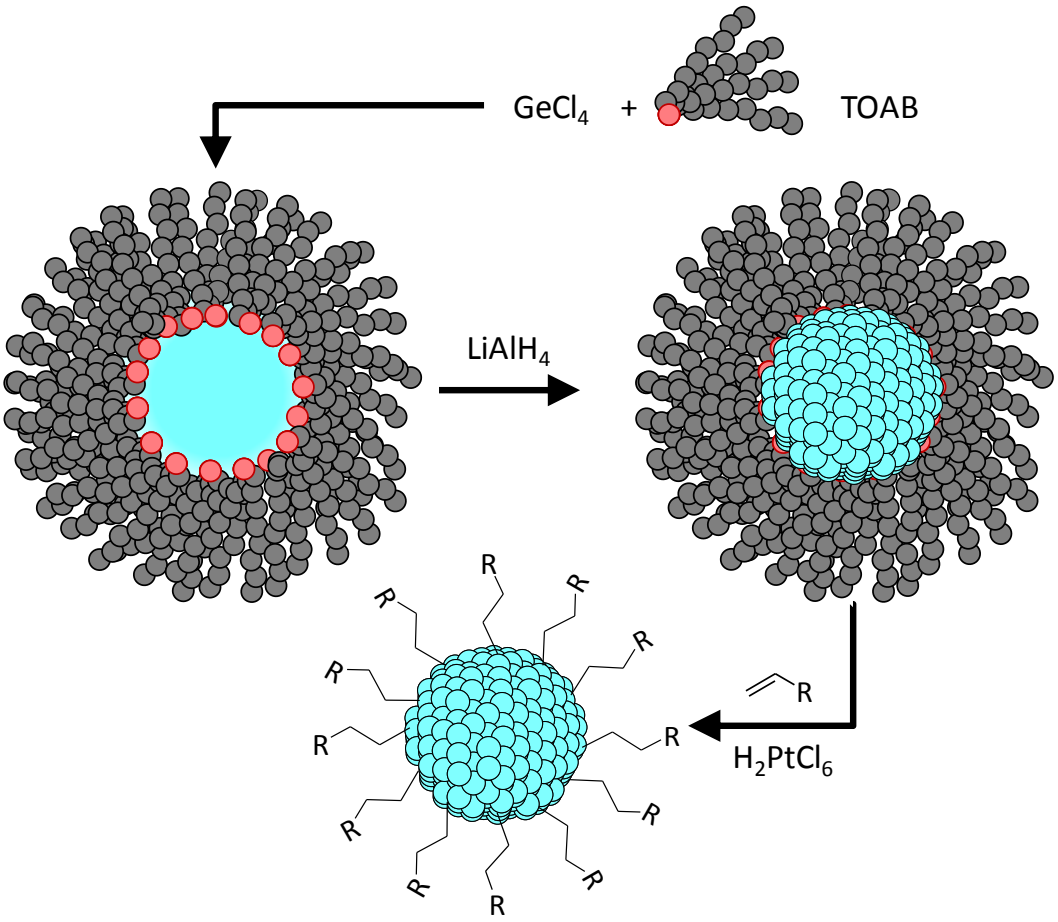
In this chapter, we report the room-temperature synthesis of size monodisperse amine-terminated Ge NCs within inverse micelles, with well-defined core diameters that may be tuned from 3.5 to 4.5 nm. These NCs are readily dispersed in water, acetonitrile, ethanol, chloroform and other polar organic solvents, making them amenable to low cost, solution based device processing. Regulation of the Ge NCs size was achieved by variation of the cationic quaternary ammonium salts used to form the inverse micelles. These Ge NCs exhibit a strong, narrow luminescence with a transition from primarily blue to green emission as the NC diameter increases from 3.5 to 4.5 nm.

Also reported here is the production of a polydisperse sample which showed a mixture of blue and green emission. We were subsequently able to easily separate this sample into two discrete size ranges, the smaller NCs showing only blue emission while the larger NCs showed only green emission. Lifetime measurements showed the presence of nanosecond components, consistent with recombination of excitons at energy states present at the nanocrystal surface, while both fractions showed good long-term PL stability.

2.2 Experimental Section

2.2.1 Synthesis and Purification of Amine Terminated Ge NCs

The synthesis of Ge NCs is adapted from the procedure reported by Warner and co-workers,[1] please see Scheme 2-1 and Table 2-1, entries 1-4 for synthetic conditions used. This method uses an inverse micelle synthetic scheme, which acts as nanoscale “reaction vessels”, within which the nanocrystals are formed by reduction of a germanium halide precursor by a hydride reducing agent. At this stage of the reaction, the Ge NCs are terminated by hydride and encapsulated within the surfactant micelle. The surface of the NCs may then be chemically passivated using a Pt-catalysed hydrogermylation reaction to form covalent germanium-carbon bonds. Depending on the choice of ligand, the NCs can be dispersed in either polar or non-polar media.



Scheme 2-1: Depiction of the different steps involved in the synthesis of Ge NCs

Chemicals. Tetrabutylammonium bromide (TBAB) (98 %), tetrahexylammonium bromide (THAB) (99 %), tetraoctylammonium bromide (TOAB) (98 %), tetrakis(decyl)ammonium bromide (TKAB) (98 %), tetrahexadecylammonium bromide (THDAB) (98 %), 9,10-diphenylanthracene (97 %), fluorescein (for fluorescence), cyclohexane (CHROMASOLV Plus, for HPLC, ≥ 99.9 %), sodium hydroxide (NaOH) (BioUltra, for luminescence, ≥ 98.0 %), sulphuric acid (95-97 %) and hydrogen peroxide (30 % v/v) were purchased from Sigma Aldrich Ltd. and stored in an ambient atmosphere. Germanium tetrachloride ($GeCl_4$) (99.99 %), chloroplatinic acid (H_2PtCl_6) (≥ 99.9 %), lithium aluminium hydride ($LiAlH_4$) (1M in THF), allylamine (≥ 99 %), toluene (99.8 %, anhydrous), methanol (99.8 %, anhydrous) and propan-2-ol (99.5 %, anhydrous) were purchased from Sigma Aldrich Ltd. and stored under inert atmosphere before use. All materials and solvents were used as received.

Synthesis and Purification. All synthetic manipulations were carried out in an inert atmosphere glove box. All glassware used was thoroughly cleaned by soaking in a base bath overnight, followed by immersion in piranha solution (3:1 concentrated sulphuric acid : 30 % hydrogen peroxide) for 20 minutes. *Caution: piranha solution is a strong oxidizing agent and should be handled with extreme care*. In a typical preparation, 2.74 mmol of the surfactant was dissolved in 60 mL toluene in a 2-neck round bottomed flask with continuous stirring. 0.1 mL (0.876 mmol) $GeCl_4$ was then added to the solution and left to stir for 30 min. Ge NCs were formed by the drop wise addition of 2 mL of $LiAlH_4$ over a period of 2 minutes. *Caution: germane gas, which is pyrophoric and highly toxic, could be evolved at this stage of the reaction and care should be taken to prevent exposure to air.*[2] The solution was then left to stir for 2.5 h. The excess reducing agent was then quenched with the addition of 20 mL methanol. At this stage of the reaction the Ge NCs are terminated by hydride and encapsulated within the inverse micelle.

Chemically passivated nanocrystals were formed by modifying the germanium-hydrogen bonds at the surface *via* the addition of 0.5 mL of 0.1 M chloroplatinic acid in propan-2-ol as a catalyst, followed by 2 mL of allylamine. After stirring for 2.5 h, the amine-terminated Ge NCs were removed from the glove box and the organic solvent removed by rotary evaporation. The resulting brown dry powder (consisting of surfactant and Ge NCs) was then re-dispersed in 40 mL deionised (DI) water (18.2 MΩ cm) and sonicated for 20 min. The solution was first filtered using filter paper and then PTFE membrane filters (Acrodisc, 0.45 μM) to remove the surfactant. Amine-terminated Ge NCs remain in the water phase. The Ge NCs were further purified by chromatography. The solution was concentrated down to *ca.* 1.5 mL and loaded into the column (ϕ = 1 cm, Length = 47.0 cm). Sephadex gel LH-20 was used as the stationary phase: fractions of *ca.* 3 mL were collected at a drop rate of approximately 1 drop every 25 seconds. The fractions were then combined and concentrated down to *ca.* 5 mL.

2.2.2 Characterisation

Structural Characterisation

TEM images and SAED patterns were acquired using a high-resolution JEOL 2100 electron microscope, equipped with a LaB_6 thermionic emission filament and Gatan DualVision 600 Charge-Coupled Device (CCD), operating at an accelerating voltage of 200 keV. TEM samples were prepared by depositing a 40 µL aliquot of the Ge NC dispersion onto a holey carbon coated copper grid (300 mesh, #S147-3, Agar Scientific), which was allowed to evaporate under ambient conditions. Data for size distribution histograms was acquired by analysis of TEM images of exactly 300 NCs located at different regions of the grid. NC diameter was determined by manual inspection of the digital images; in the case of anisotropic structures, the diameter was determined using the longest axis. EDX spectra were taken using an Oxford INCA x-sight detection spectrometer. Spectra were obtained from an area of the grid where there was a large amount of NCs. A process time of 3-4 seconds was used and the spectra obtained using an integration time of 40 s.

Optical Characterisation

FTIR spectra were recorded on a Perkin-Elmer Two spectrometer. Spectra were recorded on aliquots of Ge NCs dispersed in chloroform in a liquid cell with CaF_2 plates. UV-Vis absorption spectra were recorded using a Shimadzu UV PC-2401 spectrophotometer equipped with a 60 mm integrating sphere (ISR-240A, Shimadzu). Spectra were recorded at room temperature using a quartz cuvette (1 cm) and corrected for the solvent absorption. PL spectra were recorded using an Agilent Cary Eclipse spectrophotometer. Long-term PL stability measurements were carried out over 6 hours on the same spectrophotometer. Excitation wavelengths of 340 nm for the blue emitting Ge NCs and 400 nm for the green emitting sample were used.

Lifetimes

PL lifetime measurements were recorded on a scanning confocal fluorescence microscope (MicroTime 200, PicoQuant GmbH) equipped with a TimeHarp 200 TCSPC (Time Correlated Single Photon Counting) board. NC samples were excited in solution using a 402 nm pulsed diode laser (10 MHz; 70 ps pulse duration, LDH-P-C-

400) that was spectrally filtered using a 405 nm band-pass filter (Z405/10x, Chroma Technology Corp.). A 50x objective (0.5 NA; LM Plan FL, Olympus Corp.) was used for focusing the excitation light onto the NC dispersion and collecting the resultant fluorescence, which was directed onto an avalanche photodiode (APD; SPCM-AQR-14, Perkin-Elmer, Inc.). Backscattered excitation light was blocked with a 410 nm long-pass filter placed in the collection path (3RD410LP, Omega Optical). The excitation power was adjusted to maintain a count rate of < 10^4 counts s^{-1} at the APD in order to preserve single photon counting statistics. All emission lifetimes were fitted to a weighted multi-exponential model on FluoFit 4.2 software (PicoQuant GmbH). All lifetimes were fitted with a χ^2 value of less than 1.1

Determination of the Quantum Yield

The QY of the Ge NCs was determined using established literature methods.[3, 4] All glassware was thoroughly washed with acetone, methanol, DI water and rinsed with the solvent used in the measurements. Solutions were prepared with optical densities between 0.01-0.1 to minimise the "inner filter" (self-quenching) effects. Quantum yields were determined by comparison of the integrated fluorescence intensities of the Ge NCs with solutions of the reference emitters 9,10-diphenylanthracene in cyclohexane and fluorescein in 0.1 M NaOH with similar optical densities. The quantum yields were calculated using the formula:

$$QY_S = QY_R \times \frac{m_S}{m_R} \times \frac{n_S}{n_R}$$

Where QY_S is the quantum yield of the sample, QY_R is the quantum yield of the reference emitter, m_S and m_R are the slopes of the linear fits to plots of the integrated intensity *vs* absorbance of the sample and reference emitter, while n_S and n_R are the refractive indices of the sample solvent and the reference solvent, respectively.

PL spectra of the Ge NCs and the reference emitter were acquired using an appropriate excitation wavelength, and the total PL intensity integrated over a suitable range for each set of NCs and reference emitters, see Figure 2-1(a) for an example of 9,10-diphenylanthracene. This was repeated for various solutions with different concentrations, and the integrated fluorescence intensity plotted against

the solution absorbance (Figure 2-1(b)). The slopes (m_S and m_R, for the sample and reference material, respectively) were determined using a linear least squares fitting with a correlation coefficient of $R^2 \geq 0.99$.

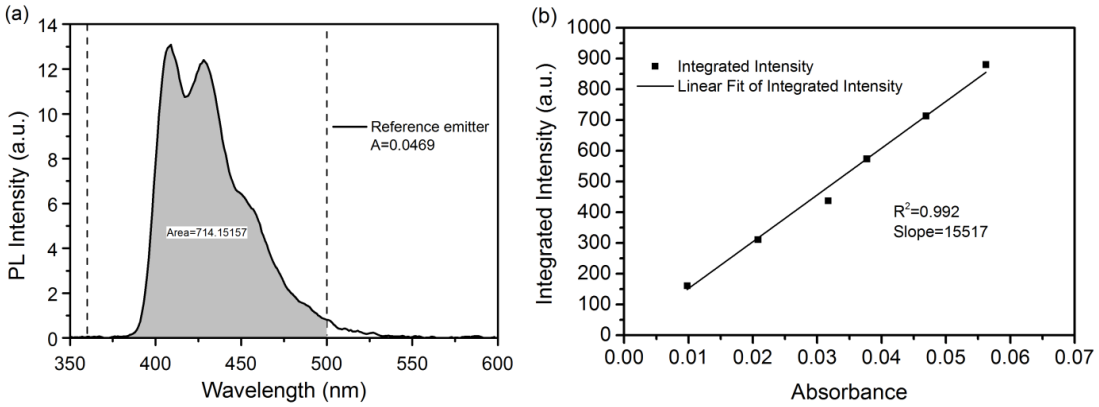


Figure 2-1: (a) The fluorescence spectrum of 9,10 diphenylanthracene showing absorbance value, integration range and integrated intensity. (b) Plot of integrated intensity *vs* absorbance for various dilutions of the reference material with a linear fit to the data

Table 2-1: Synthetic conditions for the reactions carried out in this section

Entry	Precursor (Amount)	Surfactant (Amount)	Reducing Agent (Amount)	Catalyst (Amount)	Ligand (Amount)	Extracted to
1	$GeCl_4$ (0.876 mmol)	TBAB (2.74 mmol)	$LiAlH_4$ (2 mmol)	H_2PtCl_6 (0.5 mL of a 0.1 M soln.)	Allylamine (2 mL)	Water
2	"	THAB (2.74 mmol)	"	"	"	"
3	"	TOAB (2.74 mmol)	"	"	"	"
4	"	TKAB (2.74 mmol)	"	"	"	"
5	"	THDAB (2.74 mmol)	"	"	"	"

TBAB: tetrabutylammonium bromide, THAB: tetrahexylammonium bromide, TOAB: tetraoctylammonium bromide, TKAB: tetra(kis)decylammonium bromide, THDAB: tetrahexadecylammonium bromide.

2.3 Results and Discussion

2.3.1 Amine Terminated Ge NCs

Amine-terminated Ge NCs were synthesised by room temperature reduction of $GeCl_4$ by $LiAlH_4$ under an inert atmosphere; see Experimental Section for further details**.** Figure 2-3 shows low magnification TEM images of Ge NCs prepared in the presence of the cationic quaternary ammonium salts TBAB, THAB, TOAB, TKAB, see Figure 2-2 for chemical structures of these surfactants.

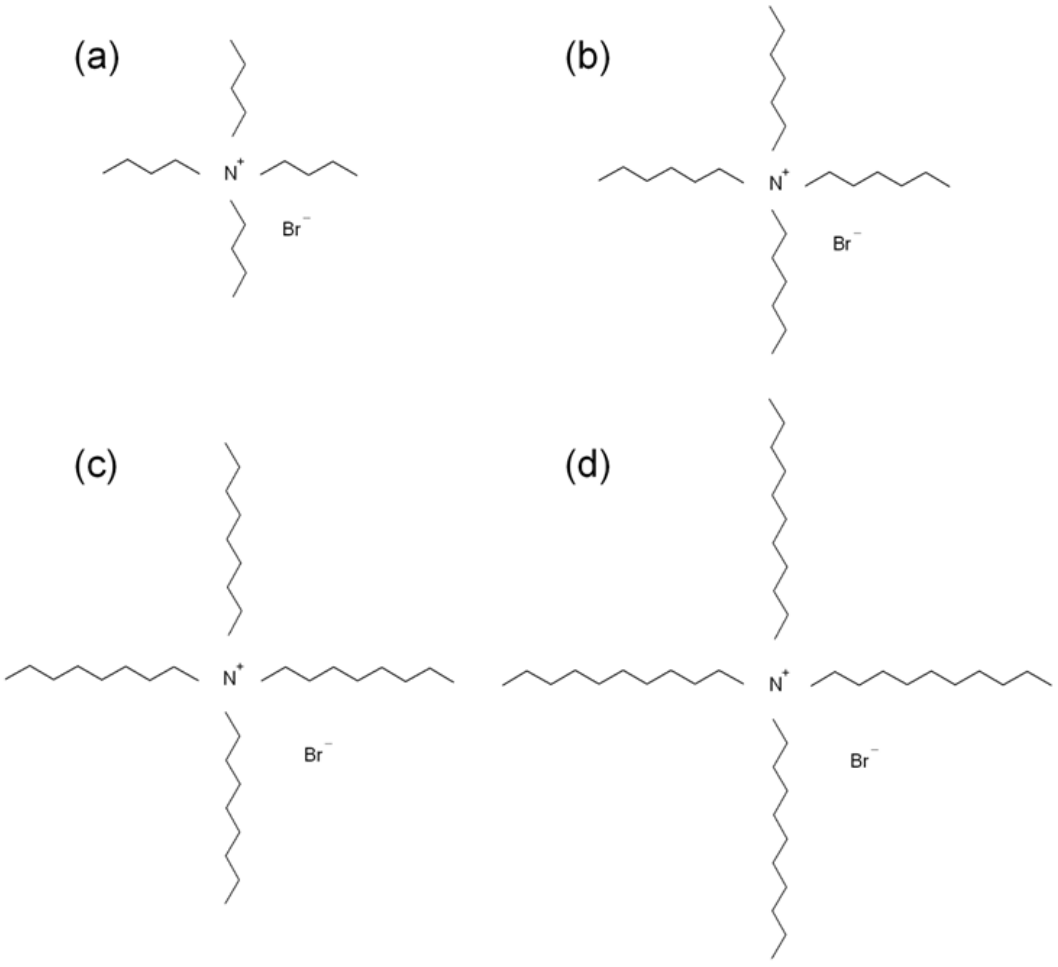


Figure 2-2: Chemical structures of the surfactants used in this study, (a) TBAB, (b) THAB, (c) TOAB, (d) TKAB

TEM imaging of Ge NCs synthesised in the presence of TBAB as the surfactant template (Figure 2-3(a)) show that the Ge NCs are highly size and shape monodisperse, with no evidence of aggregation. Inset in Figure 2-3(a) is a histogram of NC diameters (see section 2.2.2). Fitting the histogram to a Gaussian model

yielded a mean diameter of 3.5 nm, with a standard deviation of 0.4 nm, closely matching the (111) spacing of bulk germanium, emphasising the highly size monodisperse nature of the NCs. Replacing TBAB with THAB, TOAB or TKAB resulted in an increase in the mean NC diameter to 3.7 ± 0.3 nm, 4.1 ± 0.3 nm and 4.5 ± 0.4 nm respectively, see Figure 2-3(b)-(d). These TEM imaging results demonstrate that selection of the appropriate surfactant allows a high degree of control over the average NC diameter while maintaining the size monodispersity of the sample. A strong correlation is observed between the alkyl chain length of the surfactant and the Ge NC size, with an average increase in the NC diameter from 3.5 to 4.5 nm as the surfactant side chains are increased from C_4 to C_{10}.

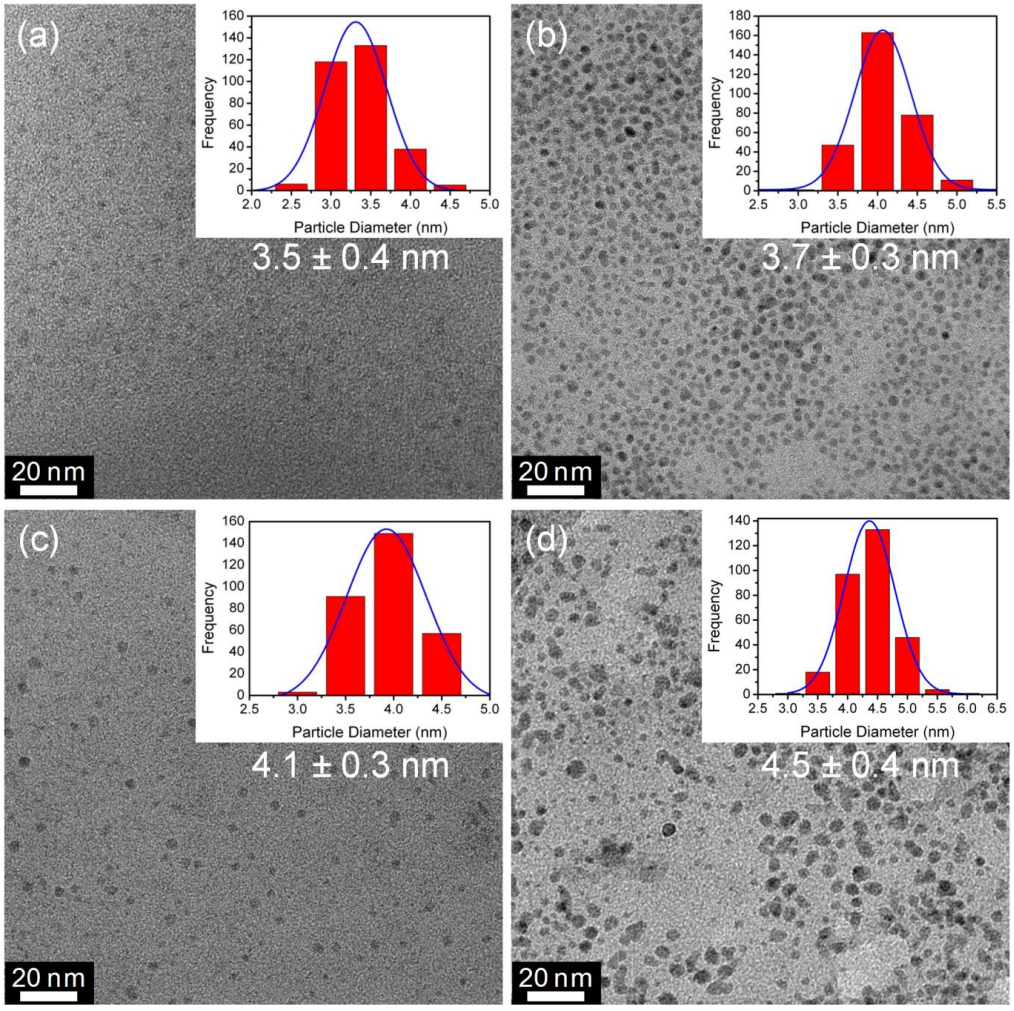


Figure 2-3: TEM images of Ge NCs synthesised using the surfactants (a) TBAB, (b) THAB, (c) TOAB and (d) TKAB. Inset: Size histograms of Ge NCs with Gaussian curves fitted to the data

HR-TEM imaging was used in conjunction with SAED to confirm the crystallinity and establish the crystal phase of the NCs; see Figure 2-4(a) and (b). HR-TEM imaging (Figure 2-4(a)) showed that the Ge NCs form a single contiguous crystalline phase, without the presence of packing defects. The lattice fringes shown in Figure 2-4(a) correspond to a *d* spacing of 2.0 Å, matching the (220) spacing reported for the germanium unit cell. SAED patterns of the Ge NCs (Figure 2-4(b)) showed reflections that could be indexed to Ge diamond cubic (*Fd3m*) lattice at 2.0 Å (220), 1.7 Å (311), 1.3 Å (331) and 1.2 Å (422), respectively.

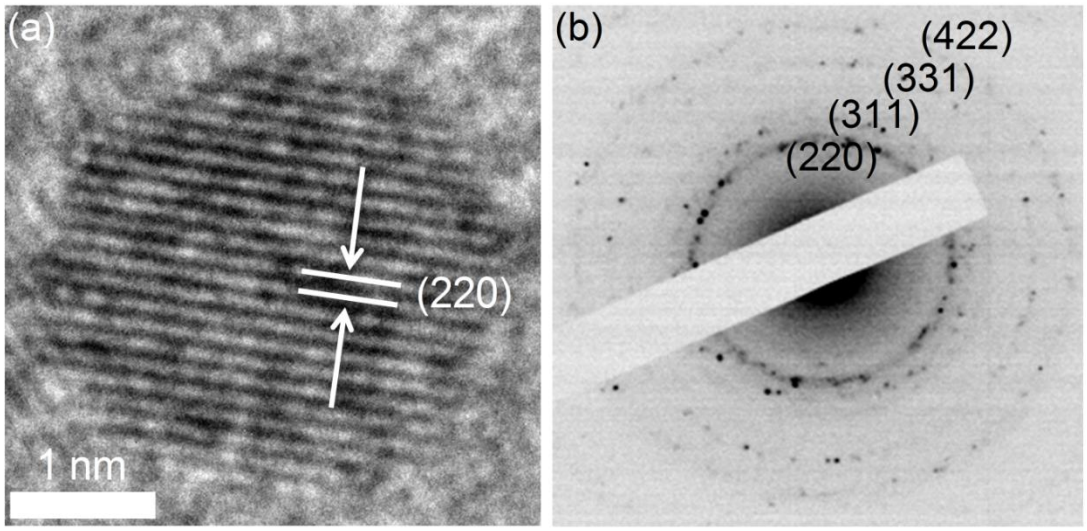


Figure 2-4: (a) HR-TEM image of an individual Ge NC. (b) SAED pattern of as-synthesised Ge NCs, with the reflections characteristic of crystalline Ge indexed

The surface chemistry of the quantum dots was characterised by FTIR, see Figure 2-5. The peaks at 3690 and 3605 cm^{-1} are assigned to the N-H stretching of the amine, while the band at 1602 cm^{-1} is attributed to the N-H scissoring mode.[5] The features observed between 3000-2850 cm^{-1} are attributed to C-H stretching modes.[6] The peaks observed at 1458 and 1260 cm^{-1} are attributed to scissoring and symmetric bending of the Ge-C bond, respectively. The strong peak at 1098 cm^{-1} is assigned to the C-N stretching mode of the amine group.[7] The absence of the characteristic $CH=CH_2$ peaks at 900, 1640 and 3080 cm^{-1}, combined with the formation of the Ge-C bond at 1458 and 1260 cm^{-1}, indicate covalent attachment of the amine ligand to the NC surface. The absence of peaks between 1000-800 cm^{-1}, previously reported

for Ge-O stretching vibrations,[8-10] indicates that the germanium nanocrystals are well passivated with minimal surface oxidation.

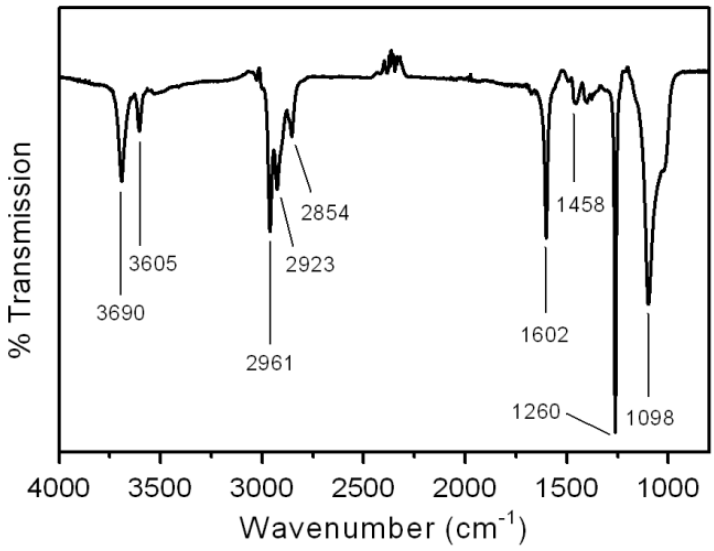


Figure 2-5: FTIR spectrum of the amine-terminated Ge NCs

Figure 2-6(a) shows the UV-Vis absorption spectra of the Ge NCs prepared using the different surfactants. The spectra are very similar, with a strong absorbance in the UV and a tail extending into the visible region, in agreement with previous reports for amine-capped semiconductor nanocrystals.[1]

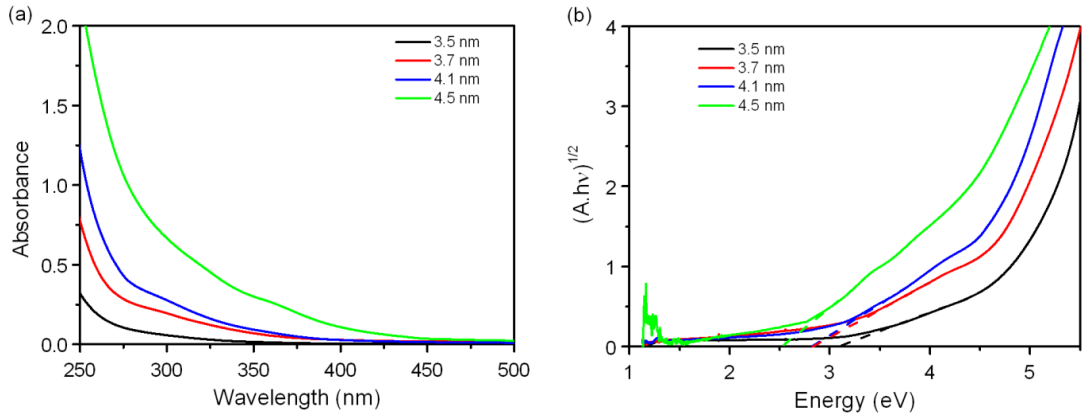


Figure 2-6: (a) UV-Vis absorption spectra for the different sized NCs. (b) Tauc plotting of the UV-Vis data shows a decrease in the bandgap with increasing size

While the spectrum of the 3.5 nm NCs is almost featureless, an additional shoulder near 300 nm is observed in the spectra of the 3.7 and 4.1 nm Ge NCs. Increasing the NC diameter to 4.5 nm results in a significant red-shift in the overall spectrum[1, 11, 12]

and the emergence of an additional peak centred near 360 nm. Tauc plots of the absorption data showed strong quantum confinement effects within the NCs, with an onset of absorption between 3.1 and 2.8 eV for Ge NCs between 3.5 to 4.1 nm in diameter, while the 4.5 nm NCs had an onset close to 2.5 eV, see Figure 2-6(b).

Figure 2-7(a) shows the normalised PL spectra of aqueous dispersions of the amine-capped Ge nanocrystals prepared using the four surfactants. The 3.5 and 3.7 nm diameter NCs exhibited a strong blue emission centered at *ca.* 460 nm (2.7 eV), with a tail extending into the red region of the spectrum.

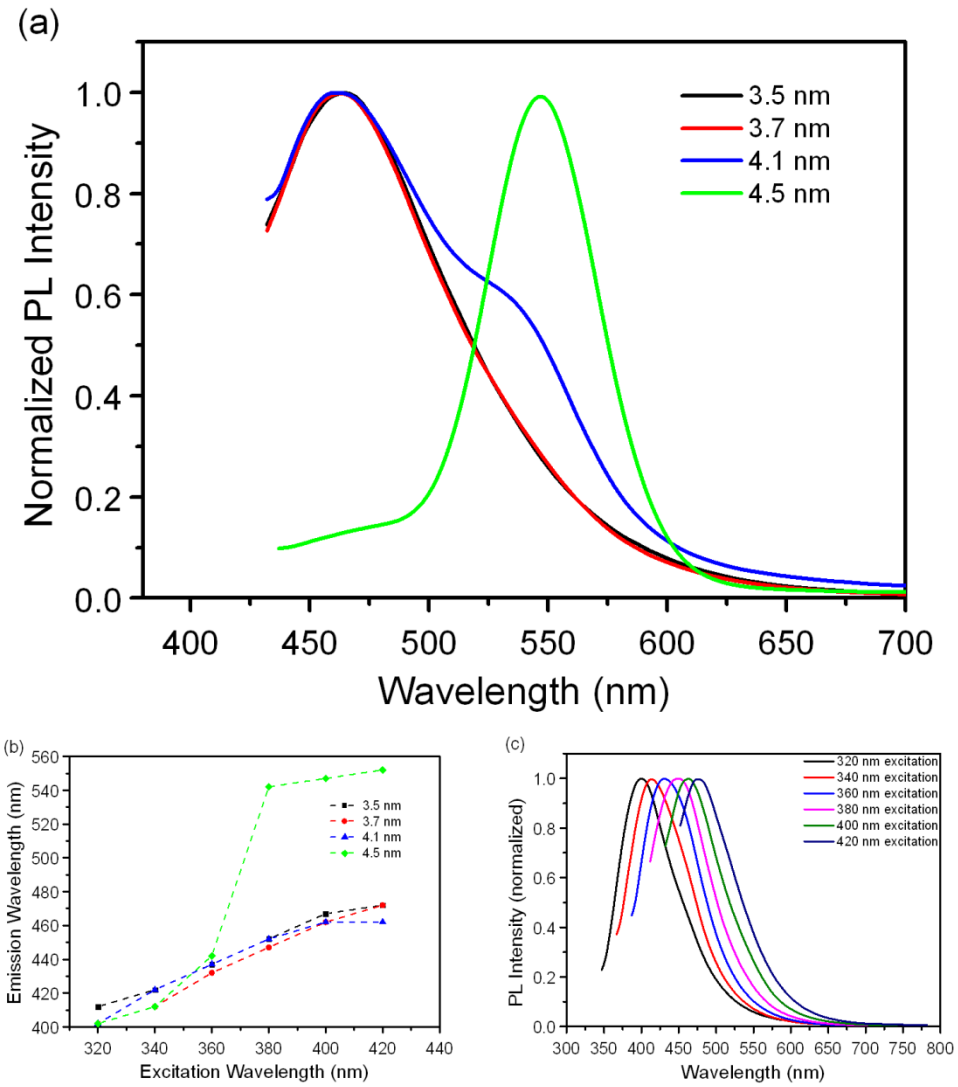


Figure 2-7: (a) PL spectra of aqueous dispersions of Ge NCs recorded using an excitation wavelength of 400 nm. (b) Wavelength position of the luminescence maximum as a function of excitation wavelength. (c) Representative red shift of the maximum emission wavelength with increasing excitation wavelength

Increasing the NC diameter to 4.1 nm was accompanied by the emergence of a shoulder in the PL spectrum at *ca.* 540 nm (2.3 eV). Further increasing the NC diameter to 4.5 nm resulted in a marked transition from blue to green emission, with complete suppression of the peak centered at 460 nm, and the emergence of a new peak centered at *ca.* 545 nm with a very narrow full width at half maximum (FWHM) of 50 nm, in agreement with reports for highly size monodisperse green luminescent Ge NCs.[13]

All the NC dispersions show a strong dependence between the wavelength position of the PL maximum and the excitation wavelength, see Figure 2-7(b) and (c). For the three smaller Ge NCs, increasing the excitation wavelength from 320 to 420 nm results in a *ca.* 60 nm red shift in the position of the PL maximum. In contrast to this, the largest Ge NCs (4.5 nm) exhibited a marked transition (*ca.* 100 nm) from primarily blue to green emission at excitation wavelengths above 360 nm.

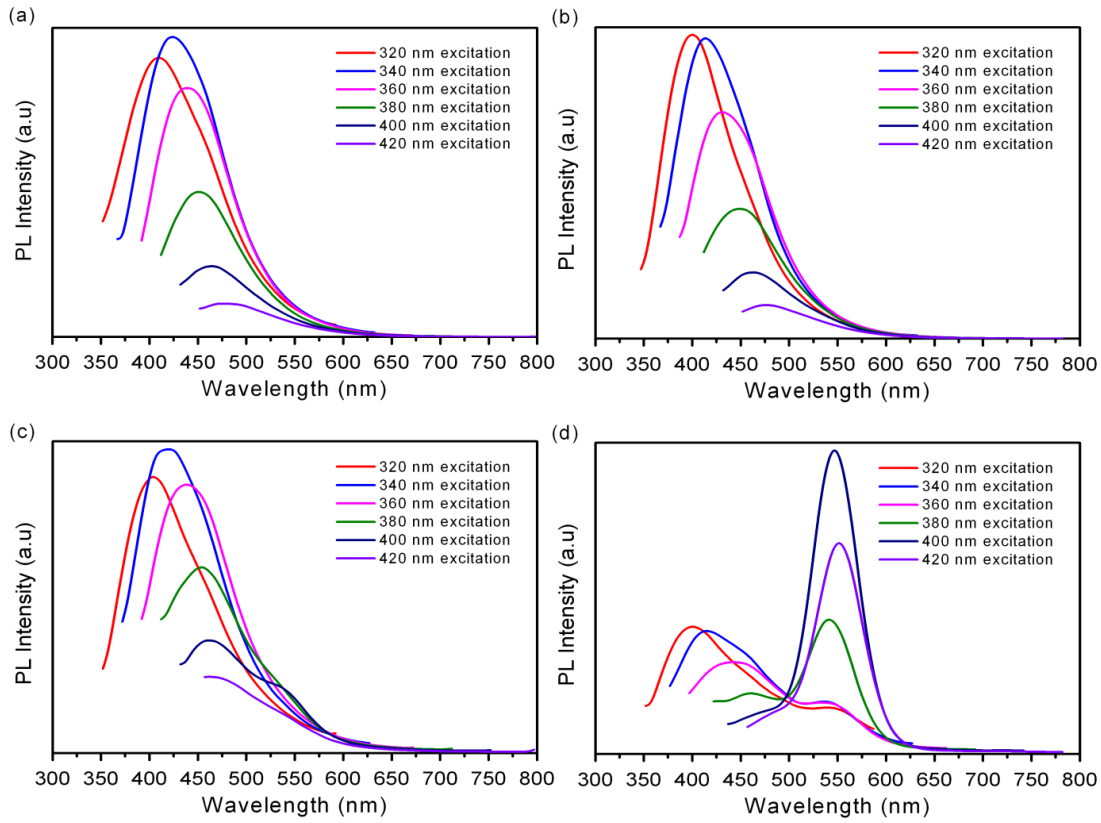


Figure 2-8: Normalised PL spectra of aqueous dispersions of Ge NCs recorded using different excitation wavelengths for (a) 3.5 nm, (b) 3.7nm, (c) 4.1 nm and (d) 4.5 nm nanocrystals

The maximum PL intensity for 3.5 to 4.1 nm NCs was observed for 340 nm excitation (3.65 eV), significantly exceeding the energy of the absorption edge (3.1 eV), see Figure 2-6. A decrease in the relative PL intensity is observed at increasing excitation wavelengths (see Figure 2-8(a) and (b)), in agreement with previous reports.[14-20] 4.1 nm Ge NCs exhibited similar trends in their photophysical response, with the emergence of an additional shoulder at excitation wavelengths at or above 400 nm, see Figure 2-8(c). The 4.5 nm Ge NCs showed a similar wavelength dependence from 320 to 360 nm for blue emission, with an significantly more intense green emission observed at excitation wavelengths from 380 to 420 nm, see Figure 2-8(d).

This wavelength dependence has previously been attributed to sample polydispersity, with the smaller NCs being selectively excited at shorter wavelengths, and larger NCs at longer wavelengths. However, the narrow size distributions in the Ge NCs reported here preclude this argument, while the transition from blue to green emission with increasing NC diameter indicate that quantum confinement effects play a significant role.

The microscopic origin of the blue-green luminescence observed in organically terminated Group IV nanocrystals remains unresolved. The wide variety of synthetic strategies reported, together with broad particle size distributions, different ligand passivation strategies and varying degrees of surface oxidation have all contributed to the lack of consensus.[1, 17, 21-24] The underlying mechanism is usually described in terms of quantum size effects where the electron-hole pairs are well confined within the nanocrystal core, a surface chemistry model that emphasises the importance of species at the nanocrystal surface, or a combination of both. The marked size dependency observed in the UV-Vis absorption spectra shown in Figure 2-6 agrees well with the quantum confinement model.

PLE spectra of the Ge NCs recorded at their PL maxima are shown in Figure 2-9. The three smaller Ge NCs exhibit similar spectra, with two distinct peaks observed at *ca.* 260 and 340 nm, which are most likely due to direct *Γ*-*Γ* band gap transitions.[20]

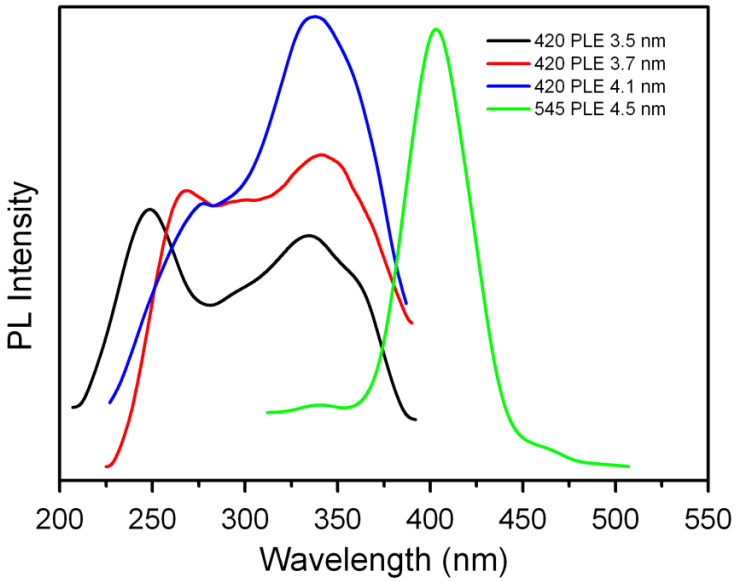


Figure 2-9: Normalised photoluminescence excitation (PLE) spectra of aqueous dispersions of Ge nanocrystals. The wavelength positions at which the spectra were recorded are indicated

In contrast, the PLE spectrum of the 4.5 nm Ge NCs shows a single peak centered at 400 nm, close to the onset of absorption determined from the Tauc plots shown in Figure 2-6, suggesting a lowering of the energies required for exciton generation, consistent with quantum confinement effects within the Ge nanocrystalline core.

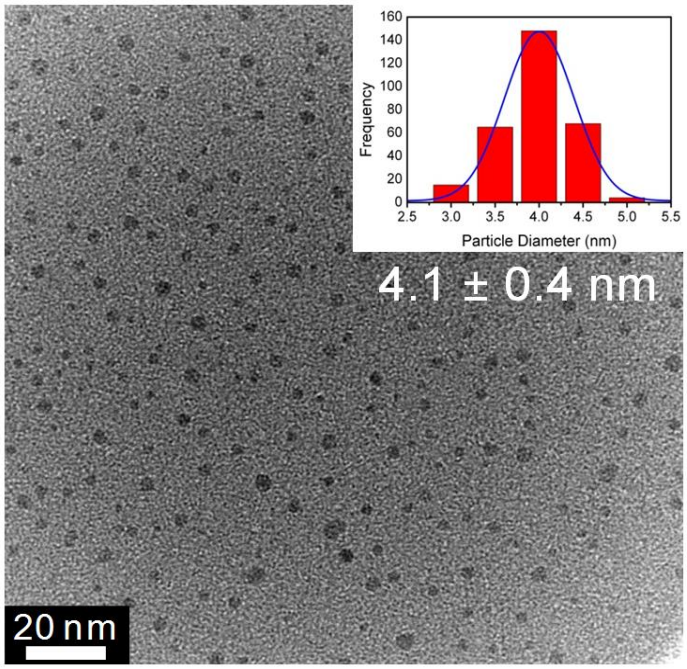


Figure 2-10: TEM image of the NCs produced using TOAB as the surfactant template, re-dispersed in chloroform

Dispersal of NCs in polar organic solvents would render them amenable to low cost, solution based device processing methods used in a number of different application areas. Figure 2-10 shows a TEM image of the NCs in chloroform. It is obvious from the image that no agglomeration of the NCs occurred, while the size and monodispersity remained the same.

PL spectra of the Ge NCs dispersed in a variety of polar organic solvents (see Figure 2-11) show broadly similar PL spectra and excitation wavelength dependency.

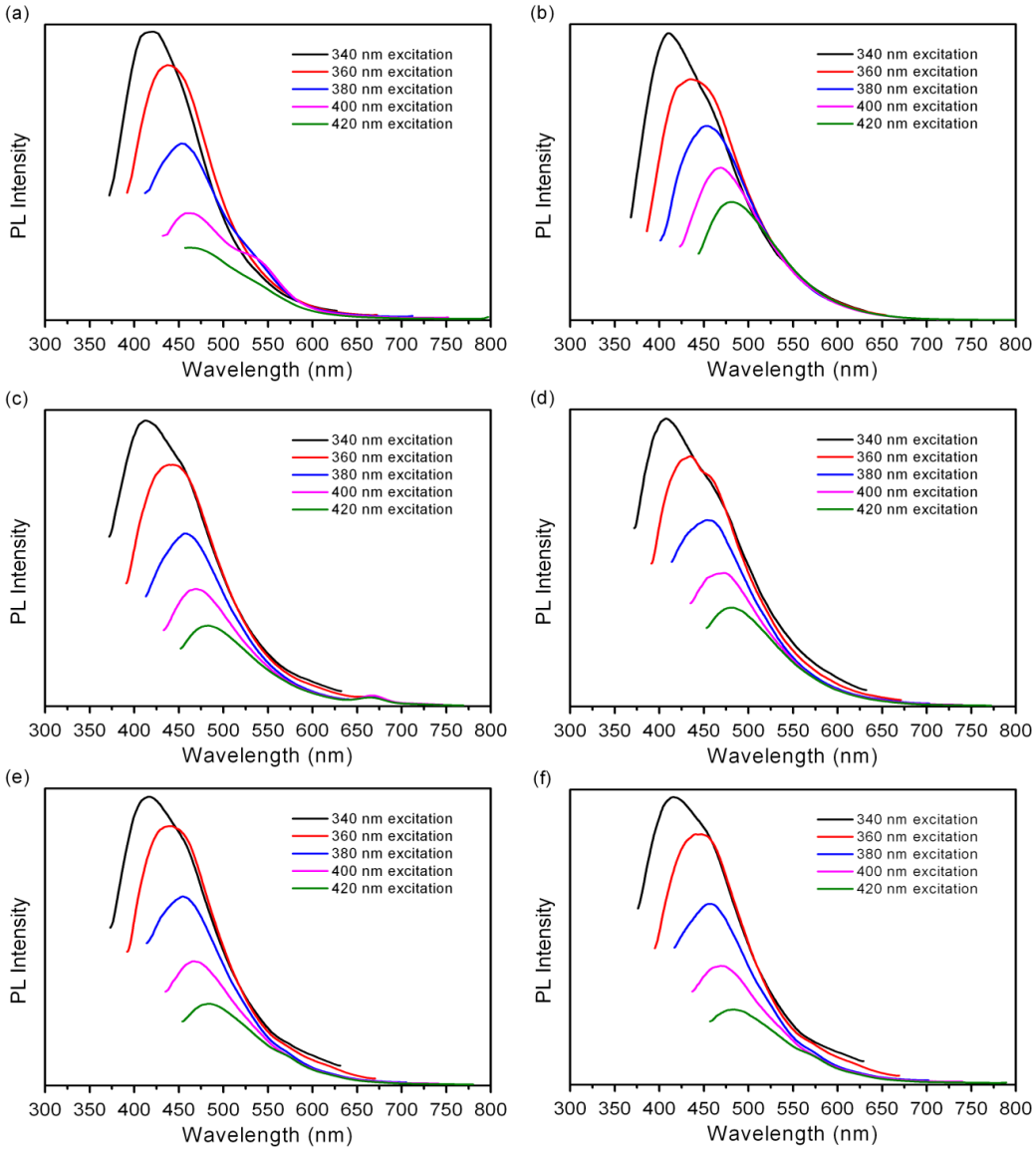


Figure 2-11: Normalised PL spectra of Ge NCs dispersed in (a) water, (b) chloroform, (c) acetonitrile, (d) dichloromethane, (e) ethanol and (f) methanol recorded using different excitation wavelengths

The slight shifting in the position of the PL maxima indicates some involvement of NC surface species. These spectra rule out the involvement of contaminants and most importantly, they highlight the fact that the NCs are proccessible in a range of solvents which is important for future device fabrication and applications.

To test the stability of the NCs (in chloroform), a PL spectrum (400 nm excitation) of a fresh sample was compared to a spectrum taken four months later (See Figure 2-12). The spectra are similar, apart from a slight decrease in intensity of the peak as well as a 2 nm blue shift, but overall this result indicates that the NCs are stable in solution for long periods of time.

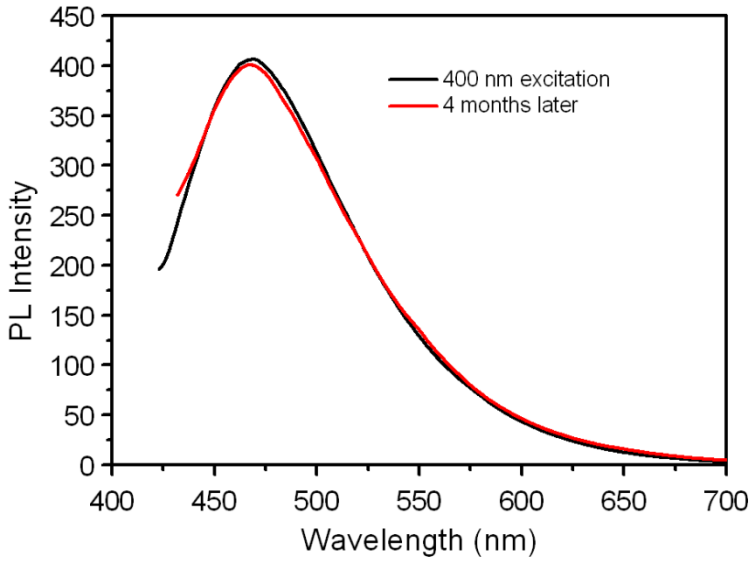


Figure 2-12: Stability test for the Ge NCs

PL QYs were determined using 9,10-diphenylanthracene and fluorescein as reference emitters for blue and green emissive NCs, see Experimental Section for further details. Figure 2-13(a) shows the integrated PL intensity (340 nm excitation) of dilute dispersions of the blue emitting Ge NCs (3.5, 3.7 & 4.1 nm diameter) compared with solutions of 9,10-diphenylanthracene recorded under identical excitation conditions. The QYs of the 3.5 and 3.7 nm Ge NCs were 19 and 20 % respectively, comparable to QY values reported in the literature, which range from 11 to 17 %.[1, 13, 24, 25] The 4.1 nm Ge NCs exhibit a lower QY value of 12 %. Figure 2-13(b) shows the integrated PL intensity (400 nm excitation) of dilute dispersions of

the green emitting 4.5 nm Ge NCs compared with aqueous solutions of fluorescein. The quantum yield of the Ge NCs was found to be 8 % at the optimal excitation wavelength of 400 nm, again in good comparison with the literature.

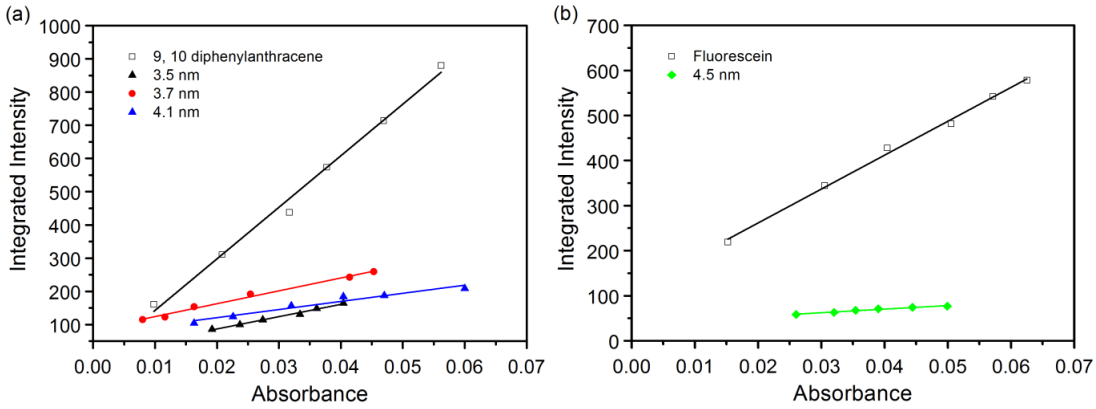


Figure 2-13: (a) Integrated PL intensity *vs*. absorbance for dilute dispersions of blue emitting Ge NCs and 9,10-diphenylanthracene. (b) Integrated PL intensity *vs*. absorbance for dilute dispersions of green emitting Ge NCs and fluorescein

2.3.2 Evidence for a Size Threshold Between Blue and Green Emission

Here, the synthetic conditions were adapted to produce a polydisperse Ge NC sample which is subsequently purified by a combination of column chromatography and centrifugation to give highly emissive nanocrystals with different sizes and emission colours in each fraction produced. Many groups employ post synthetic purification techniques such as high performance liquid chromatography (HPLC),[20] column chromatography,[24] controlled etching,[26] size-selective precipitation using non-solvents,[9, 12, 23, 27-29] or a combination of the above[19, 25] to chemically purify and separate size monodisperse Ge NCs fractions. While chromatography and HPLC methods work well for size separation, the method is generally reported only for small samples, and the rate of production is slow compared to simple centrifugation methods.

To obtain a polydisperse sample, a longer chained surfactant was used, namely tetrahexadecylammonium bromide (THDAB), see Table 2-1, entry 5 for reaction conditions.

Figure 2-14(a) shows a TEM image of amine-terminated Ge NCs prepared by the reduction of $GeCl_4$ by $LiAlH_4$ in the presence of THDAB, see the Experimental Section for further details. As can be seen from this image, the as-synthesised Ge NCs are relatively polydisperse, with average sizes ranging from 3-12 nm, and evidence of some shape anisotropy in the sample. Fitting the histogram to a lognormal model yielded a mean diameter of 6.4 nm, with a standard deviation of 2.0 nm. Following centrifugation at 13,200 rpm for 15 minutes, the supernatant was decanted off and the resultant pellet re-dispersed in deionised water. TEM imaging of the supernatant, Figure 2-14(b), demonstrates that it was possible to separate highly size and shape monodisperse NCs from the parent solution. The corresponding histogram was fitted with a Gaussian model, yielding a mean diameter of 3.9 nm and a standard deviation of 0.4 nm.

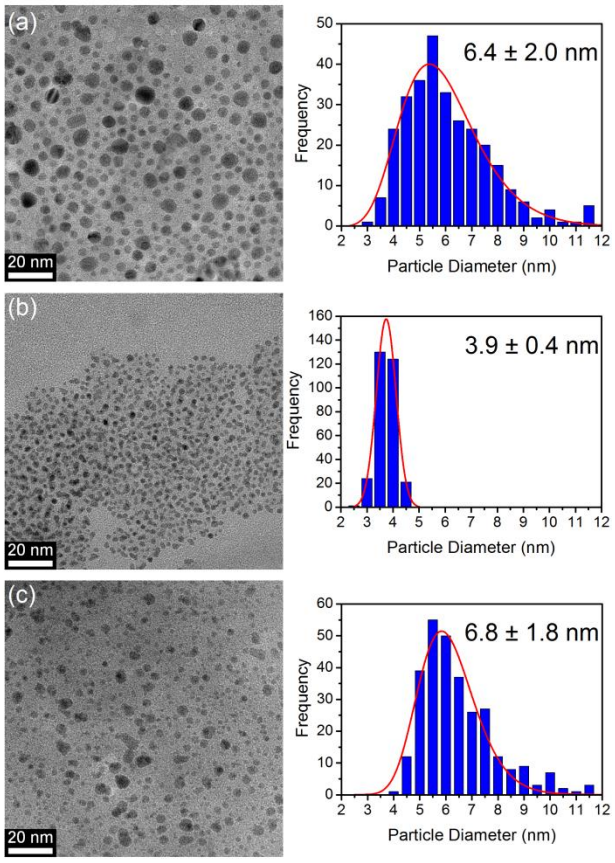


Figure 2-14: Left, TEM images of the (a) parent solution, (b) supernatant and (c) pellet. Right, histograms of the NC size with curves fitted to the data using a lognormal model in the case of (a) and (c) and a Gaussian model in the case of (b)

Figure 2-14(c) shows a TEM image of the Ge NCs from the pellet, with the corresponding histogram fitted with a lognormal model. It is evident that the size of the NCs is larger in the pellet, with an average diameter of 6.8 ± 1.8 nm. These TEM imaging results confirm that this simple centrifugation step results in the separation of a polydisperse parent solution into 2 fractions with differently sized NCs in each fraction.

The optical properties of these Ge NCs were investigated using UV-Vis, PL and PLE spectroscopy. Figure 2-15(a) and (b) show the UV-Vis, PL and PLE spectra for the 3.9 nm and 6.8 nm NCs, respectively. The UV-Vis spectrum for the small NCs (Figure 2-15(a)) shows weak absorption in the UV with a feature at *ca.* 290 nm and an onset of absorption at *ca.* 350 nm. These NCs show strong blue luminescence centred at *ca.* 430 nm, while the PLE spectrum (dashed line) recorded at the PL maximum shows a clear peak at 340 nm.

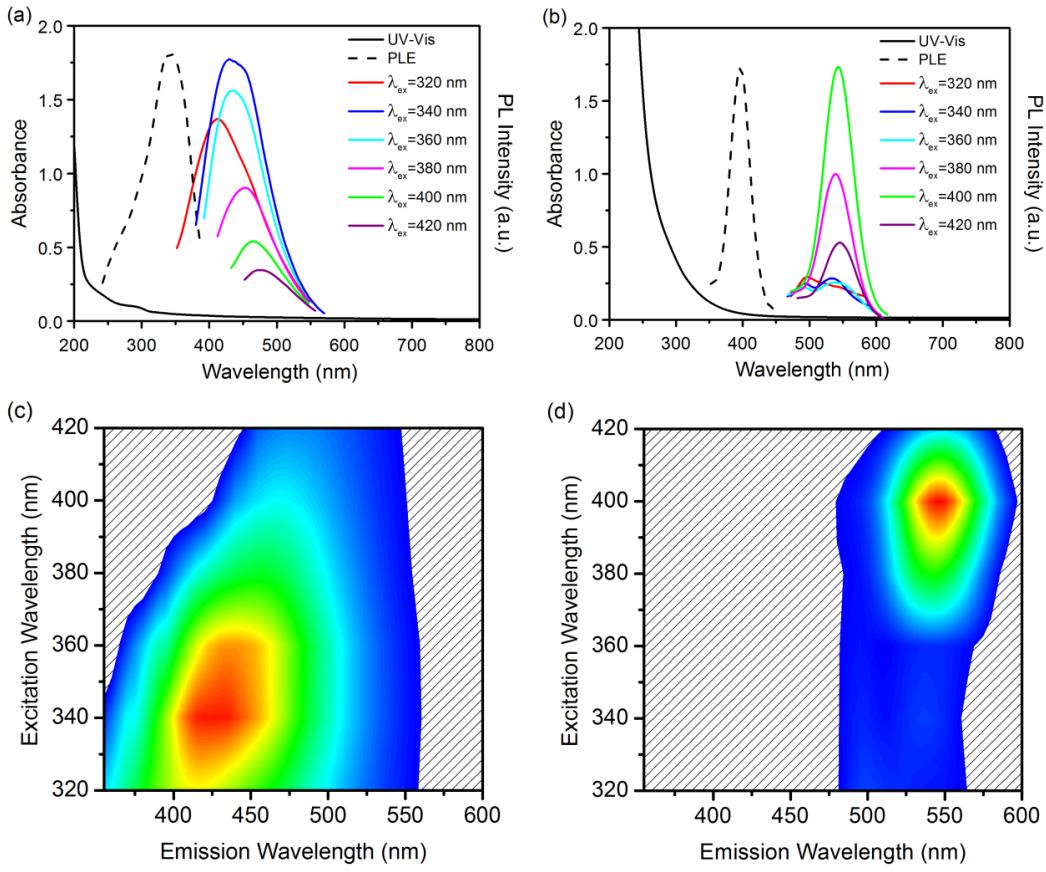


Figure 2-15: (a) UV-Vis, PL and PLE (dashed lines) spectra of (a) 3.9 nm and (b) 6.8 nm Ge NCs. Excitation-emission scanning matrices for (c) 3.9 nm and (d) 6.8 nm Ge NCs

The 6.8 nm NCs show a bathochromic shift in the onset of absorption and a stronger absorbance in the UV (see Figure 2-15(b)), in agreement with the results reported in the previous section. The larger NCs exhibited an intense green emission colour, with a wavelength maximum at *ca.* 540 nm, while the PLE spectrum showed a distinct peak at 400 nm. The PL spectra of both nanocrystal fractions demonstrated the strong excitation wavelength dependence, which is due to the involvement of different surface states in the luminescence process rather than sample polydispersity.

This excitation wavelength dependency for both NC fractions is shown graphically in the photoluminescence excitation-emission matrices presented in Figures 2-15(c) and (d). For 3.9 nm Ge NCs, the strong blue luminescence observed shifts to longer wavelengths and decreases in intensity as the excitation wavelength is increased from 320 nm to 420 nm. In contrast, the intensity of the green photoluminescence increases with increasing excitation wavelength, without any significant shift in emission wavelength. The corresponding photoluminescence excitation-emission matrix for the parent solution shows the two emission bands visible at *ca.* 420 nm and *ca.* 540 nm, corresponding to the presence of both fractions, see Figure 2-16(a). The luminescence intensity of the overlaid PL spectra of the parent solution also reflects the individual excitation wavelength dependencies of both fractions (Figure 2-16(b)).

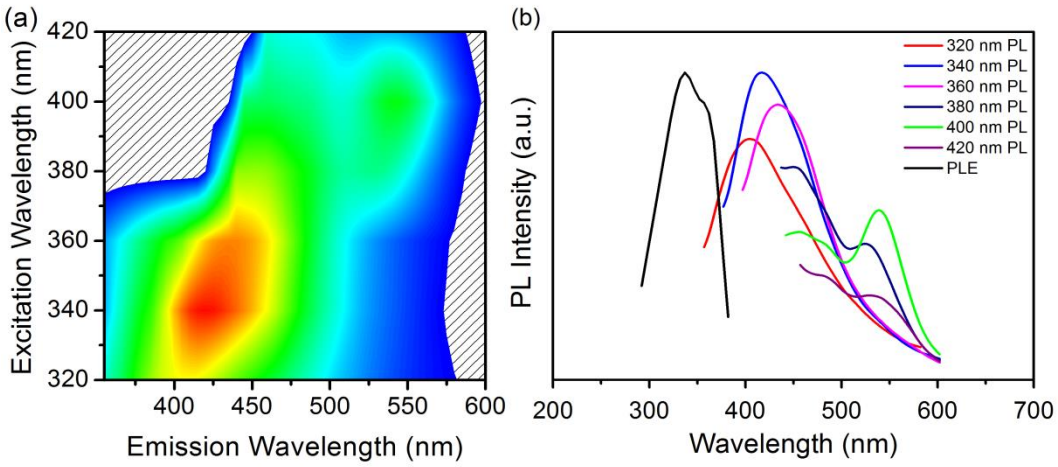


Figure 2-16: (a) Excitation-emission scanning matrix, (b) PL and PLE (black line) spectra of the parent solution

Figure 2-17(a) shows the integrated PL intensity of dilute dispersions of the 3.9 nm Ge NCs compared with solutions of 9,10-diphenylanthracene. The QY of the 3.9 nm NCs was calculated to be 21.5 %. Figure 2-17(b) shows the integrated PL intensity of dilute dispersions of the 6.8 nm Ge NCs compared with aqueous solutions of fluorescein. The QY of the 6.8 nm Ge NCs was found to be 6.2 %; again in good comparison with the literature. PL lifetimes of the Ge NCs were acquired using time-correlated single photon counting methods; see Figure 2-17(c). Measured transients were well fitted (χ^2 < 1.1) to the sum of two weighted exponentials, yielding an average lifetime of 6.1 ns for the 3.9 nm NCs and 7.8 ns for the 6.8 nm NCs, consistent with previous reports. [1, 13, 24, 25]

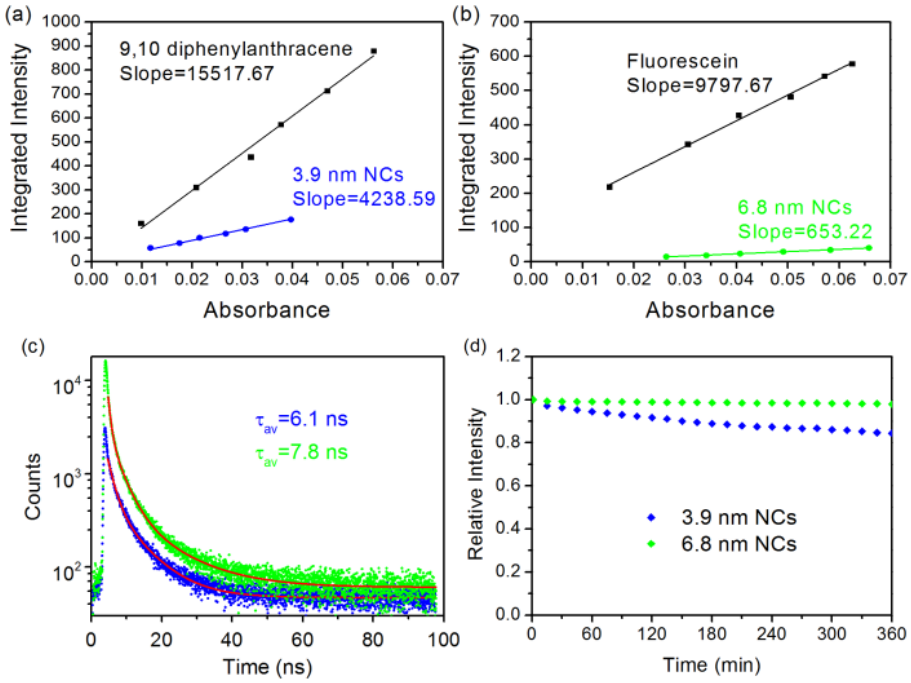


Figure 2-17: Integrated PL intensity *vs.* absorbance for dilute dispersions of (a) 3.9 nm Ge NCs and 9,10 diphenylanthracene, (b) 6.8 nm Ge NCs and fluorescein. (c) PL decays of both NC samples and (d) long-term PL stability of both samples recorded over 6 hours

The nanosecond lifetimes provide further confirmation that the Ge NCs luminescence arises from surface state recombination, as band gap transitions in indirect semiconductors typically occur on microsecond timescales.[30] The difference in PL lifetimes between the NC fractions is attributed to the involvement of different surface states in the luminescence process. It is noted that both Ge NC

fractions exhibit good to excellent long-term PL stability, decreasing by only 15 % for the 3.9 nm NCs and only 2 % for the 6.8 nm NCs over a period of 6 hours, see Figure 2-17(d).

2.4 Conclusion

Despite the successes of the microemulsion synthesis approach for preparation of high quality, size monodisperse Ge NCs, the effect of the surfactant structure in determining the size and shape the resultant Ge NCs has not been reported. Here, we report a simple room-temperature synthesis of amine-terminated Ge NCs within inverse micelles. Regulation of the Ge NCs size was achieved by variation of the cationic quaternary ammonium salts used to form the inverse micelles. HR-TEM and SAED showed that the NCs were size monodisperse, highly crystalline, with well-defined core diameters that may be tuned from 3.5 to 4.5 nm. FTIR spectroscopy confirmed that the ligand successfully attached to the surface of the NCs with minimal oxidation. These water-dispersed Ge NCs exhibited interesting optical properties with a red shift in the onset of absorption with increasing NC size, a narrow luminescence with a marked transition from primarily blue to green emission as the NC diameter increases from 3.7 nm to 4.5 nm. [a] They also displayed the property of excitation tuneable emission. It was shown that the NCs could be dispersed in a range of solvents and that they are stable in solution for long periods of time. Quantum yields were calculated to be up to 21.5 %. A polydisperse sample with a mixed blue/green emission profile could be separated by centrifugation into individual sized NCs which each showed blue and green only, with total suppression of other emission colours.[b]

[a] Publications arising from this work: "Size and Emission Color Tuning in the Solution Phase Synthesis of Highly Luminescent Germanium Nanocrystals" *J. Mater. Chem. C, 2014, 2 (18), 3562 - 3568*

[b] Publications arising from this work: "Germanium Nanocrystals as Luminescent Probes for Rapid, Sensitive and Label-Free Detection of Fe^{3+} Ions" *Nanoscale, 2015, 7 (12), 5488 - 5494*

2.5 References

1. Warner, J. H.; Tilley, R. D., Synthesis of Water-Soluble Photoluminescent Germanium Nanocrystals. *Nanotechnology* **2006,** *17*, 3745.

2. Wilcoxon, J. P.; Provencio, P. P.; Samara, G. A., Synthesis and Optical Properties of Colloidal Germanium Nanocrystals. *Phys. Rev. B* **2007,** *76*, 199904.

3. Williams, A. T. R.; Winfield, S. A.; Miller, J. N., Relative Fluorescence Quantum Yields Using a Computer-Controlled Luminescence Spectrometer. *Analyst* **1983,** *108*, 1067.

4. Lakowicz, J. R., *Principles of Fluorescence Spectroscopy*. Springer-Verlag: New York, 2008.

5. Ahire, J. H.; Wang, Q.; Coxon, P. R.; Malhotra, G.; Brydson, R.; Chen, R.; Chao, Y., Highly Luminescent and Nontoxic Amine-Capped Nanoparticles from Porous Silicon: Synthesis and Their Use in Biomedical Imaging. *ACS Appl. Mater. Interfaces* **2012,** *4*, 3285.

6. Silverstein, R. M.; Bassler, G. C.; Morrill, T. C., *Spectrometric Identification of Organic Compounds*. Wiley: New York, 1991.

7. Socrates, G., *Infrared Characteristic Group Frequencies*. Wiley: Chichester, 1980.

8. Henderson, E. J.; Seino, M.; Puzzo, D. P.; Ozin, G. A., Colloidally Stable Germanium Nanocrystals for Photonic Applications. *ACS Nano* **2010,** *4*, 7683.

9. Lee, D. C.; Pietryga, J. M.; Robel, I.; Werder, D. J.; Schaller, R. D.; Klimov, V. I., Colloidal Synthesis of Infrared-Emitting Germanium Nanocrystals. *J. Am. Chem. Soc.* **2009,** *131*, 3436.

10. Gerung, H.; Bunge, S. D.; Boyle, T. J.; Brinker, C. J.; Han, S. M., Anhydrous Solution Synthesis of Germanium Nanocrystals from the Germanium(II) Precursor $Ge[N(SiMe_3)_2]_2$. *Chem. Commun.* **2005,** 1914.

11. Holman, Z. C.; Kortshagen, U. R., Absolute Absorption Cross Sections of Ligand-Free Colloidal Germanium Nanocrystals. *Appl. Phys. Lett.* **2012,** *100*, 133108.

12. Vaughn, D. D., II; Bondi, J. F.; Schaak, R. E., Colloidal Synthesis of Air-Stable Crystalline Germanium Nanoparticles with Tunable Sizes and Shapes. *Chem. Mater.* **2010,** *22*, 6103.

13. Ghosh, B.; Sakka, Y.; Shirahata, N., Efficient Green-Luminescent Germanium Nanocrystals. *J. Mater. Chem. A* **2013,** *1*, 3747.

14. Ma, X.; Wu, F.; Kauzlarich, S. M., Alkyl-Terminated Crystalline Ge Nanoparticles Prepared from NaGe: Synthesis, Functionalization and Optical Properties. *J. Solid. State. Chem.* **2008,** *181*, 1628.

15. Tanke, R. S.; Kauzlarich, S. M.; Patten, T. E.; Pettigrew, K. A.; Murphy, D. L.; Thompson, M. E.; Lee, H. W. H., Synthesis of Germanium Nanoclusters with Irreversibly Attached Functional Groups: Acetals, Alcohols, Esters, and Polymers. *Chem. Mater.* **2003,** *15*, 1682.

16. Taylor, B. R.; Fox, G. A.; Hope-Weeks, L. J.; Maxwell, R. S.; Kauzlarich, S. M.; Lee, H. W. H., Solution Preparation of Ge Nanoparticles with Chemically Tailored Surfaces. *Mater. Sci. Eng., B* **2002,** *96*, 90.

17. Taylor, B. R.; Kauzlarich, S. M.; Delgado, G. R.; Lee, H. W. H., Solution Synthesis and Characterization of Quantum Confined Ge Nanoparticles. *Chem. Mater.* **1999,** *11*, 2493.

18. Taylor, B. R.; Kauzlarich, S. M.; Lee, H. W. H.; Delgado, G. R., Solution Synthesis of Germanium Nanocrystals Demonstrating Quantum Confinement. *Chem. Mater.* **1998,** *10*, 22.

19. Shirahata, N., Solution-Processable White-Light-Emitting Germanium Nanocrystals. *J. Solid. State. Chem.* **2014,** *214*, 74.

20. Wilcoxon, J. P.; Provencio, P. P.; Samara, G. A., Synthesis and Optical Properties of Colloidal Germanium Nanocrystals. *Phys. Rev. B* **2001,** *64*, 035417.

21. Vaughn II, D. D.; Schaak, R. E., Synthesis, Properties and Applications of Colloidal Germanium and Germanium-Based Nanomaterials. *Chem. Soc. Rev.* **2013,** *42*, 2861.

22. Muthuswamy, E.; Iskandar, A. S.; Amador, M. M.; Kauzlarich, S. M., Facile Synthesis of Germanium Nanoparticles with Size Control: Microwave Versus Conventional Heating. *Chem. Mater.* **2012,** *25*, 1416.

23. Fok, E.; Shih, M. L.; Meldrum, A.; Veinot, J. G. C., Preparation of Alkyl-Surface Functionalized Germanium Quantum Dots *Via* Thermally Initiated Hydrogermylation. *Chem. Commun.* **2004,** 386.

24. Prabakar, S.; Shiohara, A.; Hanada, S.; Fujioka, K.; Yamamoto, K.; Tilley, R. D., Size Controlled Synthesis of Germanium Nanocrystals by Hydride Reducing Agents and Their Biological Applications. *Chem. Mater.* **2010,** *22*, 482.

25. Shirahata, N.; Hirakawa, D.; Masuda, Y.; Sakka, Y., Size-Dependent Color Tuning of Efficiently Luminescent Germanium Nanoparticles. *Langmuir* **2012,** *29*, 7401.

26. Kim, S.; Walker, B.; Park, S. Y.; Choi, H.; Ko, S.-J.; Jeong, J.; Yun, M. H.; Lee, J. C.; Kim, D. S.; Kim, J. Y., Size Tailoring of Aqueous Germanium Nanoparticle Dispersions. *Nanoscale* **2014,** *6*, 10156.

27. Codoluto, S. C.; Baumgardner, W. J.; Hanrath, T., Fundamental Aspects of Nucleation and Growth in the Solution-Phase Synthesis of Germanium Nanocrystals. *CrystEngComm* **2010,** *12*, 2903.

28. Ruddy, D. A.; Johnson, J. C.; Smith, E. R.; Neale, N. R., Size and Bandgap Control in the Solution-Phase Synthesis of Near-Infrared-Emitting Germanium Nanocrystals. *ACS Nano* **2010,** *4*, 7459.

29. Lu, X. M.; Korgel, B. A.; Johnston, K. P., High Yield of Germanium Nanocrystals Synthesized from Germanium Diiodide in Solution. *Chem. Mater.* **2005,** *17*, 6479.

30. Dasog, M.; Yang, Z.; Regli, S.; Atkins, T. M.; Faramus, A.; Singh, M. P.; Muthuswamy, E.; Kauzlarich, S. M.; Tilley, R. D.; Veinot, J. G. C., Chemical Insight into the Origin of Red and Blue Photoluminescence Arising from Freestanding Silicon Nanocrystals. *ACS Nano* **2013,** *7*, 2676.

Chapter 3: Synthesis & Characterisation of Surface Modified Germanium Nanocrystals

3.1 Introduction

While the synthetic approach reported in the previous chapter is good for the preparation of high quality, size monodisperse Ge NCs, the post synthetic purification remains lengthy and the Pt catalyst used is toxic to cells.[1] To address these issues, we have developed an efficient one-step synthesis of Ge NCs with *in situ* passivation and straightforward purification steps. Ge NCs are formed by co-reduction of a mixture of $GeCl_4$ and *n*-butyltrichlorogermane; the latter is used both as a capping ligand and a germanium source, see Scheme 3-1. When *n*-butyllithium is added, the Ge-Cl bonds in both precursors are readily reduced, while the more stable Ge-C bond in *n*-butyltrichlorogermane remains, resulting in an alkyl capped surface and ultimately limiting NC growth. This surface-bound layer of butyl chains both chemically passivates the NC surface and stabilises the Ge NCs to facilitate dispersal in a range of organic solvents. The advantage of this synthetic approach over that reported in the previous chapter is that it allows rapid synthesis and functionalisation of NCs with minimal post-synthetic purification requirements. Optical spectroscopy of the NCs showed a strong absorbance in the UV region and an excitation wavelength dependent photoluminescence in the UV/violet range. Lifetime measurements showed the presence of nanosecond components, consistent with recombination of excitons at energy states present at the nanocrystal surface, while PL QYs were determined to be 37 %, one of the highest values reported for organically terminated Ge.

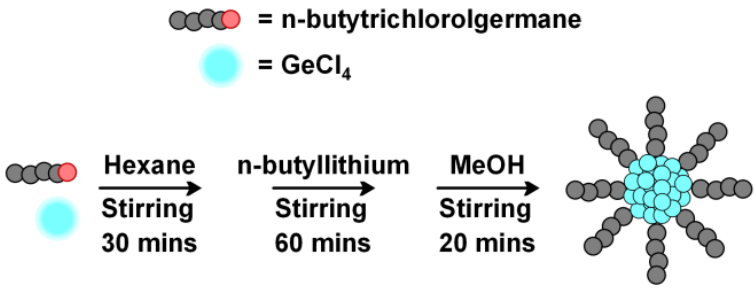
While the alkyl terminated Ge NCs possess excellent stability against aggregation, their emission is mainly confined to the UV/violet spectral region and the insulating surface alkyl layer is considered detrimental for the construction of a NC-based devices. For a variety of potential application areas, it is preferable that the NCs emit in the visible region. Although the photophysical properties of Group IV nanocrystals may be tuned *via* size control, it is known that the emission from organically terminated NCs is highly sensitive to the chemical identity of the surface passivation layer. As a result, a synthetic method was developed to produce size monodisperse Ge NCs with modified surface chemistries bearing carboxylic acid, acetate, amine and epoxy functional groups. Direct comparison of the emission

properties of the surface modified Ge NCs showed the wavelength position of the PL maxima could be moved over 100 nm from the UV to the blue/green, with a tail extending into the yellow/red.

3.2 Experimental Section

3.2.1 Synthesis and Purification of Alkyl Terminated Ge NCs

The synthetic procedure used here is similar to that described in Chapter 2. Ge NCs are formed by co-reduction of $GeCl_4$ in the presence of *n*-butyltrichlorogermane, producing NCs with butyl terminated surfaces (See Scheme 3-1 and Table 3-1, entries 1-3).



Scheme 3-1: Schematic of the one-pot method used to produce butyl terminated Ge NCs by co-reduction of $GeCl_4$ and *n*-butyltrichlorogermane with *n*-butyllithium

Chemicals. Sulphuric acid (95-97 %) and hydrogen peroxide (30 % v/v) were purchased from Sigma Aldrich Ltd. and stored in an ambient atmosphere. $GeCl_4$ (99.99 %), *n*-butyllithium (2.5M in hexanes), hexane (95 %, anhydrous) and methanol (99.8 %, anhydrous) were purchased from Sigma Aldrich Ltd. and stored under inert atmosphere before use. *N*-butyltrichlorogermane was purchased from Fluorochem Ltd. and stored under inert atmosphere before use. All materials and solvents were used as received.

Synthesis and Purification. Glassware used was cleaned by soaking in a base bath overnight, followed by immersion in piranha solution. All synthetic manipulations were carried out in an inert atmosphere glove box. For Ge NCs prepared with both precursors, (see Scheme 3-1) *n*-butyltrichlorogermane (142.7 µL) was added to hexane (60 mL), closely followed by $GeCl_4$ (100 µL) (1:1 ratio of precursors); for Ge NCs prepared with only one precursor, the same quantities

(142.7 µL *n*-butyltrichlorogermane or 100 µL $GeCl_4$ in 60 mL hexane) were used. In all cases, the reaction mixture was stirred continuously for 30 minutes, followed by the drop wise addition of *n*-butyllithium (2 mL), which simultaneously reduces both germanium precursors to form *n*-butyl terminated Ge NCs. *Caution: germane gas could be evolved at this stage of the reaction and care should be taken to prevent exposure to air*.[2] The solution was then left to stir for 1 h. The excess reducing agent was then quenched with the addition of methanol (40 mL) and left to stir for another 20 minutes, after which the reaction was stopped. The solution was then removed from the glove box and the organic solvent removed by rotary evaporation. The Ge NCs were then extracted into 20 mL of chloroform and sonicated for 10 min. The solution was first filtered using filter paper and filtered through PVDF membrane filters (Acrodisc, 0.2 µM). The Ge NCs were further purified by washing once with 20 mL deionised water (18.2 MΩ cm). Butyl-terminated Ge NCs remain in the chloroform phase.

3.2.2 Synthesis and Purification of Functionalised Ge NCs

Chemicals. Dodecyltrimethylammonium bromide (DTAB) (≥ 98 %) was purchased from Sigma Aldrich Ltd. and stored under ambient atmosphere. Germanium tetrachloride (99.99 %), chloroplatinic acid (≥ 99.9 %), lithium aluminium hydride (1M in THF), 1-heptene (≥ 99 %), allylamine (≥ 99 %), allyl alcohol (≥ 99 %), 4-pentenoic acid (97 %), allyl acetate (99 %) 1,2-epoxy-5-hexene (97 %) toluene (99.8 %, anhydrous), methanol (99.8 %, anhydrous) and propan-2-ol (99.5 %, anhydrous) were purchased from Sigma Aldrich Ltd. and stored under inert atmosphere before use. All materials and solvents were used as received.

Synthesis and Purification. The synthetic procedure employed here is similar to those previously described in Section 2.2.1. Briefly, 2.7 g of the surfactant DTAB (2:1 surfactant:precursor ratio) was dissolved in 100 mL toluene in a 2-neck round bottomed flask with continuous stirring. 0.5 mL (4.38 mmol) $GeCl_4$ was then added to the solution and left to stir for 30 min. Ge NCs were formed by the drop wise addition of 6 mL of $LiAlH_4$. The solution was then left to stir for 1 h. The excess reducing agent was then quenched with the addition of 60 mL methanol. The reaction mixture was then split into equal parts to allow the attachment of various

different ligands to NCs of the same size. (See Table 3-1, entries 4-8 for synthetic details)

Chemically passivated nanocrystals were formed by the addition of 0.3 mL of 0.1 M chloroplatinic acid in propan-2-ol as a catalyst, followed by a six times excess of ligand (26.6 mmol). After stirring for 1 h, the Ge NCs were removed from the glove box and the organic solvent removed by rotary evaporation. The resulting brown dry powder was then re-dispersed in 40 mL of chloroform and sonicated for 20 min. The solution was first filtered using filter paper and then PTFE membrane filters (Acrodisc, 0.45 µM) twice to remove the surfactant. Ligand-terminated Ge NCs remain in the chloroform phase.

3.2.3 Characterisation

The structural and optical characterisation reported here, including TEM, SAED, EDX, FTIR, UV-Vis, PL, nanosecond lifetime measurement and QY determination were performed as described in the previous chapter (see Section 2.2.3).

X-Ray Photoelectron Spectroscopy

X-ray photoelectron spectroscopy (XPS) measurements were carried out using a Kratos Ultra DLD photoelectron spectrometer. The narrow scan spectra were obtained under high vacuum conditions by using a monochromatic Al Kα x-ray radiation at 15 kV and 10 mA with an analyser pass energy of 20 eV. Substrates were cleaned for 20 min in piranha solution, rinsed with deionised water and dried with a nitrogen gun. A few drops of the Ge NC dispersion dissolved in chloroform were dropped on a clean gold surface substrate. All spectra were acquired at room temperature and binding energies were referenced to the Au $4f_{7/2}$ line. All spectra were fitted with two peaks using a Shirley background.

Table 3-1: Synthetic conditions for the reactions carried out in this section

Entry	Precursor (Amount)	Surfactant (Amount)	Reducing Agent (Amount)	Catalyst (Amount)	Ligand (Amount)	Extracted to
1	$GeCl_4$ (0.876 mmol) *n*-BTCG (0.876 mmol)	N/A	*n*-BuLi (3.5 mmol)	N/A	N/A	Chloroform
2	$GeCl_4$ (0.876 mmol)	N/A	*n*-BuLi (3.5 mmol)	N/A	N/A	"
3	*n*-BTCG (0.876 mmol)	N/A	*n*-BuLi (3.5 mmol)	N/A	N/A	"
4	$GeCl_4$ (4.38 mmol)	DTAB (8.76 mmol)	$LiAlH_4$ (6 mmol)	H_2PtCl_6 (30 µmol)	1-Heptene (26.6 mmol)	"
5	"	"	"	"	Allylamine (26.6 mmol)	"
6	"	"	"	"	4-Pentenoic Acid (26.6 mmol)	"
7	"	"	"	"	Allyl Acetate (26.6 mmol)	"
8	"	"	"	"	1,2-epoxy-5-hexene (26.6 mmol)	"

DTAB: dodecyltrimethylammonium bromide, *n*-BTCG: *n*-butyltrichlorogermane, $LiAlH_4$: lithium aluminium hydride, *n*-BuLi: *n*-butyllithium and N/A: not applicable.

3.3 Results and Discussion

3.3.1 Alkyl Terminated Ge NCs

Figure 3-1 shows a TEM image of the butyl capped Ge NCs formed by the reduction of $GeCl_4$ and *n*-butyltrichlorogermane. No aggregation of the NCs was observed and the size distribution of the NCs was determined to be 3.9 ± 0.5 nm, see the corresponding size histogram.

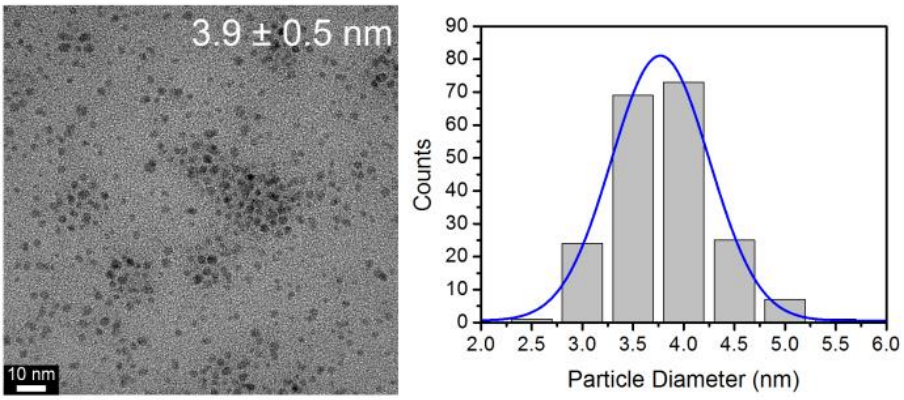


Figure 3-1: Left, TEM image of Ge NCs synthesised by the reduction of both *n*-butyltrichlorogermane and $GeCl_4$. Right, histogram of Ge NC diameters fitted using a Gaussian model

Ge NCs formed by the reduction of only *n*-butyltrichlorogermane also showed narrow size distributions with a reduced diameter (3.4 ± 0.4 nm, see Figure 3-2(a)), possibly due to the lesser amount of Ge precursor used in the synthesis. In contrast, Ge NCs prepared with an equivalent amount of $GeCl_4$ exhibited significant increases in both size and polydispersity, with an average diameter of 7.2 ± 0.6 nm, indicating that *n*-butyltrichlorogermane plays a role in regulating NC size and monodispersity, see Figure 3-2(b).

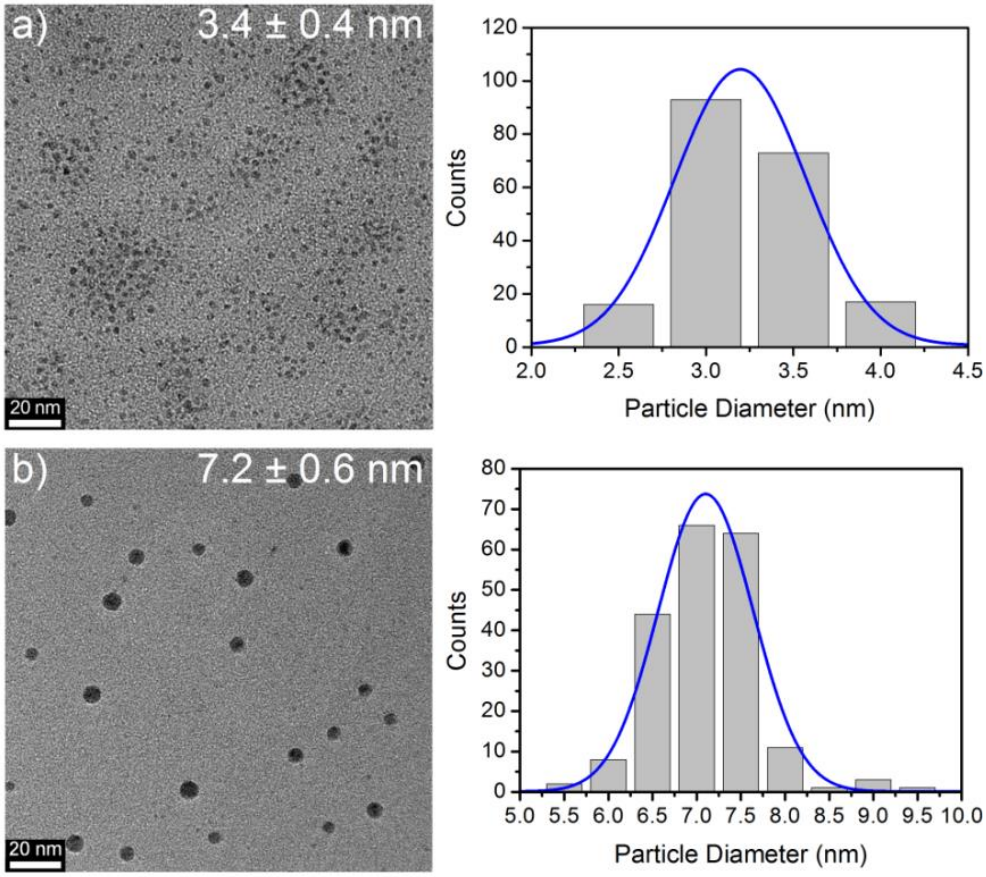


Figure 3-2: Left, TEM images and, right, size histograms and of Ge NCs produced by the reduction of a single precursor (a) *n*-butyltrichlorogermane and (b) $GeCl_4$

HR-TEM imaging was used in conjunction with SAED to confirm the crystallinity and establish the phase of the NCs formed; see Figure 3-3(a) and (b). HR-TEM images (Figure 3-3(a)) showed that the Ge NCs form a single crystalline domain, with a lattice *d* spacing (2.0 Å) matching the (220) reflection of the germanium unit cell. The fast fourier transform (FFT) of the HR-TEM image in Figure 3-3(a), inset, exhibits the characteristic pattern of the diamond germanium crystal structure, viewed down the [111] direction. SAED patterns of the Ge NCs (Figure 3-3(b)) showed reflections that could be indexed to Ge diamond cubic (*Fd3m*) lattice at 1; 3.3 Å (111), 2; 2.0 Å (220), 3; 1.7 Å (311), 4; 1.3 Å (331) and 5; 1.2 Å (422), respectively. EDX spectroscopy was employed to determine the elemental composition of the samples. Figure 3-3(c) shows an EDX spectrum recorded for the butyl capped Ge NCs. Characteristic Ge peaks were observed as well as Cu from the TEM grid support.

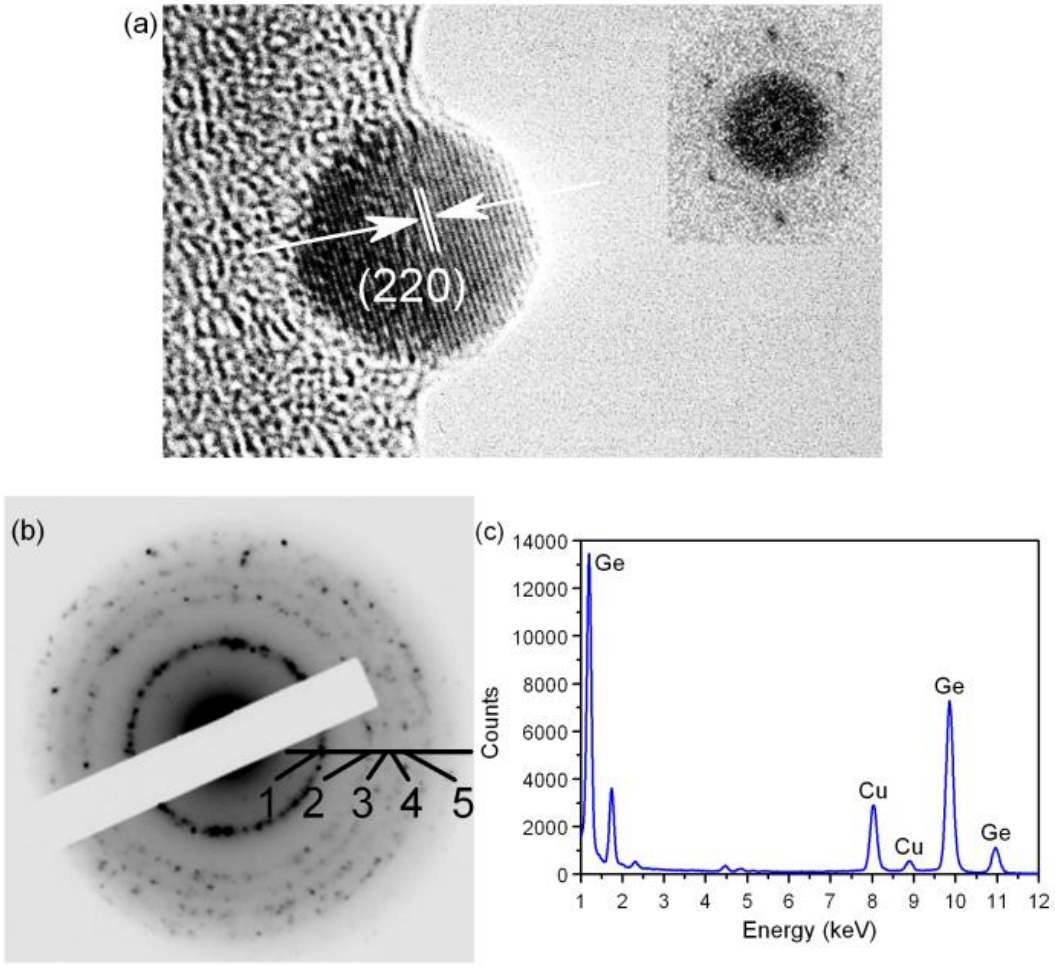


Figure 3-3: (a) HR-TEM of an individual Ge NC, inset shows an FFT pattern, (b) SAED pattern for the Ge NCs and (c) EDX spectrum

The surface of the Ge NCs was characterised by FTIR and XPS spectroscopy, see Figures 3-4 and 3-5, respectively. The peaks between 2855 and 2956 cm^{-1} are attributed to the CH_2 and CH_3 stretching modes of the alkyl group.[3] The peaks at 1465 and 1260 cm^{-1} are ascribed to the scissoring and bending of the Ge-C and Ge-CH_2 bonds, respectively, while the strong peak at 1375 cm^{-1} is assigned to the C-CH_3 symmetric stretching mode.[4, 5] The peak at 964 cm^{-1} is assigned to the Ge-O-Ge vibrations,[6] while the peaks below 900 cm^{-1} are a combination of the Ge-O and the Ge-C stretching modes,[7] consistent with a covalently attached alkyl layer and some surface oxidation.

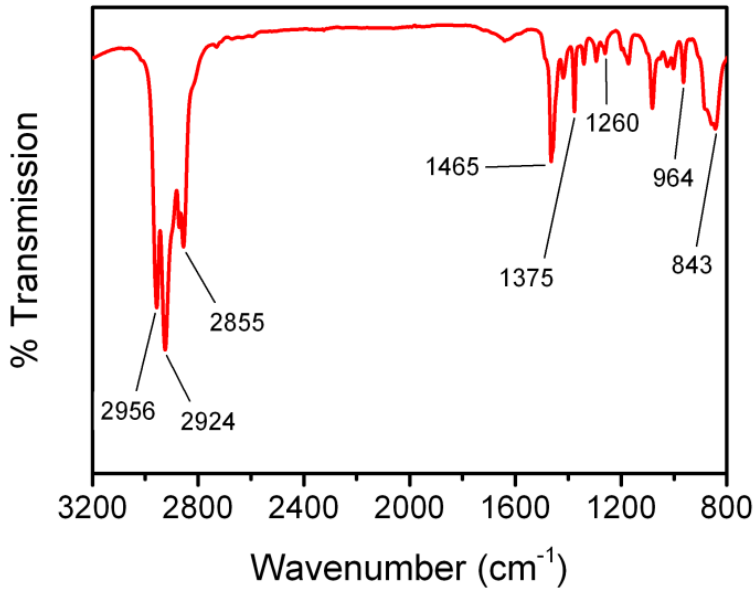


Figure 3-4: FTIR of the butyl capped Ge NCs produced by reduction of both germanium precursors

The XPS survey spectrum (Figure 3-5(a)) shows no peaks due to the presence of contaminants such as Li or Cl from the reducing agent or precursor materials demonstrating the purity of the samples, while the Si2s and Si2p peaks between 150 to 100 eV are due to the substrate used in the measurement. The Ge3d spectrum (Figure 3-5(b)) exhibits peaks at 30.5 and 32.2 eV, consistent with a partially oxidised Ge NC surface. The O1s spectrum (Figure 3-5(c)) is fitted with two components at 532.3 and 533.9 eV, assigned to C-O and Ge-O bonds, respectively. The C1s XPS spectrum (Figure 3-5(d)) has a strong peak at 284.8 eV, assigned to C-C/C-H bonding, with a minor peak at 286.4 due to C-O bonds.

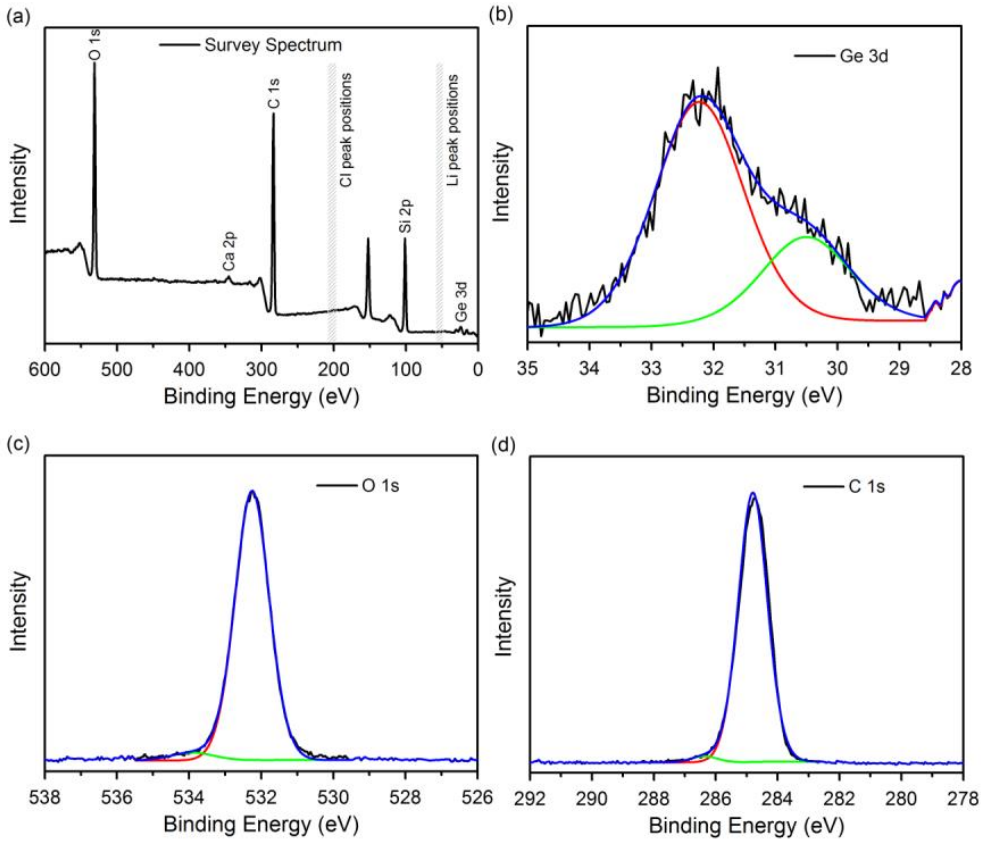


Figure 3-5: XPS spectra of the butyl capped Ge NCs produced by reduction of both germanium precursors

The optical properties of the butyl-terminated Ge NCs were investigated using UV-Vis absorbance, PL and PLE spectroscopy; see Figure 3-6(a). The UV-Vis spectrum shows a strong UV absorbance, with a small shoulder near 330 nm and an onset of absorbance at *ca.* 350 nm (3.5 eV), much higher in energy than the band gap of bulk Ge (0.6 eV). Similar spectral features have been previously reported in optical spectra of Ge NCs,[8, 9] which were assigned to direct transitions from Γ_{25} to split energy levels at Γ_{15}; the significant blue shift in the onset of absorption compared to the bulk Ge band gap energy suggests the presence of quantum confined carriers in the nanocrystals. The PLE spectrum shows a narrow peak centred at *ca.* 290 nm (4.3 eV), considerably in excess of the observed onset of absorbance at 3.5 eV, with additional shoulders at 310 nm and 330 nm. The complex surface chemistry of the Ge NCs revealed by FTIR and XPS measurements, suggests the involvement of a number of different surface states in the photoluminescence process, although it is possible that radiationless transfer to lower lying energy states occurs prior to

exciton recombination. The alkyl-terminated Ge NCs also exhibit a structured luminescence between 300-500 nm, with PL spectra clearly dependent on the excitation wavelength used; the wavelength position of the PL maximum red-shifts from 358 nm to 433 nm as the excitation wavelength is increased from 290 nm to 400 nm, see Figure 3-6(b).

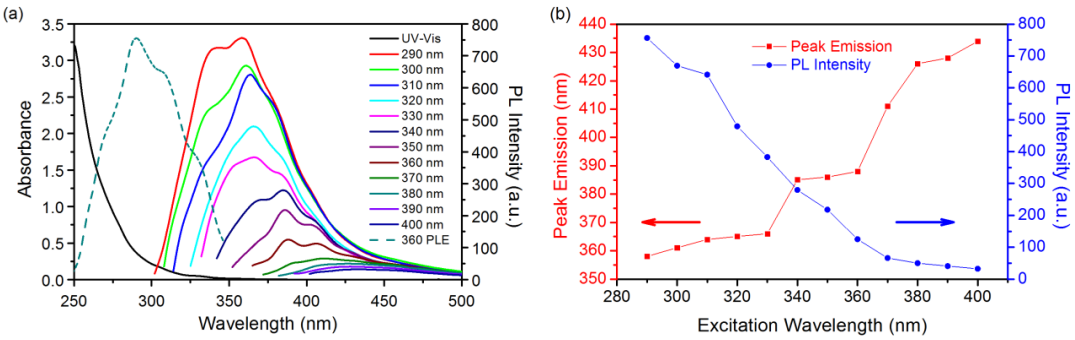


Figure 3-6: (a) UV-Vis, PL and PLE spectra for Ge NCs in chloroform. (b) PL peak maximum (red squares) and intensity (blue circles) *vs*. excitation wavelength

Increasing the excitation wavelength also results in a slight broadening of the PL spectrum (the FWHM increases from 72 nm to 91 nm) and a 10-fold decrease in the PL intensity as the excitation wavelength is increased. Ge NCs formed by the reduction of a single precursor show similar optical characteristics, see Figure 3-7. While the UV-Vis absorbance of NCs prepared with *n*-butyltrichlorogermane is blue shifted with respect to the $GeCl_4$-derived NCs, which would be expected due to their smaller size, both NC samples possess similar structured PL spectra with a marked dependence on excitation wavelength.

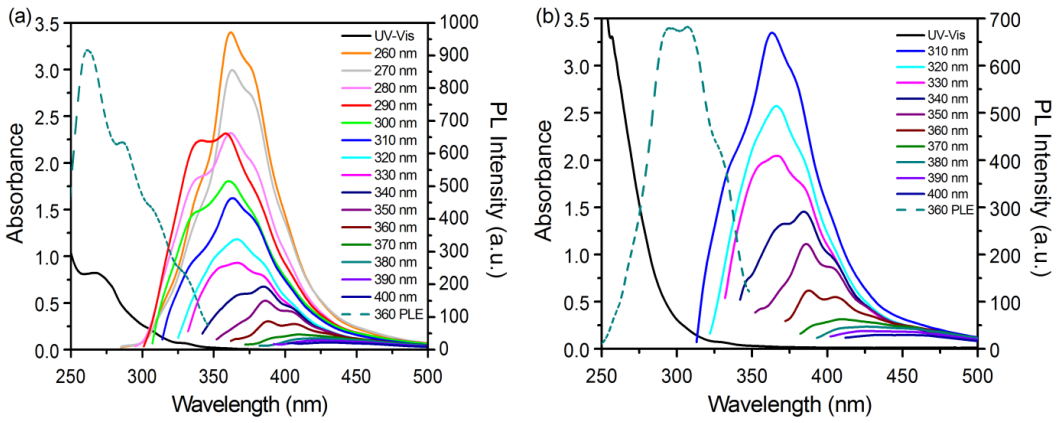


Figure 3-7: UV-Vis, PL and PLE spectra for Ge NCs produced by the reduction of a single precursor (a) *n*-butyltrichlorogermane and (b) $GeCl_4$

As germanium is an indirect band gap semiconductor, optical transitions are allowed only if phonons are involved in the transitions in order to conserve the crystal momentum. However, spatial confinement of electrons and holes inside a nanocrystal increases the uncertainty of their momentum, thus allowing optical transitions in which phonons are not involved. Due to the reduced number of energy levels and high surface to volume ratios inherent to semiconductor nanostructures, the chemical identity of surface states and the interface with the host matrix or environment must also be considered when describing their optical properties. As discussed previously, the underlying mechanism for PL in Ge NCs is usually described either in terms of exciton recombination confined entirely within the nanocrystal core, or a surface chemistry model that emphasizes the importance of energy states at the NC surface.[5, 10]

The PL spectra shown in Figures 3-6(a) and 3-7 exhibit a structured emission that is independent of nanocrystal size, implying that exciton recombination is not confined within the nanocrystal core, does not involve Ge band states, and that nanocrystal surface states are involved in the emission process. The structured luminescence observed from Ge NCs (the normalised PL spectra are almost entirely superimposable) implies that a number of surface or near-interface states are involved. This probably involves the oxygen-derived surface states (Ge-O_x and Ge-O-Ge) shown by FTIR and XPS, see Figures 3-4 and 3-5.

The excitation wavelength dependence of the PL could be attributed to sample polydispersity, with the larger NCs being selectively excited at longer wavelengths, but the narrow size distribution reported here rules out this explanation. Therefore, the origin of the excitation wavelength dependence is attributed to the involvement of different surface states in the luminescence process. Considering that the optimal excitation energies are considerably greater than the band gap energy, the sharp decrease in PL intensity at excitation wavelengths close to the absorption edge, the most reasonable interpretation is that excitation at shorter wavelengths results in efficient generation of excitons, which readily transfer to and/or recombine at surface states to give emission. Excitation at longer wavelengths may result in less efficient generation of excitons, or increased

transfer to non-radiative trap states, which would also contribute to the overall decrease in PL intensity.

The PL QY of NCs prepared with both germanium precursors was determined using 9,10-diphenylanthracene as the reference emitter. Figure 3-8(a) shows the integrated PL intensities of dilute dispersions of the butyl-capped Ge NCs in chloroform and 9,10-diphenylanthracene.

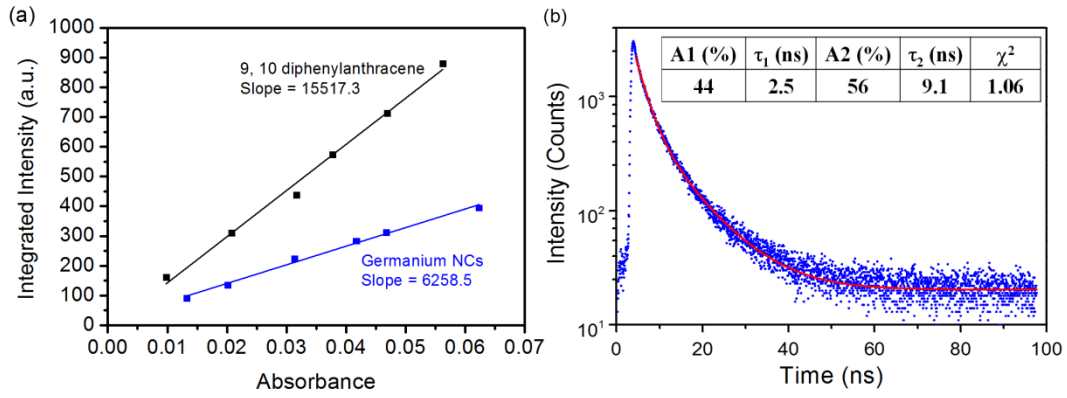


Figure 3-8: Integrated PL intensity *vs*. absorbance for dilute dispersions of Ge NC in chloroform and 9,10-diphenylanthracene in cyclohexane. (b) PL decays of Ge NC dispersions. Inset: Table of fitted time constants and relative amplitudes

The QY of the Ge NCs was calculated to be 37 %, one of the highest reported to date for solution synthesised Ge NCs. PL lifetimes of the Ge NCs were acquired (λ_{ex} = 402 nm); see Figure 3-8(b). Measured transients were well fitted (χ^2 < 1.1) to the sum of two weighted exponentials, yielding two lifetime components of 2.5 ns (44 %) and 9.1 ns (56 %), in line with previous reports.[9, 11-13] The nanosecond lifetimes observed provide further evidence that luminescence in Ge NCs is due to surface state recombination; band gap transitions in indirect semiconductors typically occur on microsecond timescales.

3.3.2 Surface Modified Ge NCs

Surface modified Ge NCs were formed by the reduction of $GeCl_4$ in the presence of the surfactant template dodecyltrimethylammonium bromide (DTAB), followed by chemical passivation of the NCs with different ligands. Figure 3-9(a) shows a low magnification TEM image of epoxy terminated Ge NCs (Ge NCs-epoxy) produced using this method. There is no evidence of aggregation and the NCs are relatively

monodisperse; Figure 3-9(b) shows a size histogram with a Gaussian curve fitted to the data. An average size of 4.1 ± 0.4 nm was determined based on a count of 200 NCs. HR-TEM imaging, see Figure 3-9(c), showed that the NCs are highly crystalline with lattice fringes corresponding to the (220) plane of the diamond cubic crystal structure which Ge adopts. The inset shows an FFT of the Ge NCs which is hexagonal in shape, typical for the germanium lattice structure. Figure 3-9(d) shows the SAED pattern obtained for these Ge NCs and characteristic reflections were seen that could be indexed to Ge diamond cubic (*Fd3m*) lattice at 2.0 Å (220), 1.3 Å (331) and 1.2 Å (422), respectively.

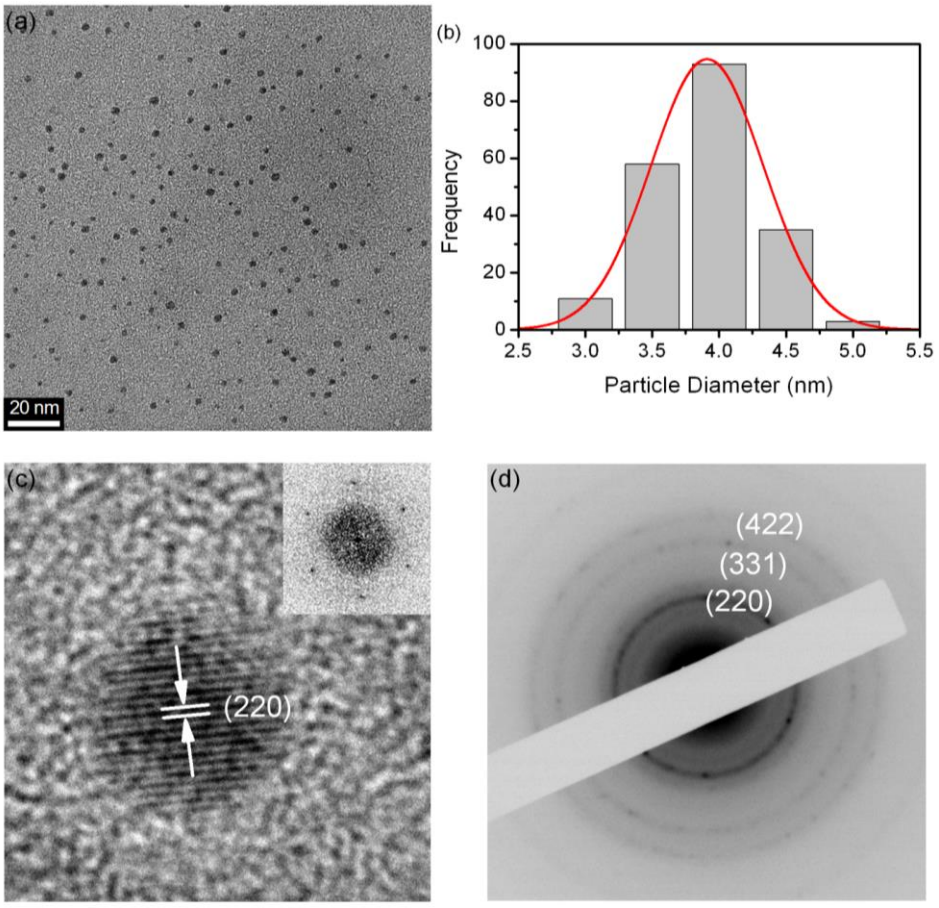


Figure 3-9: (a) Low magnification TEM image of epoxy terminated Ge NCs, (b) size histogram with a Gaussian curve fitted to the data, (c) HR-TEM of the NCs and (d) SAED pattern with the reflections characteristic of crystalline Ge indexed

Similar sized NCs were obtained with other functional groups on the NC surface, see Figure 3-10(a)-(d). This is expected as these NCs were produced using the same reaction conditions. Representative TEM images are shown in Figure 3-10 with different terminal groups, (a) acetate ($COOCH_3$) terminated Ge NCs (4.1 ± 0.4 nm),

(b) amine (NH_2) terminated Ge NCs (4.1 ± 0.4 nm), (c) carboxylic acid (COOH) terminated Ge NCs (4.1 ± 0.4 nm) and (d) and alkyl terminated Ge NCs (3.9 ± 0.5 nm). Inset in each image is the corresponding histogram for each sample with Gaussian curves fitted to the data.

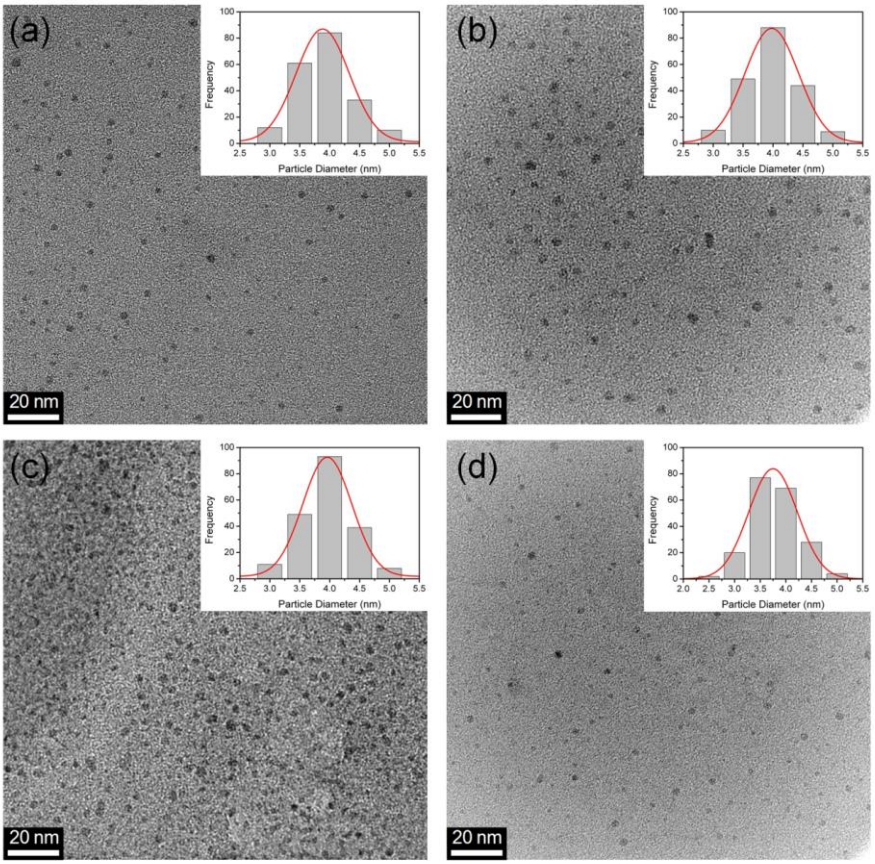


Figure 3-10: Low magnification TEM images of the NCs produced with (a) acetate terminations, (b) amine terminations, (c) carboxylic acid terminations and (d) alkyl terminations. Insets show histograms of the sizes

The surface modified Ge NCs were characterised by FTIR spectroscopy, see Figure 3-11. The features observed between 3000-2850 cm^{-1} are attributed to C-H stretching modes,[3] while the peaks near 1460 and 1260 cm^{-1} are ascribed to the scissoring and bending of the Ge-C and Ge-CH_2 bonds, respectively.[5] The peak at *ca.* 960 cm^{-1} is assigned to the Ge-O-Ge vibrations,[6] while the peaks below 900 cm^{-1} are a combination of the Ge-O and the Ge-C stretching modes.[7] These features are present in all spectra and are consistent with a covalently attached ligand layer with some surface oxidation.

The symmetrical stretching, or ring breathing mode, of the epoxy ring expected near 1250 cm^{-1},[3] is partially obscured and appears as a shoulder in the peak for the Ge-CH_2 bending mode. The peak at 1725 cm^{-1} in the spectrum for carboxylic acid terminated Ge NCs is attributed to the C=O stretching vibration, while the C-O-H in-plane bending mode near 1420cm^{-1} is obscured by the Ge-C scissoring mode.[3] The peak at 1610 cm^{-1}, is ascribed to the carboxylate anion, indicating partial dissociation of the acid. A C=O stretching mode with diminished intensity is also observed at 1734 cm^{-1} for the acetate terminated NCs, while the small peak at 1376 cm^{-1} is assigned to the C-CH_3 symmetric stretching mode. The spectra of the amine and alkyl terminated NCs is in good agreement with those presented previously.

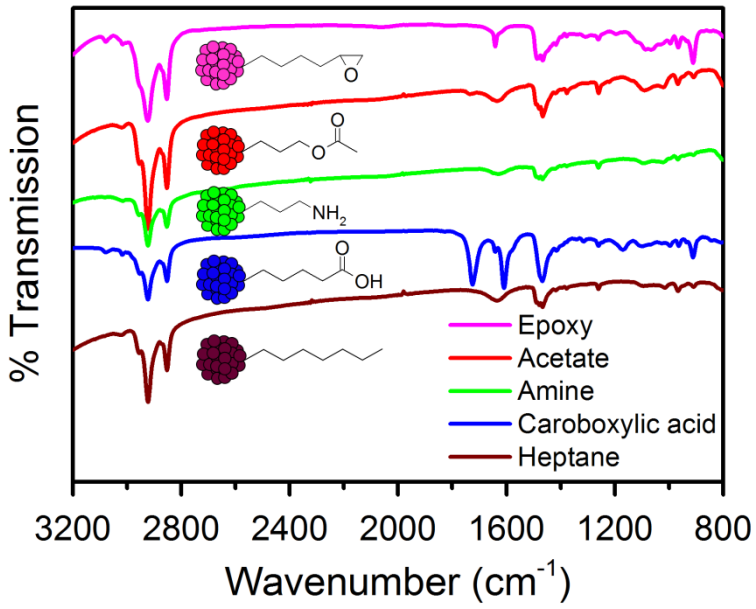


Figure 3-11: FTIR spectra for Ge NCs capped with different ligands

Surface ligands play a critical role in determining the properties of NCs, helping to shield the surface against oxidation and can chemically passivate the NC surface to minimise trap states, leading to efficient emission characteristics. The significant role played by the NC surface in tuning the optical properties of Ge NCs is well known; a number of ligands have therefore been explored for Ge NC surface capping and reported in the literature.[14, 15] Oleylamine was used as a capping ligand for Ge NCs.[16, 17] Oleic acid was also used as a capping ligand along with oleylamine and in the preparation of highly crystalline Ge NCs.[18] Hydrogermylation reactions with multiple carbon-carbon bond containing organic compounds is a common

method of modifying the hydrogen termination into a more stable Ge-C bond at the surface.[19] 1-octadecene[20, 21] was utilised to prepare Ge NCs dispersible in non-polar solvents and allylamine[11, 12] was used to prepare Ge NCs dispersible in water.

Figure 3-12 shows the PL spectra for differently terminated Ge NCs in chloroform (excitation wavelength 370 nm for all samples). Ge NCs passivated with an epoxy ligand showed a narrow emission centred at 410 nm with a tail extending into the visible region. As the capping ligand is changed to acetate, amine, carboxylic acid and alkyl groups, a concomitant red shift in the emission maximum is observed, with heptane terminated NCs exhibiting an emission maximum at 495 nm. As each sample contains similarly sized NCs (see Figures 3-9 and 3-10 above), these changes in the wavelength position of the PL maxima cannot be accounted for by quantum size effects and must be due to the presence of the different functional groups at the NC surface.

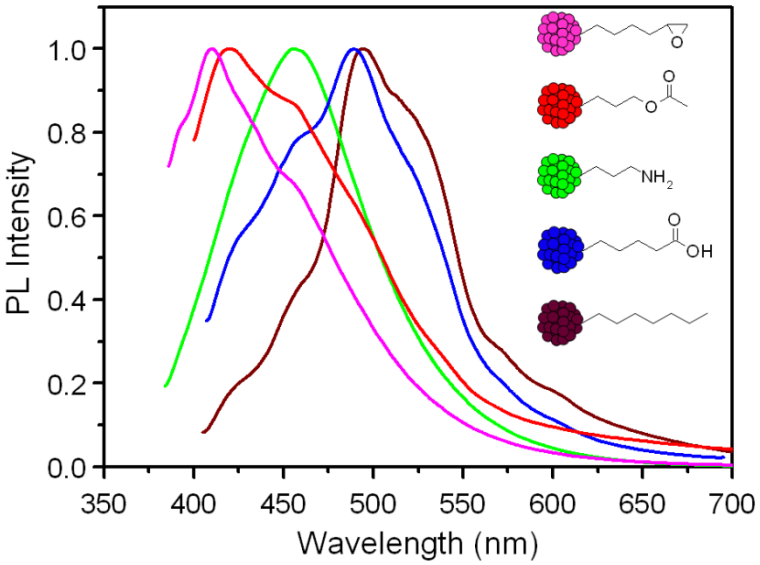


Figure 3-12: PL spectra of Ge NCs modified with different functional groups. An excitation wavelength of 370 nm was used for all samples

3.4 Conclusion

An efficient one-pot method for synthesis of size monodisperse, butyl-terminated Ge NCs with *in situ* surface passivation has been demonstrated. The advantage of this method is that it allows rapid synthesis and functionalisation of NCs with

minimal post-synthetic purification requirements. TEM imaging showed that the NCs are monodisperse and highly crystalline, while EDX and SAED confirmed the chemical identity and crystal phase of the NCs. FTIR and XPS confirmed that the Ge NCs were well passivated, with some oxidation of the nanocrystal surface. Optical spectroscopy confirmed that the NCs were in the strong quantum confinement regime, with significant involvement of surface oxide species in exciton recombination processes. Photoluminescence quantum yields were determined to be 37 %, one of the highest values reported for organically terminated Ge NCs.[c]

A synthetic method was also developed to produce size monodisperse Ge NCs with modified surface chemistries bearing carboxylic acid, acetate, amine and epoxy functional groups. TEM imaging showed that the modified Ge NCs were identical in size, while optical spectroscopy showed no changes in the absorption spectra. Direct comparison of the emission properties of the surface modified Ge NCs showed the wavelength position of the PL maxima could be moved over 85 nm from the UV to the blue/green, with a tail extending into the yellow/red.[d]

[c] Publications arising from this work: "Efficient One-Pot Synthesis of Monodisperse Alkyl-Terminated Colloidal Germanium Nanocrystals" *J. Nanopart. Res.,* 2014*, 16 (12), 1 - 8*

[d] Publications arising from this work: "Tuning the Photoluminescence Properties of Ge NCs Using Polarisable Ligands" *Nanoscale, Manuscript in preparation.*

3.5 References

1. Wang, J.; Sun, S.; Peng, F.; Cao, L.; Sun, L., Efficient One-Pot Synthesis of Highly Photoluminescent Alkyl-Functionalised Silicon Nanocrystals. *Chem. Commun.* **2011,** *47*, 4941.

2. Wilcoxon, J. P.; Provencio, P. P.; Samara, G. A., Synthesis and Optical Properties of Colloidal Germanium Nanocrystals. *Phys. Rev. B* **2007,** *76*, 199904.

3. Silverstein, R. M.; Bassler, G. C.; Morrill, T. C., *Spectrometric Identification of Organic Compounds*. Wiley: New York, 1991.

4. Socrates, G., *Infrared Characteristic Group Frequencies*. Wiley: Chichester, 1980.

5. Carolan, D.; Doyle, H., Size and Emission Color Tuning in the Solution Phase Synthesis of Highly Luminescent Germanium Nanocrystals. *J. Mater. Chem. C* **2014,** *2*, 3562.

6. Henderson, E. J.; Seino, M.; Puzzo, D. P.; Ozin, G. A., Colloidally Stable Germanium Nanocrystals for Photonic Applications. *ACS Nano* **2010,** *4*, 7683.

7. Taylor, B. R.; Kauzlarich, S. M.; Delgado, G. R.; Lee, H. W. H., Solution Synthesis and Characterization of Quantum Confined Ge Nanoparticles. *Chem. Mater.* **1999,** *11*, 2493.

8. Wilcoxon, J. P.; Provencio, P. P.; Samara, G. A., Synthesis and Optical Properties of Colloidal Germanium Nanocrystals. *Phys. Rev. B* **2001,** *64*, 035417.

9. Ghosh, B.; Sakka, Y.; Shirahata, N., Efficient Green-Luminescent Germanium Nanocrystals. *J. Mater. Chem. A* **2013,** *1*, 3747.

10. Dasog, M.; Yang, Z.; Regli, S.; Atkins, T. M.; Faramus, A.; Singh, M. P.; Muthuswamy, E.; Kauzlarich, S. M.; Tilley, R. D.; Veinot, J. G. C., Chemical Insight into the Origin of Red and Blue Photoluminescence Arising from Freestanding Silicon Nanocrystals. *ACS Nano* **2013,** *7*, 2676.

11. Warner, J. H.; Tilley, R. D., Synthesis of Water-Soluble Photoluminescent Germanium Nanocrystals. *Nanotechnology* **2006,** *17*, 3745.

12. Prabakar, S.; Shiohara, A.; Hanada, S.; Fujioka, K.; Yamamoto, K.; Tilley, R. D., Size Controlled Synthesis of Germanium Nanocrystals by Hydride Reducing Agents and Their Biological Applications. *Chem. Mater.* **2010,** *22*, 482.

13. Shirahata, N.; Hirakawa, D.; Masuda, Y.; Sakka, Y., Size-Dependent Color Tuning of Efficiently Luminescent Germanium Nanoparticles. *Langmuir* **2012,** *29*, 7401.

14. Taylor, B. R.; Fox, G. A.; Hope-Weeks, L. J.; Maxwell, R. S.; Kauzlarich, S. M.; Lee, H. W. H., Solution Preparation of Ge Nanoparticles with Chemically Tailored Surfaces. *Mater. Sci. Eng., B* **2002,** *96*, 90.

15. Tanke, R. S.; Kauzlarich, S. M.; Patten, T. E.; Pettigrew, K. A.; Murphy, D. L.; Thompson, M. E.; Lee, H. W. H., Synthesis of Germanium Nanoclusters with Irreversibly Attached Functional Groups: Acetals, Alcohols, Esters, and Polymers. *Chem. Mater.* **2003,** *15*, 1682.

16. Muthuswamy, E.; Iskandar, A. S.; Amador, M. M.; Kauzlarich, S. M., Facile Synthesis of Germanium Nanoparticles with Size Control: Microwave Versus Conventional Heating. *Chem. Mater.* **2012,** *25*, 1416.

17. Gerung, H.; Bunge, S. D.; Boyle, T. J.; Brinker, C. J.; Han, S. M., Anhydrous Solution Synthesis of Germanium Nanocrystals from the Germanium(II) Precursor Ge $[N(SiMe_3)_2]_2$. *Chem. Commun.* **2005,** 1914.

18. Vaughn, D. D., II; Bondi, J. F.; Schaak, R. E., Colloidal Synthesis of Air-Stable Crystalline Germanium Nanoparticles with Tunable Sizes and Shapes. *Chem. Mater.* **2010,** *22*, 6103.

19. Fok, E.; Shih, M. L.; Meldrum, A.; Veinot, J. G. C., Preparation of Alkyl-Surface Functionalized Germanium Quantum Dots *Via* Thermally Initiated Hydrogermylation. *Chem. Commun.* **2004,** 386.

20. Lee, D. C.; Pietryga, J. M.; Robel, I.; Werder, D. J.; Schaller, R. D.; Klimov, V. I., Colloidal Synthesis of Infrared-Emitting Germanium Nanocrystals. *J. Am. Chem. Soc.* **2009,** *131*, 3436.

21. Ruddy, D. A.; Johnson, J. C.; Smith, E. R.; Neale, N. R., Size and Bandgap Control in the Solution-Phase Synthesis of Near-Infrared-Emitting Germanium Nanocrystals. *ACS Nano* **2010,** *4*, 7459.

Chapter 4: Applications of Germanium Nanocrystals in Metal Ion Sensing

4.1 Introduction

Iron is a biologically important and indispensable element playing a vital role in oxygen uptake, oxygen metabolism and electron transfer in the body. Not only is iron involved in an enormous range of functions, it is also found in the whole gamut of life forms from bacteria to man. Iron is extremely abundant in the earth's crust and it is found in many biologically essential systems, while it is ranked as the second most important trace element in the human body. Deficiency or excess accumulation of iron can lead to anaemia (a condition in which there are too few red blood cells), organ failure and diseases.[1, 2] Measuring the level of ferric ions (Fe^{3+}) is a significant factor in the evaluation of water quality. Hence, there is on-going requirement for sensitive sensing strategies for detection of Fe^{3+}.

In this chapter we report the highly selective, fast and sensitive detection of Fe^{3+} ions by quenching of the blue PL from Ge NCs. As an introduction to this chapter, we recap the results obtained in Chapter 2, at the end of section 2.3.2, and give some sound reasoning as to why we chose the blue emitting Ge NCs over the larger green NCs for the sensing experiments. Following this, it is shown that the Ge NCs have a high sensitivity for the fast detection of Fe^{3+} over other metal ions (Al^{3+}, Cd^{2+}, Co^{2+}, Cu^{2+}, Fe^{2+}, Hg^{2+}, Mn^{2+}, Ni^{2+}, Pb^{2+}, Pd^{2+}, Pt^{4+}, and Zn^{2+}). The sensing platform was shown to be highly sensitive to Fe^{3+} with a lower detection limit of 54 ± 6 nM, while the quenching mechanism was unequivocally confirmed to be static by lifetime measurements, UV-Vis and close inspection of the quenched spectra. This nanosensor system could also detect Fe^{3+} in numerous real water samples such as tapwater, riverwater and lakewater, while PL "turn on" experiments demonstrated that the Fe^{3+} has a higher affinity for the NCs compared to other important molecules. To the best of our knowledge, this is also the first report of the use of luminescent NCs for label-free detection of a specific heavy metal ion in a specific formal charge state.

4.2 Experimental Section

4.2.1 Chemicals and Procedures

Chemicals. Phosphate buffered saline (PBS) (tablet), hydrochloric acid (HCl) (≥ 37 %), NaOH (BioUltra, for luminescence, ≥ 98.0 %), $AlCl_3•6H_2O$ (99 %), $Cd(ClO_4)_2•xH_2O$ (99.999 % trace metal basis), $CoCl_2$ (97 %), $CuCl_2$ (97 %), $CrK(SO_4)_2•12H_2O$ (≥ 98 %), $FeCl_2$ (98 %), $Fe(NO_3)_3•9H_2O$ (99.99 % trace metal basis), $HgCl_2$ (≥ 99.5 %), $MnCl_2$ (98 %), $NiCl_2$ (98 %), $PbCl_2$ (98 %), $PdCl_2$ (≥ 99.9 %), $H_2PtCl_6•H_2O$ (≥ 99.9 %), $Zn(CH_3COO)_2•2H_2O$ (99.999 % trace metal basis) were purchased from Sigma Aldrich Ltd. and stored under ambient atmosphere.

pH Measurements. 0.5 mL aliquots of a stock solution of Ge NCs were added to a series of PBS buffered solutions with different pH values (3-9). These solutions were formed by initially making up a 0.01 M phosphate buffer solution (1 tablet in 200 mL DI water), taking aliquots of this and adding either HCl or a 0.5 M NaOH solution to adjust the pH. The fluorescence intensity was measured at an excitation of 400 nm for both the blue and green NCs. Solution pHs were measured using an Oakton Acorn Series 6 pH meter calibrated to NIST traceable pH 4.01, 7.00 and 10.00 standards (Oakton).

Metal Ion Sensing. Standard metal ion stock solutions (10 mM) were prepared in DI water and different concentrations obtained by diluting these stock solutions. The detection of Fe^{3+} was performed in DI water at room temperature. In a typical assay, 2.5 mL of a particular concentration of Fe^{3+} was added to 0.5 mL Ge NCs, the solution was shaken and the PL spectra were subsequently recorded. The selectivity towards Fe^{3+} was confirmed by adding other metal ion solutions (50 µM) instead of Fe^{3+} in the same way. Tapwater samples were obtained from the tap in our lab, riverwater from the river Lee in Cork and lakewater from the Lough in Cork. Prior to any fluorescence measurements, the riverwater and lakewater were centrifuged at 11,000 rpm for 10 minutes and filtered through 0.22 µM PVDF membrane filters (Acrodisc). The tapwater was not purified. Fe^{3+} with different concentrations was prepared in these real water samples and then analysed using the proposed method above.

PL "Turn-On" Experiment. For the PL "turn-on" experiments, Fe^{3+} at a concentration of 600 µM was used to quench the nanocrystal emission. After addition of 2.5 mL of the Fe^{3+} to 0.5 mL of the NCs, 2.5 mL of the sequestration molecule was added, the solution was stirred and the PL spectra recorded. 4 molecules were tested, namely dopamine (DA), melamine (Mel), 3,4-dihydroxyphenylacetic acid (3,4 DHPA) and sodium phosphate monobasic monohydrate (Phos). To test if the molecules could bind to the Fe^{3+} first, the experiment was carried out in the same manner, except that the Ge NCs were added last instead of first.

4.2.2 Characterisation

Optical Characterisation

UV-Vis absorption spectra were recorded using a Shimadzu UV PC-2401 spectrophotometer equipped with a 60 mm integrating sphere (ISR-240A, Shimadzu). Spectra were recorded at room temperature using a quartz cuvette (1 cm) and corrected for the solvent absorption. Photoluminescence spectra were recorded using an Agilent Cary Eclipse spectrophotometer. Nanosecond lifetime measurements were performed as described in the previously (see Section 2.2.3).

4.3 Results and Discussion

4.3.1 Selection of Ge NCs for Metal Ion Sensing

Figure 4-1(a) shows the integrated PL intensity of dilute dispersions of the 3.9 nm Ge NCs compared with solutions of 9,10-diphenylanthracene recorded under identical excitation conditions. The QY of the 3.9 nm NCs was calculated to be 21.5 %. Figure 4-1(b) shows the integrated PL intensity of dilute dispersions of the 6.8 nm Ge NCs compared with aqueous solutions of fluorescein. The QY of the 6.8 nm Ge NCs was found to be 6.2. PL lifetimes of the Ge NCs were acquired; see Figure 4-1(c). The average lifetime was calculated to be 6.1 ns for the 3.9 nm NCs and 7.8 ns for the 6.8 nm NCs, consistent with previous reports. The difference in PL lifetimes between the NC fractions is attributed to the involvement of different surface states in the luminescence process.

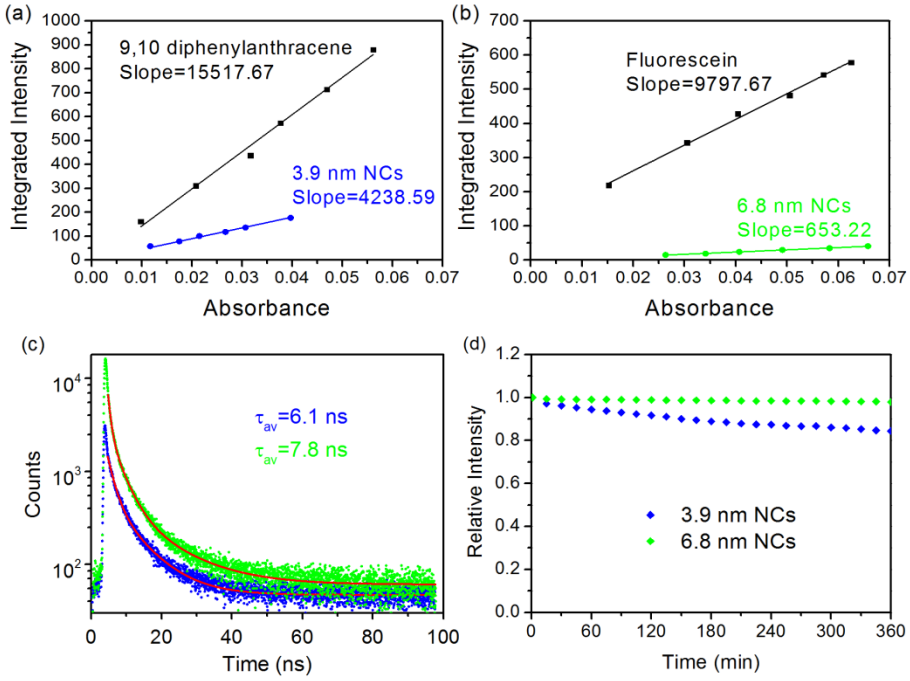


Figure 4-1: Integrated PL intensity *vs.* absorbance for dilute dispersions of (a) 3.9 nm Ge NCs and 9,10 diphenylanthracene, (b) 6.8 nm Ge NCs and fluorescein. (c) PL decays of both NC samples and (d) long-term PL stability of both samples recorded over 6 hours

The involvement of different surface species is demonstrated by PL measurements of the different Ge NC fractions taken under different pH conditions, see Figure 4-2.

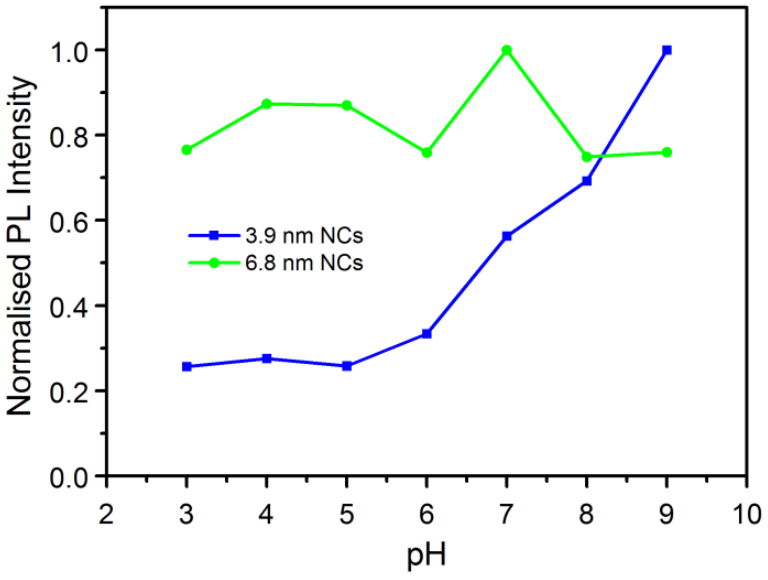


Figure 4-2: Normalised PL intensity of 3.9 nm and 6.8 nm Ge NCs as a function of pH

The 3.9 nm blue emitting NCs shows a strong response to the presence of H^+ ions, with a *ca.* 75 % decrease in PL intensity observed as the pH is lowered from 9.0 to 3.0. In contrast, the luminescence intensity of larger 6.8 nm NCs is insensitive to pH variations, implying that recombination does not involve surface species that are responsive to the presence of positive ions. As a result, luminescence quenching studies for the detection of metal ions in aqueous solution focused on the use of the brighter, more responsive 3.9 nm sized NCs. Both Ge NC fractions exhibit good to excellent long-term PL stability, decreasing by only 15 % for the 3.9 nm NCs and only 2 % for the 6.8 nm NCs over a period of 6 hours, see Figure 4-1(d).

4.3.2 Metal Ion Sensing

The luminescence quenching response of the blue emitting Ge NC to the presence of different metal ions (Al^{3+}, Cd^{2+}, Co^{2+}, Cu^{2+}, Fe^{2+}, Fe^{3+}, Hg^{2+}, Mn^{2+}, Ni^{2+}, Pb^{2+}, Pd^{2+}, Pt^{4+}, and Zn^{2+} ions), at a concentration of 50 µM in aqueous solution, is shown in Figure 4-3(a). It was found that the Ge NCs exhibited a substantial (*ca.* 20 %) decrease in the PL intensity in the presence of Fe^{3+} ions only; while a modest response (typically less than 5% change) was observed for the other metal ions examined. Interestingly, it is evident that the PL intensity of the Ge NCs in the presence of Fe^{2+} showed no decrease in intensity (in fact, a minor increase was observed), demonstrating that the nanocrystals can be used to selectively detect Fe^{3+} ions. Exposure tests carried out with Al^{3+} showed no evidence of a quenching response, indicating that the quenching response is selective towards iron, and not simply to the formal charge of the metal ions. Experiments carried out with Pt ions (formal charge: +4) also showed no change in PL intensity. This unusual selectivity demonstrated for a specific element and charge state make the Ge NCs a promising chemosensing platform for the highly efficient and sensitive detection of Fe^{3+}. The response time of this sensor was elucidated by monitoring the dependence of relative PL intensity on the reaction time; see Figure 4-3(b). The results showed that the PL intensity had reached a constant value within 2 minutes of addition of Fe^{3+}, indicating fast quenching kinetics; thereafter the PL intensity remains constant, see inset in Figure 4-3(b).

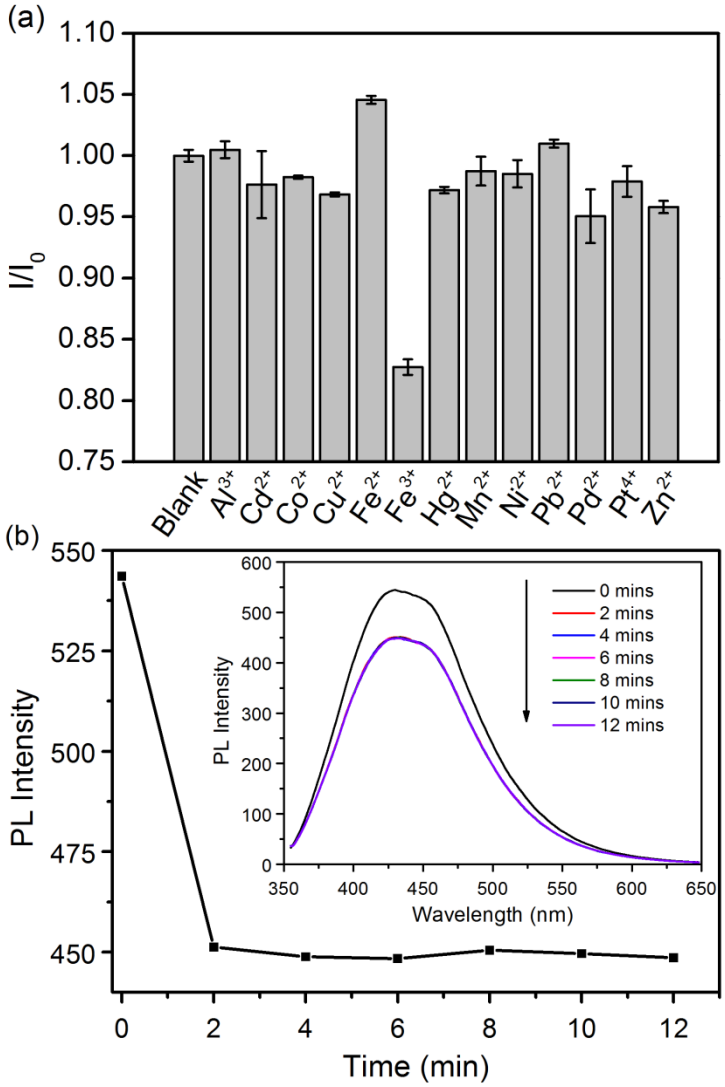


Figure 4-3: (a) Normalised response for the effect of various different metal ions on the Ge NC fluorescence. (Concentration of ions is 50 µM). Error bars were calculated from the standard deviation of 6 measurements (b) Time-dependent PL intensity obtained for the interaction between Ge NCs and Fe^{3+} ions. Inset shows the spectra obtained

PL spectra were recorded at a series of different Fe^{3+} concentrations in order to evaluate the sensitivity of our Ge NCs sensing system for Fe^{3+} detection, see Figure 4-4(a). Increasing the Fe^{3+} concentration from 0.25 µM to 800 µM resulted in a concomitant decrease in the PL intensity. Figure 4-4(b) shows the dependence of I_0/I (red squares) on Fe^{3+} concentration, where I_0 and I are the PL intensities before and after addition of the analyte, respectively. The quenching data shows a linear relationship that is in excellent agreement with the Stern-Volmer relationship,

$I_0/I=1+K_{SV}[Q]$, where K_{SV} is the Stern-Volmer constant and [Q] is the concentration of the quencher (Fe^{3+}).

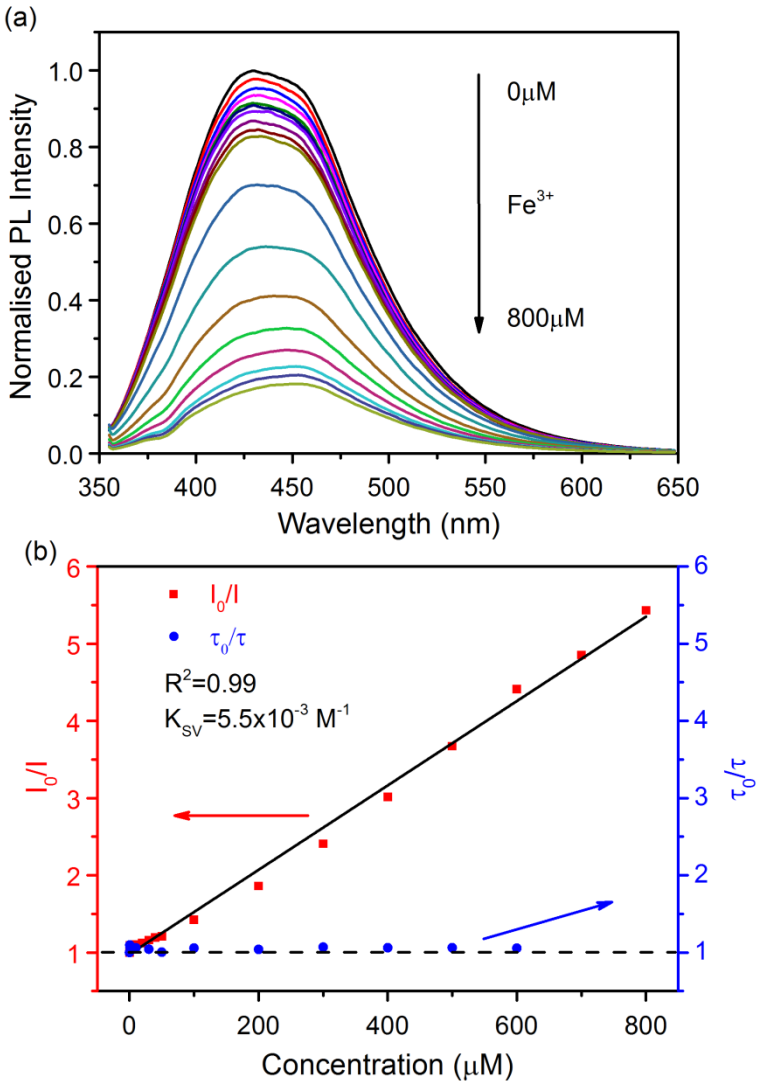


Figure 4-4: (a) Representative photoluminescence spectra of Ge NCs in the presence of increasing Fe^{3+} concentrations (0-800 μM). (b) The relationship between I_0/I (red squares) and τ_0/τ (blue circles) with the concentration of Fe^{3+} ions within the range of 0-800 μM. The excitation was fixed at 340 nm for all spectra. I_0 and I are the PL intensities in the absence and presence of Fe^{3+} ions, respectively. τ_0 and τ are the lifetimes in the absence and presence of Fe^{3+} ions, respectively

The lack of curvature in the plot indicates that only one quenching mechanism is present. Fitting the experimental data points with a least squares linear model over the range 0-800 μM yielded K_{SV} = 5.5x10^{-3} M^{-1} with a correlation coefficient, R^2 = 0.99. The limit of detection (LOD) was determined to be 0.83 ± 0.02 μM, determined from the standard deviation of the blank (noise), LOD = $3\sigma_{blank}/K_{SV}$,

according to the guidelines set by the International Union of Pure and Applied Chemistry (IUPAC).[3] A smaller LOD (54 ± 6 nM) could be obtained if the fitting was confined to the low concentration range (0.0-1.0 µM, however this resulted in a lower correlation coefficient (R^2 = 0.98) due to the fewer number of data points available for fitting, see Figure 4-5.

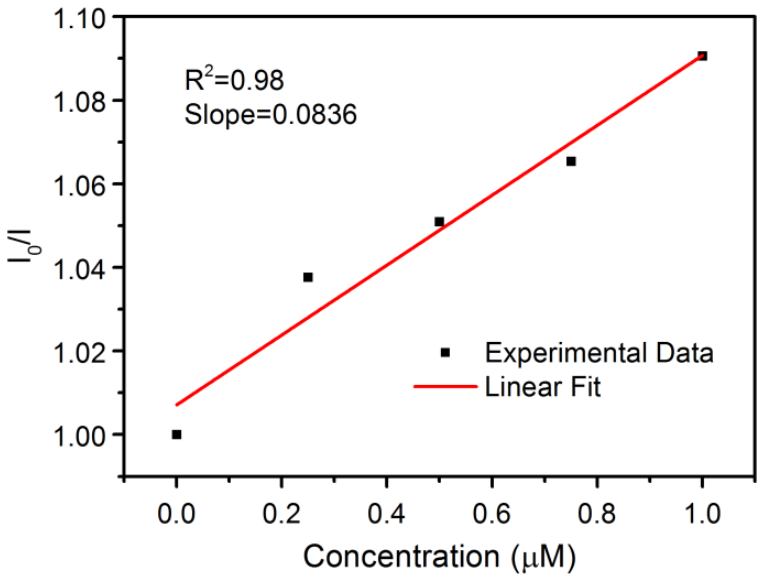


Figure 4-5: I_0/I *vs.* concentration for the linear range 0 to 1 µM

Fluorescence quenching data from intensity measurements alone can be explained by either static or dynamic processes. Dynamic (or collisional) quenching occurs when the analyte (quencher) interacts with the excited state of the luminophore, resulting in a change in the lifetime of the excited state. The change in lifetime occurs because dynamic quenching is an additional rate process which depopulates the excited state, hence $I_0/I = \tau_0/\tau$, where τ_0 and τ are the excited state lifetimes in the absence and presence of the quencher, respectively. In contrast, static quenching results from the formation of a non-emissive ground state complex between the analyte and the nanocrystal: as the PL originates from non-complexed Ge NCs, the emissive lifetimes are unaffected. Thus, the measurement of fluorescence lifetimes is the most definitive method to distinguish between dynamic and static quenching. To determine the quenching mechanism, the PL lifetimes of the Ge NCs were measured; see blue symbols in Figure 4-4(b).Increasing

the Fe^{3+} concentration has no effect on the lifetime of the Ge NCs and τ_0/τ remains constant, consistent with the presence of only the static quenching process.

Another way to distinguish between static and dynamic quenching is by examination of the absorption spectra of the emitting species. Dynamic quenching only affects the excited states and so no change in the absorption spectrum should occur. Conversely, static quenching involves ground-state complex formation which will result in alteration of the absorption spectrum of the fluorophore. Confirmation of the mechanism was obtained from UV-Vis spectroscopy of the Ge NCs, see Figure 4-6. In the absence of Fe^{3+}, the Ge NCs absorb primarily in the UV region with a shoulder at *ca.* 290 nm and an onset of absorption at *ca.* 350 nm. Addition of Fe^{3+} ions to the NCs results in a red shift in the position of this shoulder to *ca.* 300 nm and the appearance of a second shoulder at *ca.* 260 nm is observed, demonstrtaing that the Fe^{3+} induced PL quenching is due to formation of a non-emissive nanocrystal-analyte complex.[4-6]

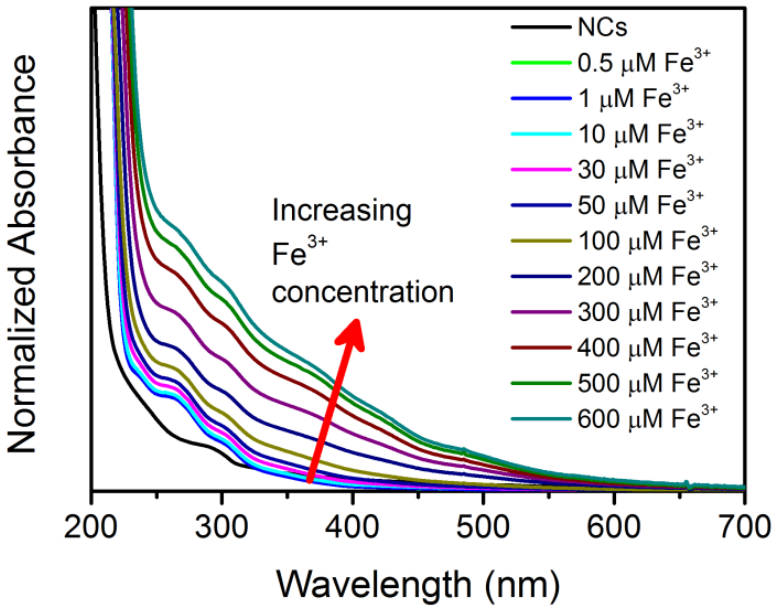


Figure 4-6: Normalised UV-Vis spectra for the Ge NCs before, and after the addition of increasing concentrations of Fe^{3+}

Plotting the peak emission wavelength against Fe^{3+} concentration (Figure 4-7) shows that the spectral wavelength maximum red-shifts by about 25 nm from *ca.* 430 nm to *ca.* 455 nm as the Fe^{3+} concentration is increased from 0-800 µM. This

obvious change in the PL spectra indicates a change in the surface states of the NCs has occurred, thus providing further evidence of Fe^{3+} binding to the NC surface.[4-7]

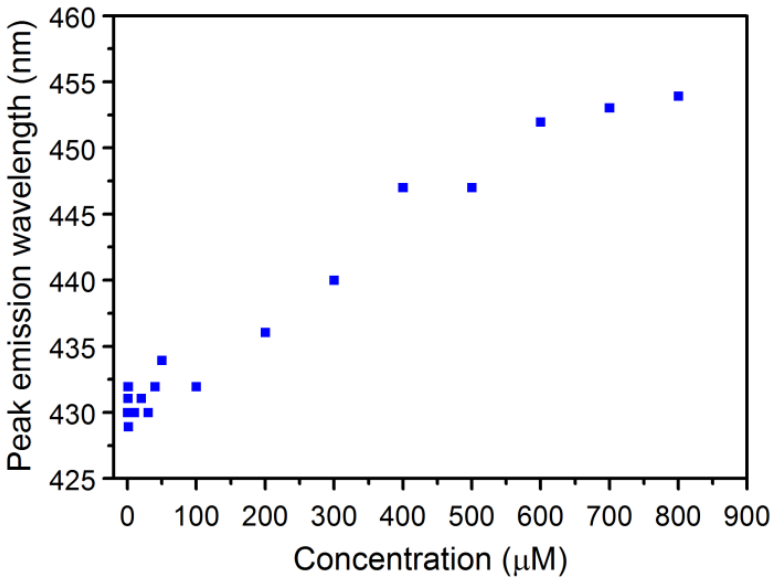


Figure 4-7: Variation of the peak emission wavelength as a function of the Fe^{3+} concentration

The ability of the Ge NCs to discriminate between Fe^{2+} and Fe^{3+} ions in solution may also be interpreted in terms of binding of ions to oxygeneous species at the NC surface. Previously reported XPS measurements Ge NCs showed the presence of significant amounts of oxygenic Ge−O_x species at the surface, which are known to readily bind hard acids such as Al^{3+}, Cr^{3+} and Fe^{3+}. In contrast, borderline acids such as Co^{2+}, Fe^{2+}, Ni^{2+}, Cu^{2+}, Zn^{2+} and Pb^{2+} show an affinity for nitrogen containing ligands such as amines. However, at the pHs typically used in these experiments (the pH of the DI water used is 7.2), the amine ligands (pKa = 9.5-10.5) would be fully protonated, thus lessening their ability to bond to the positively charged ions. In contrast, the higher acidity of Ge-O_x species allows them to readily bind Fe^{3+} ions from solution, resulting in fluorescence quenching. However, the absence of a quenching response to the presence of 50 μM Al^{3+}, see Figure 4-3(a), suggests that the interaction between the NC surface and the metal ions is not fully understood.

Previous reports on Fe^{3+} detection have limitations including a narrow linear detection range,[8-21] lack of selectivity,[16-19, 21-23] lack of real water analysis[8, 9, 11, 12, 14] and insufficient understanding of the quenching mechanism.[12, 15, 19-22, 24] The

excellent specificity, combined with high sensitivity and fast response time, suggested that the Ge NCs were applicable for detection Fe^{3+} in real water samples. The performance of the Ge NC sensing platform for Fe^{3+}detection was tested on samples obtained from drinkable (tap) water supplies, and fresh water samples from local rivers and lakes, see Figure 4-8(a)-(f).

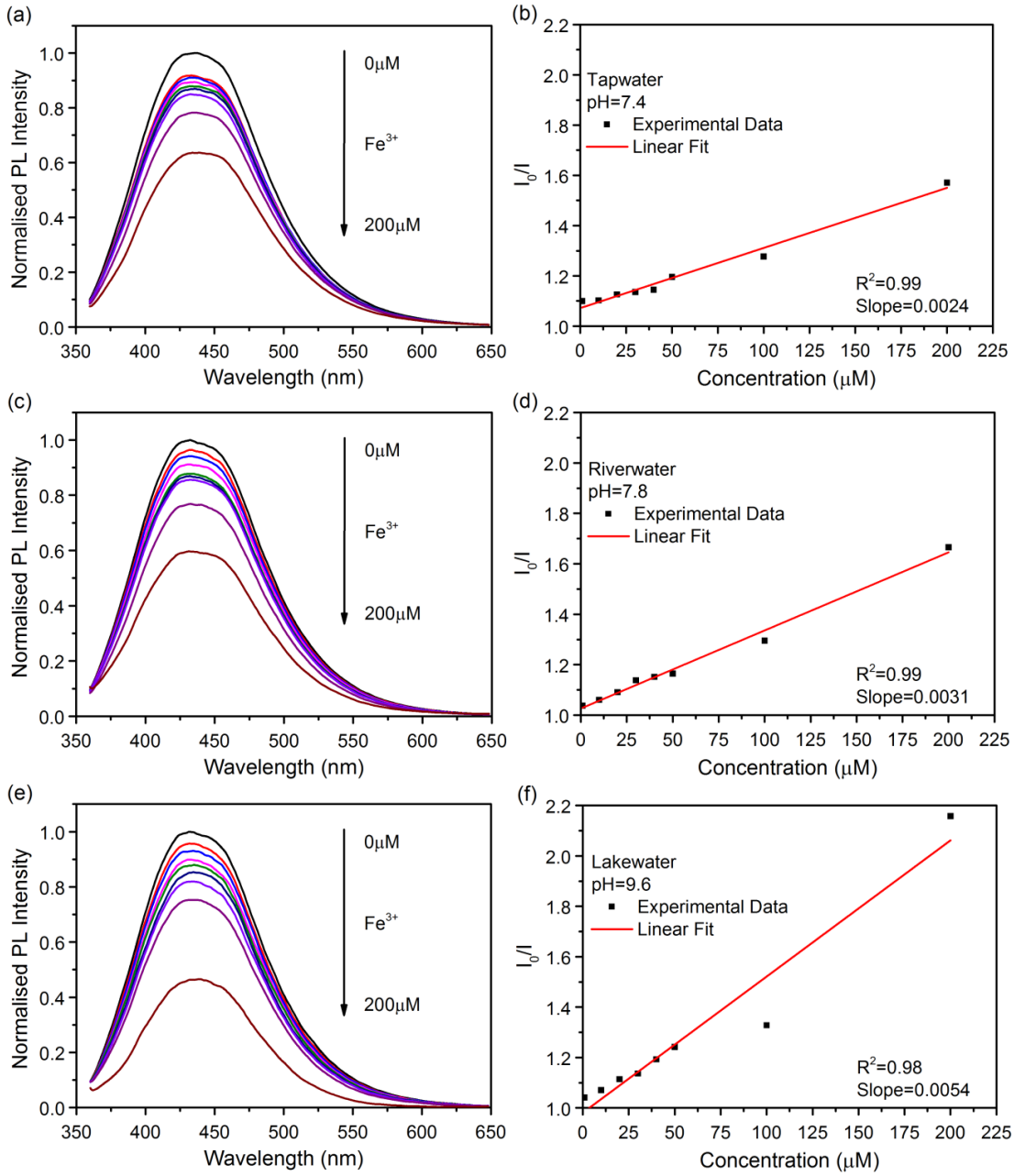


Figure 4-8: . Photoluminescence spectra (left) and I_0/I *vs.* concentration (right) of Ge NCs measured for Fe^{3+} concentrations from 1 to 200 μM in tapwater, (a) and (b), riverwater, (c) and (d) and lakewater (e) and (f). The excitation was fixed at 340 nm for all spectra. I and I_0 are the PL intensities in the presence and absence of Fe^{3+} ions, respectively

Despite the presence of minerals, organic matter and other contaminants, the Ge NCs exhibited a linear relationship between PL intensity and Fe^{3+} concentration (1-200 μM range) for all the real water samples, satisfying the US Environmental Protection Agency requirements (0.3 mg/L ≈ 5.4 μM) for Fe^{3+} levels in drinkable water supplies.

The pH of the water samples varies from 7.4 to 9.6, depending on the source, see legends on Figure 4-8 (b), (d) and (f)). This increase in pH was accompanied by an increase in the slope of the line obtained from plotting I_0/I *vs.* concentration. When the detection limit was calculated for these water samples for the concentration range 0-200 μM, using $3\sigma_{blank}/K_{SV}$, there was a decrease in the LOD (i.e. a lower LOD) as the pH of the sample increased. This general trend is interesting and is in accordance with the trend we see in Figure 4-2 for the fluorescence dependence on the pH; as the pH increased, the PL intensity also increased. This demonstrates that when a higher pH is used (and therefore a higher PL intensity) we obtain a better response from the sensing system to the analyte.

Table 4-1 shows that the recovery of Fe^{3+} was between 97-110 % for the real water samples, demonstrating the applicability and robustness of this detection procedure and showing that this system has good potential for detection of Fe^{3+} in environmental samples.

Various groups have demonstrated the reversibility of the PL quenching process by addition of a chelating or binding agent which sequesters the metal ion, thus removing it from the NC surface and restoring the NC luminescence.[12, 16, 20, 25-27] Following this idea, experiments were carried out with 4 candidate sequestration molecules, dopamine (DA), melamine (Mel), 3,4-dihydroxyphenylacetic acid (3,4 DHPA) and sodium phosphate monobasic monohydrate (Phos).

Table 4-1: Determination of Fe^{3+} in real water samples

Sample	Amount added (μM)	Measured (μM)	Recovery (%)
	1	1 ± 0.01	99.2 ± 1.4
	10	10 ± 0.1	99.9 ± 1.4
	20	19.9 ± 0.3	99.5 ± 1.4
Tapwater	30	30.6 ± 0.4	102.1 ± 1.2
	40	41.7 ± 0.6	104.2 ± 1.5
	50	50.5 ± 1.3	101.1 ± 2.5
	100	111.5 ± 1	111.5 ± 1
	1	1.1 ± 0.01	105.1 ± 0.9
	10	10.4 ± 0.1	103.8 ± 0.8
	20	20.5 ± 0.2	102.7 ± 0.9
Riverwater	30	30.6 ± 0.3	101.9 ± 1.1
	40	41.4 ± 0.5	103.6 ± 1.3
	50	51.9 ± 0.6	103.8 ± 1.3
	100	110 ± 1.1	110 ± 1.2
	1	1 ± 0.01	104.7 ± 1.1
	10	10.3 ± 0.2	102.8 ± 1.7
	20	20.1 ± 0.2	100.7 ± 1
Lakewater	30	30.6 ± 0.3	102.1 ± 1.2
	40	40 ± 0.8	100 ± 2
	50	48.7 ± 0.9	97.3 ± 1.7
	100	107.3 ± 1.1	107.3 ± 1.1

These sequestration molecules were added after the PL of the Ge NCs had been quenched by addition of 600 µM Fe^{3+}, see Figure 4-9. No increase in the PL intensity was observed after addition of 200 µM of the chelating agents was added (see black bars), suggesting that the Fe^{3+} ions had a greater affintity for the Ge NC surface. To address this point, the sequestration molecules were instead mixed with Fe^{3+} ions prior to mixing with the Ge NCs, see the red bars in Figure 4-9. However, as may be seen from the graph, this had no noticeable effect, with a similar degree of PL quenching observed irrespective of which chelating agent was used. Adding a large excess (10 mM, see blue bars in Figure 4-9) also had no effect, demonstrating that the Fe^{3+} ions have a very high affinity for the NC surface, which provides further suport for PL quenching *via* a strong ground state complex formation between Fe^{3+} and the Ge NCs.

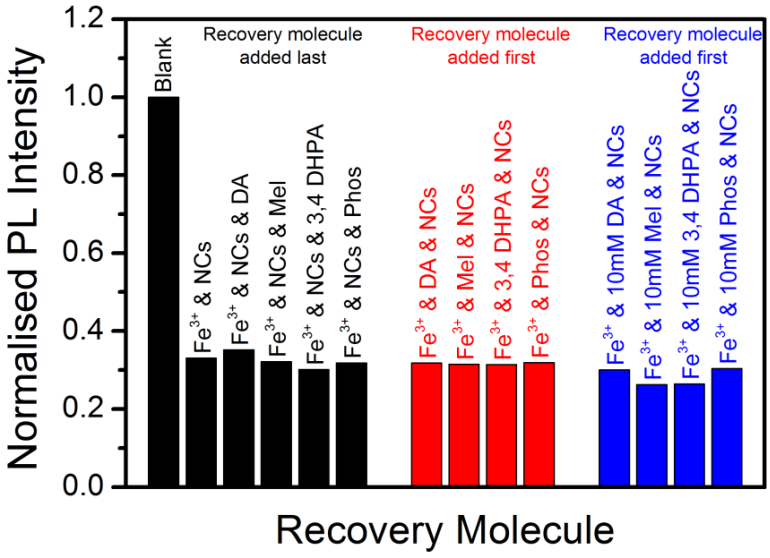


Figure 4-9: Normalised PL response for the PL recovery test

4.4 Conclusion

For the first time, we have reported the selective, fast and sensitive detection of Fe^{3+} ions by quenching of amine-terminated Ge NC PL, without the need for specific labelling groups. A linear relationship between the luminescence quenching and Fe^{3+} concentration was observed from 0.25 µM to 800 µM, with an upper limit of detection of 0.83 ± 0.02 µM and a lower LOD of 54 ± 6 nM. The Ge NCs show

excellent selectivity toward Fe^{3+} ions, with no quenching of the fluorescence signal induced by the presence of Fe^{2+} ions, allowing for solution phase discrimination between ions of the same element with different formal charges. The luminescence quenching mechanism was confirmed by lifetime and absorbance measurements as well as detailed inspection of the PL spectra. Results from PL "turn-on" experiments showed that Fe^{3+} has a higher affinity for the Ge NCs surface over various sequestering molecules. The applicability of this assay for the detection of Fe^{3+} in real water samples was successfully demonstrated, highlighting the robustness of this nanosensor and shows that it could be used in environmental water samples. This is the first report of the use of luminescent NCs for label-free detection of a specific heavy metal ion in a specific formal charge state.[e]

[e] Publications arising from this work: "Germanium Nanocrystals as Luminescent Probes for Rapid, Sensitive and Label-Free Detection of Fe^{3+} Ions" *Nanoscale, 2015, 7 (12), 5488 - 5494*

4.5 References

1. Andrews, N. C., Disorders of Iron Metabolism. *N. Engl. J. Med.* **1999,** *341*, 1986.

2. Galaris, D.; Skiada, V.; Barbouti, A., Redox Signaling and Cancer: The Role of "Labile" Iron. *Cancer Lett.* **2008,** *266*, 21.

3. Analytical Methods, C., Recommendations for the Definition, Estimation and Use of the Detection Limit. *Analyst* **1987,** *112*, 199.

4. Isarov, A. V.; Chrysochoos, J., Optical and Photochemical Properties of Nonstoichiometric Cadmium Sulfide Nanoparticles: Surface Modification with Copper(II) Ions. *Langmuir* **1997,** *13*, 3142.

5. Xia, Y.-S.; Cao, C.; Zhu, C.-Q., Two Distinct Photoluminescence Responses of CdTe Quantum Dots to Ag (I). *JOL* **2008,** *128*, 166.

6. Eychmüller, A.; Hässelbarth, A.; Weller, H., Quantum-Sized HgS in Contact with Quantum-Sized CdS Colloids. *JOL* **1992,** *53*, 113.

7. Dong, C.; Qian, H.; Fang, N.; Ren, J., Study of Fluorescence Quenching and Dialysis Process of CdTe Quantum Dots, Using Ensemble Techniques and Fluorescence Correlation Spectroscopy. *J. Phys. Chem. B* **2006,** *110*, 11069.

8. Singh, N.; Mulrooney, R. C.; Kaur, N.; Callan, J. F., A Nanoparticle Based Chromogenic Chemosensor for the Simultaneous Detection of Multiple Analytes. *Chem. Commun.* **2008,** 4900.

9. Liu, S.-d.; Zhang, L.-w.; Liu, X., A Highly Sensitive and Selective Fluorescent Probe for Fe^{3+} Based on 2-(2-Hydroxyphenyl)Benzothiazole. *New J. Chem.* **2013,** *37*, 821.

10. Yang, M.; Sun, M.; Zhang, Z.; Wang, S., A Novel Dansyl-Based Fluorescent Probe for Highly Selective Detection of Ferric Ions. *Talanta* **2013,** *105*, 34.

11. Zhang, Y.; Wang, G.; Zhang, J., Study on a Highly Selective Fluorescent Chemosensor for Fe^{3+} Based on 1,3,4-Oxadiazole and Phosphonic Acid. *Sensor. Actuat. B-Chem.* **2014,** *200*, 259.

12. Lai, T.; Zheng, E.; Chen, L.; Wang, X.; Kong, L.; You, C.; Ruan, Y.; Weng, X., Hybrid Carbon Source for Producing Nitrogen-Doped Polymer Nanodots: One-Pot

Hydrothermal Synthesis, Fluorescence Enhancement and Highly Selective Detection of Fe(III). *Nanoscale* **2013,** *5*, 8015.

13. Zhang, S.; Li, J.; Zeng, M.; Xu, J.; Wang, X.; Hu, W., Polymer Nanodots of Graphitic Carbon Nitride as Effective Fluorescent Probes for the Detection of Fe^{3+} and Cu^{2+} Ions. *Nanoscale* **2014,** *6*, 4157.

14. Zhang, Y.-L.; Wang, L.; Zhang, H.-C.; Liu, Y.; Wang, H.-Y.; Kang, Z.-H.; Lee, S.-T., Graphitic Carbon Quantum Dots as a Fluorescent Sensing Platform for Highly Efficient Detection of Fe^{3+} Ions. *RSC Adv.* **2013,** *3*, 3733.

15. Qu, S.; Chen, H.; Zheng, X.; Cao, J.; Liu, X., Ratiometric Fluorescent Nanosensor Based on Water Soluble Carbon Nanodots with Multiple Sensing Capacities. *Nanoscale* **2013,** *5*, 5514.

16. Qu, K.; Wang, J.; Ren, J.; Qu, X., Carbon Dots Prepared by Hydrothermal Treatment of Dopamine as an Effective Fluorescent Sensing Platform for the Label-Free Detection of Iron(III) Ions and Dopamine. *Chem. Eur. J.* **2013,** *19*, 7243.

17. Zhao, A.; Zhao, C.; Li, M.; Ren, J.; Qu, X., Ionic Liquids as Precursors for Highly Luminescent, Surface-Different Nitrogen-Doped Carbon Dots Used for Label-Free Detection of Cu^{2+}/Fe^{3+} and Cell Imaging. *Anal. Chim. Acta* **2014,** *809*, 128.

18. Zhu, L.; Yin, Y.; Wang, C.-F.; Chen, S., Plant Leaf-Derived Fluorescent Carbon Dots for Sensing, Patterning and Coding. *J. Mater. Chem. C* **2013,** *1*, 4925.

19. Zhu, S.; Meng, Q.; Wang, L.; Zhang, J.; Song, Y.; Jin, H.; Zhang, K.; Sun, H.; Wang, H.; Yang, B., Highly Photoluminescent Carbon Dots for Multicolor Patterning, Sensors, and Bioimaging. *Angew. Chem. Int. Ed.* **2013,** *52*, 3953.

20. Xu, J.; Lai, T.; Feng, Z.; Weng, X.; Huang, C., Formation of Fluorescent Carbon Nanodots from Kitchen Wastes and Their Application for Detection of Fe^{3+}. *Luminescence* **2014**.

21. Xu, J.; Zhou, Y.; Liu, S.; Dong, M.; Huang, C., Low-Cost Synthesis of Carbon Nanodots from Natural Products Used as a Fluorescent Probe for the Detection of Ferrum(III) Ions in Lake Water. *Anal. Methods* **2014,** *6*, 2086.

22. Li, W.; Zhang, Z.; Kong, B.; Feng, S.; Wang, J.; Wang, L.; Yang, J.; Zhang, F.; Wu, P.; Zhao, D., Simple and Green Synthesis of Nitrogen-Doped Photoluminescent Carbonaceous Nanospheres for Bioimaging. *Angew. Chem. Int. Ed.* **2013,** *52*, 8151.

23. Liu, L. Q.; Li, Y. F.; Zhan, L.; Liu, Y.; Huang, C. Z., One-Step Synthesis of Fluorescent Hydroxyls-Coated Carbon Dots with Hydrothermal Reaction and Its Application to Optical Sensing of Metal Ions. *Sci. China-Chem.* **2011,** *54*, 1342.

24. Ding, H.; Wei, J.-S.; Xiong, H.-M., Nitrogen and Sulfur Co-Doped Carbon Dots with Strong Blue Luminescence. *Nanoscale* **2014,** *6*, 13817.

25. Yang, S.; Sun, J.; Li, X.; Zhou, W.; Wang, Z.; He, P.; Ding, G.; Xie, X.; Kang, Z.; Jiang, M., Large-Scale Fabrication of Heavy Doped Carbon Quantum Dots with Tunable-Photoluminescence and Sensitive Fluorescence Detection. *J. Mater. Chem. A* **2014,** *2*, 8660.

26. Zhou, L.; Lin, Y.; Huang, Z.; Ren, J.; Qu, X., Carbon Nanodots as Fluorescence Probes for Rapid, Sensitive, and Label-Free Detection of Hg^{2+} and Biothiols in Complex Matrices. *Chem. Commun.* **2012,** *48*, 1147.

27. Zhang, R.; Chen, W., Nitrogen-Doped Carbon Quantum Dots: Facile Synthesis and Application as a "Turn-Off" Fluorescent Probe for Detection of Hg^{2+} Ions. *Biosens. Bioelectron.* **2014,** *55*, 83.

Chapter 5: Summary & Conclusions

5.1 Summary

The aim of this research was to develop a solution phase synthetic method for preparation of highly luminescent, size monodisperse germanium nanocrystals, to control their photophysical properties through modification of their size and surface chemistry, and to demonstrate their applicability for selective detection of Fe^{3+} ion in aqueous solutions.

In **Chapter 2**, a simple synthetic method is described for the size controlled synthesis of amine-terminated Ge NCs by reduction of germanium precursors within inverse micelles under inert atmospheric synthetic conditions. Regulation of the Ge NCs size was achieved by variation of the cationic quaternary ammonium salts used to form the inverse micelles. The Ge NCs are chemically passivated with amine ligands using a Pt-catalysed hydrogermylation reaction, minimising surface oxidation while rendering the NCs dispersible in a range of polar solvents. HR-TEM and SAED showed that the NCs were size monodisperse, highly crystalline, with well-defined core diameters that may be tuned from 3.5 to 4.5 nm. FTIR spectroscopy confirmed that the ligand successfully attached to the surface of the NCs with minimal oxidation. UV-Vis absorbance and photoluminescence spectra showed moderate absorption in the UV spectral range, with a strong luminescence in the visible exhibiting a marked dependency on excitation wavelength. A maximum photoluminescence quantum yield of 20% was observed for the nanocrystals, while a transition from primarily blue to green emission was observed as the NC diameter was increased from 3.5 to 4.5 nm.

To determine whether the observed size threshold was due to quantum confinement effects or differing surface chemistry/oxidation, a polydisperse Ge NC sample with a mixed blue/green emission profile was prepared by modification of the synthetic protocol. TEM imaging showed that these Ge NCs had average sizes ranging from 3-12 nm, with a mean diameter of 6.4 nm, with a standard deviation of 2.0 nm. Following centrifugation, the amine terminated Ge NCs were separable into two discrete size fractions with an average diameters of 3.9 ± 0.4 nm and 6.8 ± 1.8 nm. The smaller 3.9 nm NCs possessed a strong blue luminescence, with an average lifetime of 6.1 ns and a QY of 21.5 %, which is strongly influenced by

solution pH. In contrast, 6.8 nm NCs exhibited a green luminescence with a longer lifetime of 7.8 ns and lower QY (6.2 %) that is insensitive to pH.

In **Chapter 3**, the synthesis of size monodisperse, butyl-terminated Ge NCs with *in situ* surface passivation was reported. The advantage of this method is that it allows rapid synthesis and functionalisation of NCs with minimal post-synthetic purification requirements. TEM imaging confirmed that the NCs are monodisperse and highly crystalline, while EDX and SAED was used to identify the elemental composition and crystal phase of the NCs. FTIR and XPS confirmed that the Ge NCs were well passivated, with some oxidation of the nanocrystal surface. Optical spectroscopy confirmed that the NCs were in the strong quantum confinement regime, with significant involvement of surface oxide species in exciton recombination processes. Photoluminescence quantum yields were determined to be 37 %, one of the highest values reported for organically terminated Ge NCs.

Later in the chapter, the preparation of size monodisperse Ge NCs with modified surface chemistries bearing carboxylic acid, acetate, amine and epoxy functional groups was reported. Using this approach, it was possible to produce high quality nanocrystals that were readily dispersed in polar organic solvents and/or water, depending on the surface functionality. TEM imaging showed that the modified Ge NCs were identical in size, while direct comparison of their emission properties showed that the wavelength position of the PL maxima could be moved from 410 nm to 495 nm.

Chapter 4 reports the application of Ge NCs as a sensing platform for the highly selective and sensitive detection of Fe^{3+} ions without the need for analyte-specific labelling groups. A linear relationship between the luminescence quenching and Fe^{3+} concentration was observed from 0.25 µM to 800 µM, with an upper limit of detection of 0.83 ± 0.02 µM and a lower LOD of 54 ± 6 nM. The Ge NCs show excellent selectivity toward Fe^{3+} ions, with no quenching of the fluorescence signal induced by the presence of Fe^{2+} ions, allowing for solution phase discrimination between ions of the same element with different formal charges. The luminescence quenching mechanism was confirmed by static and time-resolved

photoluminescence spectroscopies, while the applicability for this assay for detection of Fe^{3+} in real water samples was successfully demonstrated.

5.2 Conclusion

Much success has been achieved in the synthesis of colloidal Ge nanocrystals over the past decade. Earliest reports utilised highly reactive reducing agents, such as organoalkali and alkali metal reagents, as required to reduce the common $GeCl_4$ precursor to elemental Ge in appropriate solvents. Such chemistry makes it difficult to control size and morphology, and polydisperse samples with multiple co-existing morphologies are common. Alternative easier synthetic approaches emerged, which aimed to generate Ge nanocrystals under milder conditions, such as the metathesis reaction between $GeCl_4$ and germanide Zintl salts. Solution-mediated thermal decomposition reactions involving organogermane precursors are particularly attractive for generating colloidal Ge nanoparticles. Even milder reactions are possible, however, including simple one-pot heat-up methods that generate colloidal Ge nanocrystals without highly reactive and strong reducing agents, as well as thermal reduction methods that generate Ge NCs confined within a sol-gel-derived GeO_2 or SiO_2 matrix, which can be removed by dissolution. Among the highest quality colloidal Ge nanocrystals are those produced by reducing Ge halide precursors with reducing agents, these NCs have excellent uniformity, stability and emission characteristics.

Using a simple, one-pot synthetic technique, we produced Ge NCs emitting in the UV/violet range and reported the highest quantum yield for Ge NCs to date. This method is especially appealing as it elegantly passivates the surface *in situ* and includes a quick, simple reaction in addition to uncomplicated purification procedures. In this thesis we have also expanded this type of room temperature reaction, tuning the size of the nanocrystal formed (and also their photophysical properties), by exploring the surfactant structure used to form micelles as well as post-synthetic purification procedures. However, difficulties still exist with this method, as the $GeCl_4$ precursor reacts violently with water and the reducing agents employed are highly pyrophoric, consequently the reaction must be carried out

under rigorously inert atmospheres, hence the need for complicated techniques and equipment (glovebox). Moreover, the platinum catalyst used can be toxic to cells. Therefore, future work should look towards more green, environmentally friendlier and facile techniques such as reduction (using mild reducing agents) of GeO_2 species in water or even biocompatible methods like cultivating NCs inside a living animal/plant/cell. Synthetic protocols need further improvements in terms of scale-up, possibly by using flow rather than batch processes. Purification techniques, such as size selective column chromatography, must be utilised in order to produce highly pure monodisperse samples, but these can dramatically decrease overall yield and need future refinement.

The observation of photoluminescence in germanium nanocrystals at visible wavelengths is desirable for non-toxic optoelectronic and biological applications, but this emission is controversial due to its inconsistency with the quantum confinement effects expected for colloidal germanium nanocrystals. The occurrence of germanium oxide species may influence these observations, since colloidal Ge particles with surfaces that are considered highly passivated (e.g. with Ge-C bonds and no surface oxidation) are stable and IR emitting, with weak or only negligible visible-wavelength emission. Just one monolayer or even a sub-monolayer of a species at the surface of a nanocrystal can have profound effects on its emissive properties. These additional surface species can either act as a wider bandgap shell, confining charges to the crystalline core and increasing the quantum yield, or as trap defect sites where radiationless recombination may occur.

The surface chemistry of colloidal Ge nanocrystals is therefore critically important to possibly change the emission characteristics, and much effort has gone into modifying it. We have shed some insight into the role of surface species in Ge NC emission. The photoluminescence of our nanoparticles is hugely blue-shifted from what is expected for Ge NCs in the quantum confinement regime. Although we do indeed see some size effect for amine-terminated quantum dots (which emit in the blue and green regions), alkyl functionalised nanocrystals with a well characterised, thin, oxide layer show no size dependence and emit in the UV/violet range. Furthermore, when different moieties are attached to the nanocrystal surface, we

demonstrated that the emission could be tuned from the UV to the yellow, depending on what functional group is on the surface. These results, when compared to other high temperature reduction routes (which produce Ge nanocrystals emitting in the IR), highlight the important role played by surface species. To conclude, the chemical nature of the surface of Ge nanocrystals produced in this thesis is very complicated (as confirmed by FTIR and XPS) but it seems that the room temperature reduction, combined with a very small amount of oxidation leads to the UV/visible emission observed.

A full understanding of the origins and tuneability of the optical properties of Ge NCs is still needed to integrate both theoretical and experimental understandings. Future work should look in detail at either one, or numerous synthetic routes with the aim of tuning Ge NC emission from the UV all the way through to the IR. This may be achieved by starting with a room temperature reduction and subsequently adding a heating step to the method. Monitoring the emission as a function of temperature (and surface species) may provide further insight into the emission mechanisms. Emission from Ge NCs has been achieved in the UV through to the green region as well as the IR, consequently, explorations should include expanding the spectral coverage of germanium quantum dots to orange and red wavelengths. Other work should explore ligand exchange with surface functional groups such as hydrophilic polymers or phospholipids, as well as those able to bind to cells for imaging studies. While Ge is clearly less toxic than Cd, Hg, and Pb, which make up alternative quantum dot semiconductors, there are still concerns about the toxicity of Ge nanocrystals to cells. Further work should assess the toxicology of Ge NCs with different surface groups as some studies on other quantum dot families have shown that surface groups can contribute to toxicity. A complete study on the toxicity of Ge NCs must be completed which investigates the effects of size, monodispersity, purity and surface ligand on the toxicology of the NCs to cells and possibly live subjects, while work should also focus on retention time inside organs.

Ge NCs have lately been used in various applications such as biological imaging, thin films, field effect transistors, hybrid photodetectors and inverse opals. These applications demonstrate the versatility of this material and it could also be a

promising candidate for future applications in the fields of optoelectronic devices, photovoltaics and batteries. For bioimaging applications, research is required into the development of syntheses and functionalisation to target specific cell types and/or specific cell compartments as well as development for multifunctional therapies, including drug delivery. Here, we have expanded the applications of Ge NCs by using them, for the first time, as selective, fast and sensitive chemosensors for the efficient detection of Fe^{3+} ions. Ge NCs were found to be highly sensitive to the environmental pH, while the detection could be carried out in real water samples demonstrating the robustness of the detection system. Fe^{3+} ions were suggested to bind to oxygenic species on the surface, further highlighting the importance of surface species in Ge NCs. This type of binding could possibly be used in a further application to map the Fe^{3+} content in cells. Regarding sensing applications, new detection strategies, such as ratiometric, turn-on and FRET, are still needed because they can enhance the accuracy of the detection results. Design of Ge NCs to specifically sense other important metal ions would advance understanding in this field. Ge NC size or surface could be tailored to achieve this and would provide knowledge on the affinity of different Ge NCs to certain metal ions. The NCs cannot remove the detected metal ions, so the design of Ge NC-based nanosensors with dual functions of detection and removal of metal ions would be of great significance to the environment and human health. This could be achieved by attaching a molecule to the surface which can sense the ion in one medium and upon a change in the medium (i.e. change the pH), sequestration of the ion occurs and is transported with the Ge NC.

Many QD-based optoelectronic structures, such as LEDs or displays, have already been realised based on direct bandgap materials. Nevertheless, these materials are typically either highly toxic. On the other hand, Ge NCs offer an ideal environmentally friendly and readily available substitution for these materials but have not been used to date in light emitting applications such as LEDs. Si NCs have already been utilised in these applications, and high efficiencies could be achieved with Ge NCs by optimising the choice of polymer charge transport layers (both for electrons and for holes), which ensure the confinement of electrons and holes in

the emissive layer. In this regard, there is much room for experimentation. Apart from applications requiring charge injection, Ge NCs could also be used as a passive phosphor hybrid film in spectral converters. These are typically combined with a UV/blue diode in order to achieve a 'warmer' colour of light, similar to that of a traditional incandescent bulb, but with lower power consumption. Given the precise control of the emission colour achieved in Chapters 2 and 3, it could be possible mix different colour fractions to produce a phosphor film for broadband or even white-light applications. Currently available germanium nanocrystals are far from being ideal, leaving plenty of room for the development of novel NCs, understanding of the emission mechanism and further exploration of their use in various applications.

Appendix

6.1 Appendix

6.1.1 Peer Reviewed Publications

1. Size and Emission Colour Tuning in the Solution Phase Synthesis of Highly Luminescent Germanium Nanocrystals. **Darragh Carolan** and Hugh Doyle. *J. Mater. Chem. C, 2014, 2, 3562*

2. Efficient One-Pot Synthesis of Monodisperse Alkyl-Terminated Colloidal Germanium Nanocrystals. **Darragh Carolan** and Hugh Doyle. *J. Nanopart. Res., 2014, 16, 2721*

3. Germanium Nanocrystals as Luminescent Probes for Rapid, Sensitive and Label-Free Detection of Fe^{3+} Ions. **Darragh Carolan** and Hugh Doyle. *Nanoscale, 2015, 7, 5488*

4. Synthesis and Compositional Control of Size Monodisperse Si_xGe_{1-x} Nanocrystals for Optoelectronic Applications. Keith Linehan, **Darragh Carolan**, Daithi Ó Sé and Hugh Doyle. *2013 MRS Spring Meeting*

5. Proteomic evaluation of citrate-coated silver nanoparticles toxicity in Daphnia magna. Louis-Charles Rainville, **Darragh Carolan**, Ana Coelho Varela, Hugh Doyle and David Sheehan. *Analyst, 2014, 139, 1678*

6.1.2 Targeted Publications

6. Tuning the Photoluminescence Properties of Ge NCs Using Polarisable Ligands. **Darragh Carolan** and Hugh Doyle. *Manuscript in preparation*

7. Carbon Quantum Dots Extracted from Toast and Tobacco Ash and their Applications as Sensors and Phosphors. **Darragh Carolan** and Hugh Doyle. *Manuscript in preparation*

8. Silicon Nanocrystals as Luminescent Probes for the Detection of Fe^{3+} ions. Keith Linehan, **Darragh Carolan**, and Hugh Doyle. *Manuscript in preparation*

9. Extraction of Carbon Quantum Dots from Pineapple Juice and their Applications. Keith Linehan, **Darragh Carolan**, and Hugh Doyle. *Manuscript in preparation*

10. Metal Nanoparticles as Seeds for the Fast, Efficient Growth of Lysozome Protein Crystals. AleksandraCzekaj, **Darragh Carolan**, Hugh Doyle and David Sheehan *Manuscript in preparation*

6.1.3 Outputs

Discovery Exhibition, City Hall, Cork November 2011/2012

"Chemical Synthesis and Characterisation of Germanium Nanocrystals"

Postgraduate Symposium on Nanotechnology, December 2011

University of Birmingham

United Kingdom

"Chemical Synthesis and Characterisation of Germanium Nanocrystals"

Tyndall Postgraduate Poster Competition 2012 & 2013

6.1.4 Modules

PG 6009 Information Literacy Skills

PG 6001 Scientific Training for Enhanced Postgraduate Study

PY 3108 Lasers and Laser Safety (Frank Peters UCC)